NNT/NL : 2022AIXM0000/000ED352
DES/IRESNE/DER/SPESI/LP2E 2021-0083-DO

DOCTORAL THESIS

Defended at 21/02/2022

Júlia Bartos

Dynamic analysis of the energy deposition during a reactivity insertion accident in the CABRI research reactor

Discipline
Physics and Materials Science

Specialty
Energy, Radiation and Plasma

Doctoral school
ED 352 – Physics and Materials Science

Host laboratory
Commissariat à l'Énergie Atomique et aux Énergies Alternatives
CEA/DES/IRESNE/DER/SPESI/LP2E

Jury

Dr. Adrien BIDAUD IN2P3/LPSC	Reviewer
Dr. Andrei RINEISKI KIT/INR	Reviewer
Pr. Andreas PAUTZ PSI	Examiner
Pr. Christelle REYNARD-CARETTE AMU	Examiner
Dr. Jaques Di SALVO IRSN	Examiner
Dr. Claire VAGLIO-GAUDARD CEA	Thesis director
Dr. Adrien GRUEL CEA	Thesis supervisor (Guest)

AFFIDAVIT

I, undersigned, Julia BARTOS, hereby declare that the work presented in this manuscript is my own work, carried out under the scientific direction of Claire VAGLIO-GAUDARD and Adrien GRUEL, in accordance with the principles of honesty, integrity and responsibility inherent to the research mission. The research work and the writing of this manuscript have been carried out in compliance with both the French national charter for Research Integrity and the Aix-Marseille University charter on the fight against plagiarism.

This work has not been submitted previously either in this country or in another country in the same or in a similar version to any other examination body.

Place Aix en Provence, date 12/12/2021

Cette œuvre est mise à disposition selon les termes de la Licence Creative Commons Attribution - Pas d'Utilisation Commerciale - Pas de Modification 4.0 International.

PUBLICATIONS AND CONFERENCES

1) List of publications :

    1. Bartos, J., Gruel, A., Vaglio-Gaudard, C and Coquelet-Pascal, C., 2021 November, Some Considerations on the Energy Deposition During a RIA Transient Based on Monte Carlo Simulations. In *EPJ Web of Conferences* (Vol. 253, p.04005). EDP Sciences

2) Conference participations :

    1. ANIMMA 2021 Conference, June 21-25 2021

        Oral presentation: *Some Considerations on the Energy Deposition During a RIA Transient Based on Monte Carlo Simulations*

To my primary school teacher
Who, unbeknownst to her, put me on this track 20 years ago

Emma tanító néninek
Aki mindent megtett annak érdekében, hogy mindenki elérhesse a potenciálját

ACKNOWLEDGMENTS

First of all, I would like to sincerely thank my thesis director Claire and my supervisor Adrien for their continuous support, guidance and for always being ready to help these past years. I would like to express my gratitude to Christine, the head of laboratory, for anticipating the difficulties and to making sure I could deal with them. And for each one of them for giving me the time I needed to recover without any additional pressure.

Adrien, I have to put it in writing that your manuscript correction speed still amazes me (even though at the beginning I would have been more than okay with having more days pass between my submission and your corrections). Speaking of corrections, your comment of 'Please rewrite this part as if it were your manuscript' instead of saying that those pages are completely useless, still makes me laugh.

I would like to express my gratitude to the jury members Andreas Pautz, Christelle Reynard-Carette, Jacques di Salvo, and in particular my rapporteurs Adrien Bidaud and Andrei Rineiski, for finding time to critically evaluate this manuscript and participating in the final defense.

I am very grateful for their availability and help provided with the kinetic module of TRIPOLI4 for Davide Mancusi, Andrea Zoia and Paul.

Also huge thanks to the Ph.D. students of the 'basement', Hamza for showing how to make nice plots and for sending that screenshot from ANIMMA; Yifeng, Augusto for the after Covid picnics in the park and David for the amusing correction style. Georges, good luck for the next years!

As for the class of 202(1)2, Augusto, I'm glad I got to share the office with you! Your unexpected, yet typically Italian, blasphemies, as you call them, woke me up several times, quite the benefit. Tristan, I knew it will be fun after the first 'mamie'. This list could be quite long, so instead it will be short. Thank you, really, for listening to me complaining, it is definitely in the top 3 of the most helpful things from last year! Also, thank the stars our procrastination cycles synchronized towards the end, otherwise, we would still be writing our first draft (and by 'we' I mean me, you still are).

Kornilius, without previous coordination I ended up doing my thesis in your lab! I'm very happy it happened like that. Thanks for all our (endless) conversations; they make up for the fact that you were supposed to be my way into the social life of the lab. I should have known better!

Special mention to Maxime, who makes the best raspberry jam and whose French skills amazed me until I realized he is actually French, for providing the headquarters for the apéros and in general for keeping alive our Whatsapp group.

Special thanks to Maciej, the Python master and chief editor, you saved my sanity multiple times. In the same order of ideas, thanks to Emilia and you for choosing a place to live that came with a pool! Also, thanks for the good times spent in and around that pool, I still owe you guys a Sainte Victoire hike.

Elias, of whom I always think of being my first friend (I mean colleague) at Cadarache, thank you for not letting me forget that I did not attend your defense, the one you did NOT invite me to.

Mira, Atul and Raoul our India trip was one to remember, we managed to outrun Covid that time, although it caught up with us and Australia had to stay on our wish list. To many more trips to come!

Thank you Mira, other Mira, Kamilla for the support provided during the years. Special mention to the Hungarian team (who knew we were that many in such a small city?), girly girls, and to my flatmates for all the welcomed and unwelcomed distraction provided during these last years.

Eszter, thanks for all the support on both personal and professional level, for providing a social life and most importantly thank you for showing me a completely different way of being! Also, for not taking no for an answer (like when I explicitly told you I do not want to celebrate my birthday and you still showed up with a cookie anyhow) and for celebrating the wins I don't feel like celebrating. Also, the messages about going lunch 5 minutes after arriving to work were sometimes the highlight of my day!! And I really appreciate that you, Anne and Diane, kind of adopted me these last months and for all those co-working sessions. Now, if only you would actually listen to some of my advices…

Finally, I would like to thank my parents and sisters for their overall support and for respecting and not questioning my ban on talking about the PhD when I'm at home.

ABSTRACT

Specific research reactors are capable of simulating Reactivity insertion accident (RIA) phenomenology, in order to study the behavior of nuclear fuel pins in accidental situations. In the CABRI research reactor, the fuel pin to be examined (test pin) is placed at the center of the core in a dedicated test loop. It is then subjected to a power transient, obtained by the rapid depressurization of the helium-3 neutron absorber gas from transient rods located in the core. One of the central parameters of the experiment is the energy deposition into the test pin, which is currently not measured during a transient. Instead, it is assumed that the relative energy distribution between the core and the test pin is constant regardless of the operational state of the reactor. Currently, this correlation is measured and calculated in steady state and assumed constant during the transient. The goal of this work is to assess the dynamic energy deposition into the test pin and to study how the energy deposition rate changes during the power transient by Monte Carlo modelling and simulation. The transition between the current static calculation to a dynamic TRIPOLI-4® stochastic calculation is achieved progressively, by developing two methodologies.

In the first methodology a criticality calculation is run for consecutive core configurations, representative of different stages of the transient. This allows for observation of the variations in the parameters of interest during the transient with the codes already being utilized, and sheds a light on the most impactful parameters on the energy deposition rate, such as the helium depressurization and the Doppler feedback. The results illustrate that contrary to the current assumption, the energy deposition rate between the core and the test pin, i.e. the energy distribution rate, varies during the power pulse. The relative difference in the energy deposition rate between the core and test pin increases to 6% in the studied transients, and this increase is primarily determined by the initial helium pressure and the depressurization type. The energy deposited in the test pin is estimated based on the fission energy generated by the fission events in the test pin throughout the transient. It was also estimated based on nuclear heating, in which the transport of the secondary particles generated during fission is simulated. The result showed that regardless of the test pin type, around 10% of the fission energy generated in the test pin is deposited outside the test pin.

The second methodology is based on a fully dynamic simulation of the transient obtained by using the newly developed dynamic module of the TRIPOLI-4® code, which allows the simulation of non-stationary conditions. The aim of this simulation is twofold: to validate the energy deposition calculation scheme and to assess the kinetic module's capabilities. In the case of a supercritical transient there is a good agreement between the results of the dynamic and stepwise regarding the flux distribution and the variation of the integral parameters. However, the results show that the dynamic module is not able to correctly reproduce the power increase in case of prompt supercritical transients.

Keywords : Energy deposition, RIA, CABRI, Kinetic Monte Carlo, TRIPOLI-4®

RESUME

Des réacteurs de recherche spécifiques sont capables de reproduire des accidents d'injection de réactivité (RIA), afin d'étudier le comportement du combustible nucléaire dans des conditions accidentelles. Dans le réacteur de recherche CABRI, le combustible à examiner (crayon d'essai) est placé au centre du cœur dans une boucle de test dédiée. Il est ensuite soumis à un transitoire de puissance, obtenu par la dépressurisation rapide du gaz absorbeur de neutrons de (hélium-3), contenu dans les barres transitoires. L'un des paramètres centraux de l'expérience est le dépôt d'énergie dans le crayon d'essai, qui n'est actuellement pas mesuré pendant un transitoire. On suppose plutôt que la distribution d'énergie relative entre le cœur et le crayon d'essai est constante quel que soit l'état de fonctionnement du réacteur. Actuellement, cette corrélation est mesurée et calculée à l'état stationnaire et est considérée constante pendant le transitoire. L'objectif de ce travail est de calculer le dépôt d'énergie dynamique dans le crayon d'essai et d'étudier comment le taux de dépôt d'énergie change pendant le transitoire à l'aide d'un code stochastique. La transition entre le calcul statique actuel et l'utilisation du module cinétique de TRIPOLI-4® est réalisée progressivement, en développant deux méthodologies.

La première méthode est basée sur des calculs stochastiques à l'état stationnaire, où un calcul de criticité est effectué pour des configurations de cœur consécutives, représentatives des différentes étapes du transitoire. Cela permet d'observer les variations dans les paramètres d'intérêt pendant le transitoire avec les codes déjà à disposition, et met en lumière sur les paramètres les plus impactant sur le taux de dépôt d'énergie, tels que la dépressurisation d'hélium et l'effet Doppler. Les résultats montrent également que, contrairement à l'hypothèse actuelle, le taux de dépôt d'énergie entre le cœur et le crayon d'essai, c.-à-d. la distribution d'énergie, varie pendant le pulse de puissance. La différence relative du taux de dépôt d'énergie entre le cœur et le crayon d'essai augmente de 6 % dans les transitoires étudiés, et cette augmentation est principalement déterminée par la pression initiale d'hélium et le type de dépressurisation. L'énergie déposée dans le crayon d'essai est estimée sur la base de l'énergie de fission générée par les événements de fission dans le crayon d'essai tout au long du transitoire. L'énergie déposée a également été estimée à partir des échauffements nucléaires, dans lequel le transport des particules secondaires générées lors de la fission est simulé. Le résultat a montré que quel que soit le type de crayon d'essai, environ 10% de l'énergie de fission générée dans le crayon d'essai est déposée à l'extérieur de celui-ci.

La deuxième méthodologie est basée sur une simulation dynamique du transitoire et est obtenue en utilisant le nouveau module du code TRIPOLI-4®, qui permet la simulation de conditions non stationnaires. L'objectif de cette simulation est double : valider le schéma de calcul des dépôts d'énergie et évaluer les capacités du module cinétique sur la modélisation des transitoires de puissance réalisés dans CABRI. Dans le cas d'un transitoire supercritique il y a un bon accord entre les deux méthodologies en ce qui concerne la distribution de flux et la variation des paramètres intégraux. Cependant, les résultats montrent que le module cinétique n'est actuellement pas capable de reproduire correctement l'augmentation de puissance en cas de transitoires surcritiques prompts.

Mots clés : Dépôt d'énergie, RIA, CABRI, Monte Carlo cinétique, TRIPOLI-4®

RESUME ETENDU

Introduction

Fournir une énergie sûre, fiable et économiquement viable est une nécessité pour la production d'énergie nucléaire. L'objectif le plus important en matière de sûreté nucléaire est de garantir que le public n'est pas exposé à des risques radiologiques provenant d'installations nucléaires. Par conséquent, l'un des principaux domaines d'intérêt des analyses de sûreté est le comportement du combustible dans des situations opérationnelles et accidentelles, car il constitue la principale source de rayonnements dans une centrale électrique.

Les principaux critères de sûreté relatifs au combustible ont été définis dans les années 1970 par la Nuclear Regulatory Commission des États-Unis et reposaient sur des données expérimentales de réacteurs de recherche. Ces premiers essais ont porté sur du combustible neuf ou modérément irradié, conformément au taux moyen de combustion des centrales existantes. Les données fournies par ces expériences ont montré que le degré d'endommagement du combustible est en corrélation avec le dépôt d'énergie dans le combustible, qui a donc été défini comme critère de sûreté. Toutefois, les progrès technologiques et les progrès de la recherche en matière de gestion du combustible ont incité les opérateurs à utiliser le combustible à plus fort taux de combustion. Le manque de données expérimentales associé à ces taux de combustion élevés a conduit les autorités à lancer de nouveaux programmes expérimentaux en France, au Japon et en Russie.

La boucle à eau pressurisée fournissant des conditions représentatives de celles d'un réacteur électrogène pendant l'essai, la possibilité d'adaptation des paramètres des transitoires, les différents types de crayons d'essai qui peuvent être utilisées font de CABRI un réacteur de recherche unique en termes d'études du comportement du combustible au cours de transitoires de puissance. Le crayon d'essai à examiner est placé dans une boucle d'essai au centre du cœur et est soumis à un transitoire de puissance obtenu par la dépressurisation rapide de l'hélium-3, absorbant neutronique, contenu dans des tubes situés dans le cœur.

Afin de définir les paramètres expérimentaux initiaux qui aboutissent au transitoire recherché tout en veillant au respect des limites de sûreté d'exploitation, il est impératif de s'appuyer sur des outils de calcul et des simulations spécifiques. Jusqu'à récemment, les problèmes neutroniques non stationnaires, tels qu'un accident d'injection de réactivité, étaient résolus par des méthodes déterministes, tandis que l'approche stochastique, ou Monte Carlo, était utilisée comme méthode de référence pour les calculs à l'état stationnaire.

Dans cette optique, le but de ce doctorat est de développer une méthodologie de calcul stochastique non stationnaire pour le réacteur CABRI qui permettrait de calculer des paramètres dynamiques au cours du transitoire de puissance. Cela peut ouvrir la voie à la simulation multiphysique de conditions non stationnaires reposant sur des codes cinétiques

3D. Plus précisément, l'objectif est d'évaluer le dépôt d'énergie dynamique dans le crayon d'essai et d'étudier comment celui-ci évolue pendant le transitoire à l'aide du code TRIPOLI-4®.

Méthodes et objectifs

La modélisation d'un accident d'injection de réactivité, un phénomène intrinsèquement multiphysique, nécessite le couplage de codes cinétiques 3D avec des codes de comportement thermohydraulique et thermomécanique. Dans le contexte du réacteur CABRI, plusieurs efforts ont été faits dernièrement pour développer et valider des outils de simulation déterministes basés sur une modélisation multiphysique pour prévoir le pulse de puissance et le dépôt d'énergie pendant le transitoire.

Le principal outil utilisé pour les études de prédiction et de sûreté des expériences dans CABRI est le code DULCINEE, un code multiphysique basé sur le couplage d'un module thermo-hydraulique 1D avec un module cinétique point pour calculer la puissance du cœur. Il permet à la fois des calculs stationnaires et transitoires. Pour améliorer la prédiction des caractéristiques physiques du transitoire, telles que le pic de puissance, la durée du transitoire et le dépôt d'énergie, un nouvel outil de modélisation appelé PALANTIR a été développé, basé sur l'outil de calcul scientifique CATHARE, un code de référence développé pour l'analyse (thermohydraulique à l'échelle du système) des transitoires dans les REP et les réacteurs rapides au sodium. PALANTIR s'appuie sur le couplage d'un modèle de cinétique ponctuelle (avec calcul des effets de réactivité 3D pour les neutronique), un modèle multi-1D pour le thermo-hydraulique du cœur, un modèle du dispositif de dépressurisation de l'hélium et un modèle de thermomécanique. Il calcule l'évolution de la puissance, de la température (combustible et modérateur) et de la réactivité pendant le transitoire.

Le code de référence stochastique utilisé pour le calcul neutroniques dans CABRI est le code de Monte Carlo TRIPOLI-4®, développé au CEA. Au cours de ce travail, un module de cinétique nouvellement développé et intégré à ce code, permettant de simuler un état non stationnaire, a été mis en œuvre.

Le passage de la simulation statique à la simulation dynamique est réalisé progressivement, en développant deux méthodologies. La première méthodologie, appelée méthode *stepwise*, est fondée sur des calculs stochastiques à l'état stationnaire. Dans cette méthodologie, un calcul de criticité est effectué pour des géométries consécutives représentatives des différentes étapes du transitoire. Cela permet d'observer les variations des paramètres d'intérêt pendant le transitoire avec des outils déjà à notre disposition, et confirme les paramètres les plus impactant sur le dépôt d'énergie, tels que la dépressurisation d'hélium et l'effet Doppler. La seconde méthodologie met en œuvre une simulation entièrement dynamique du transitoire, obtenue en utilisant le nouveau module dynamique du code TRIPOLI-4®. L'objectif de cette simulation est double : valider le schéma de calcul des dépôts d'énergie et évaluer les capacités du module cinétique sur la modélisation des transitoires de puissance réalisés dans CABRI.

Schéma de calcul

L'un des objectifs de la thèse est de calculer le dépôt d'énergie dynamique dans le crayon d'essai ainsi que le facteur de couplage dynamique. Le dépôt d'énergie dans le crayon au cours du transitoire n'est actuellement pas mesuré et il est calculé à partir de l'énergie déposée dans le cœur et d'un facteur de couplage. Le facteur de couplage est défini comme le rapport de la puissance du cœur et du crayon d'essai ; il est actuellement mesuré et calculé en régime permanent. Il est supposé constant et valide pour tout le transitoire. Il y a plusieurs approximations introduites par cette hypothèse, comme ne pas prendre en considération l'influence possible de la dépressurisation de l'hélium, les contre-réaction sur le flux et le spectre neutronique, qui pourraient modifier la valeur du facteur de couplage précédemment estimé.

Deux méthodes sont utilisées pour calculer le dépôt d'énergie à l'aide de TRIPOLI-4®. Dans la première approche, l'énergie est estimée sur la base de l'énergie libérée à la suite d'une fission, tandis que dans la seconde, le dépôt d'énergie est calculé sur la base des échauffements nucléaires. La première méthodologie repose sur l'hypothèse que l'énergie libérée lors d'une fission se dépose entièrement à l'endroit où la fission a eu lieu. Ainsi, le calcul de la puissance libérée dans un volume donné ne nécessite que l'estimation des événements de fission dans le volume. Chaque isotope fissile libérant une quantité d'énergie différente pendant la fission, les taux de fission doivent être comptabilisés individuellement pour chaque isotope fissile présent dans le volume étudié. Les paramètres d'intérêt sont calculés avec TRIPOLI-4® en mode statique ou dynamique, en fonction du schéma de calcul utilisé. Dans le cas du schéma de calcul *stepwise*, un calcul statique indépendant est exécuté pour chaque configuration utilisée pour modéliser le transitoire. Dans le cas du schéma dynamique on obtient directement les variations des paramètres d'intérêt au cours du temps.

Afin de tenir compte de la distribution spatiale de l'énergie produite pendant la fission, le dépôt d'énergie peut être calculé à partir des échauffements nucléaires. Dans le cas des réacteurs de puissance, l'échauffement nucléaire est exprimé en termes de dépôt d'énergie (W/g) dans un volume donné. TRIPOLI-4® calcule le dépôt d'énergie de chaque particule transportée selon la méthode du bilan énergétique, en soustrayant l'énergie transportée par les particules transportées de l'énergie cinétique initiale disponible. Cette méthodologie n'est mise en œuvre que dans les calculs statiques.

Modélisation d'un transitoire CABRI

Une dépressurisation continue ne peut pas être simulée avec les codes stochastiques disponibles. Par conséquent, la dépressurisation est représentée par une succession de géométries intermédiaires. L'injection de réactivité spécifique au réacteur CABRI consiste en une dépressurisation de l'hélium très rapide. Selon la quantité de réactivité injectée, cette

dépressurisation peut être suivie d'une augmentation de la température du combustible et du modérateur. À ce titre, compte tenu de l'absence de changement de géométrie et de compositions, toute configuration intermédiaire du cœur peut être représentée par une pression d'hélium et une température de combustible et de modérateur. Ces données sont obtenues avec le code PALANTIR.

Deux types de transitoires sont considérés au cours de ce travail : un transitoire surcritique et un transitoire surcritique prompt. Une dépressurisation à partir de 0,73 bar a été choisie pour le cas surcritique. Cette dépressurisation correspond à une insertion de réactivité d'environ 560 pcm. La puissance initiale du cœur est de 0,1 MW et la puissance maximale atteinte pendant ce transitoire est de 0,7 MW, ce qui entraîne un dépôt d'énergie de 0,56 MJ dans le cœur jusqu'au moment de la chute des barres de contrôle. Le cas surcritique prompt est une dépressurisation à partir de 1,4 bar correspondant à une injection de réactivité de 860 pcm. Il en résulte un pic de puissance de 230 MW et un dépôt d'énergie de 22 MJ.

Lors du choix des géométries intermédiaires, l'insertion de la réactivité doit être correctement modélisée. À ce titre, les géométries sont choisies afin d'être représentatives des principales étapes du transitoire : la phase initiale, où il y a dépressurisation mais pas de changement de température de combustible, le pulse, où il y a une augmentation significative de la température, mais la variation de pression est moins importante et l'étape finale, où la pression et la température se sont stabilisées. Pour s'assurer que l'insertion de réactivité est correctement représentée, l'évolution de puissance est également calculée à l'aide des équations de cinétique ponctuelle et des réactivités obtenues pour chaque configuration, afin de donner une estimation approximative de l'évolution de puissance.

Figure 1 et Figure 2 présente les évolution des principaux paramètres et les géométries choisies le transitoire supercritique et supercritique prompt.

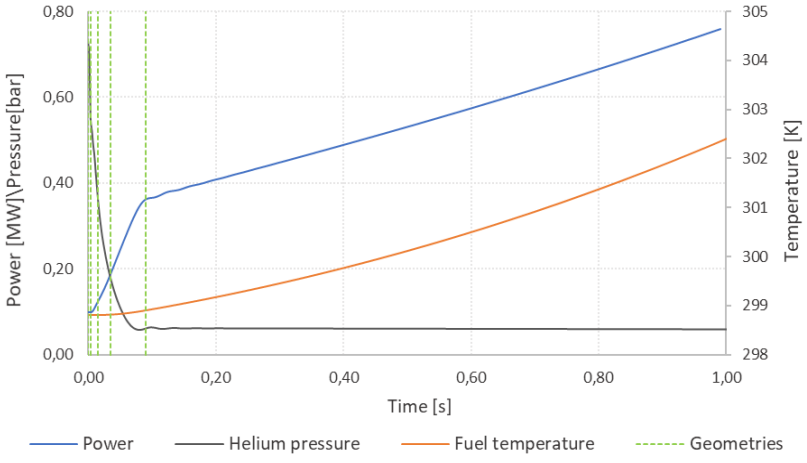


Figure 1. Evolution des principaux paramètres lors de la dépressurisation supercritique. Résultats obtenus avec PALANTIR. Les lignes vertes verticales représentent les géométries choisies

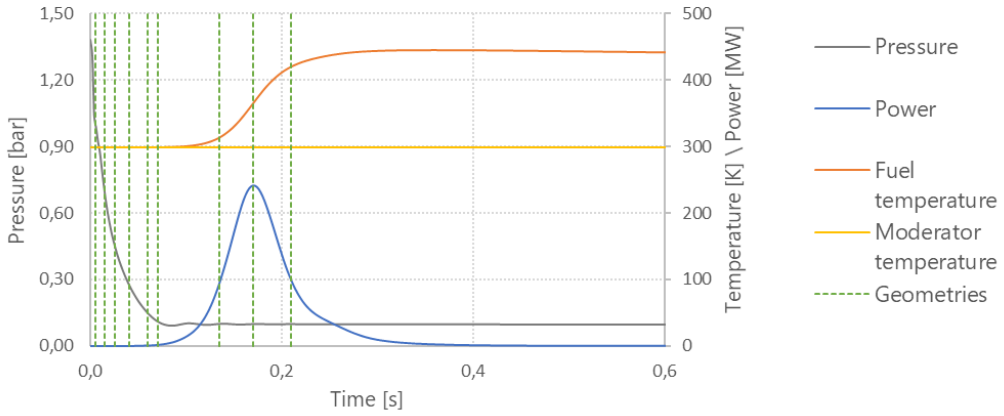


Figure 2. Evolution des principaux paramètres lors de la dépressurisation supercritique prompt. Résultats obtenus avec PALANTIR. Les lignes vertes verticales représentent les géométries choisies

L'étape suivante consiste à exécuter le calcul dynamique et à comparer les résultats avec la puissance calculée avec PALANTIR et la puissance expérimentale. Dans le cas du transitoire surcritique, les résultats obtenus avec la méthodologie *stepwise* sont en bon accord avec les résultats du calcul dynamique, la puissance donnée par PALANTIR et la puissance expérimentale (Figure 3). La validation de la modélisation est complétée par une analyse de sensibilité sur le calcul de la puissance dynamique, centrée sur l'impact des incertitudes de quelques paramètres d'entrée.

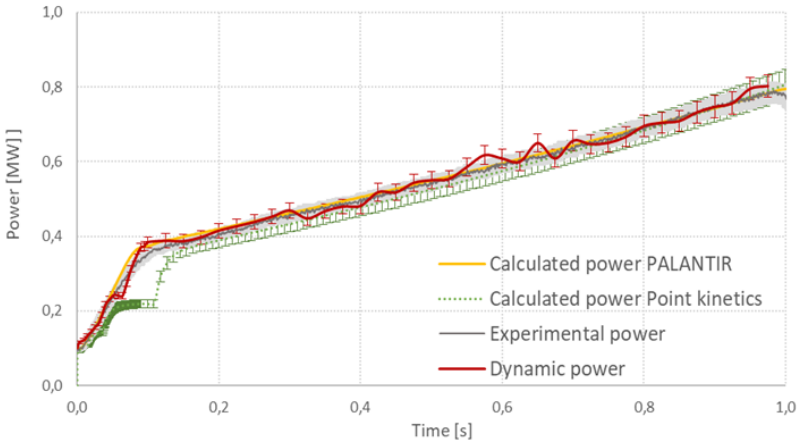


Figure 3. Comparaison entre la puissance calculée et expérimentale dans le cas du transitoire surcritique. Incertitudes données à 1σ

Dans le cas du transitoire surcritique prompt, les résultats ont révélé que le module cinétique mis en œuvre dans TRIPOLI-4® n'est pas encore en mesure de calculer correctement l'évolution de la puissance, comme le montre la Figure 4. Le pic de puissance est sous-estimé d'un facteur 100, invalidant les résultats des simulations cinétiques.

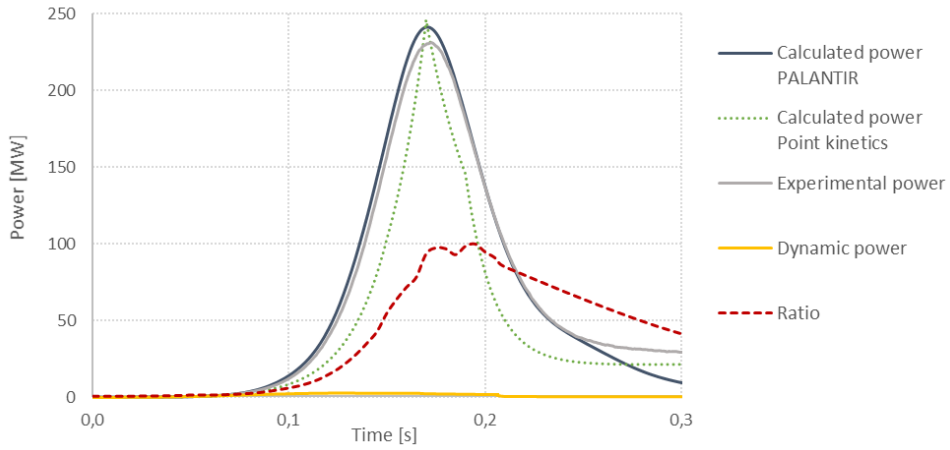


Figure 4. Comparaison entre la puissance calculée et expérimentale dans le cas du transitoire surcritique prompt

Distribution de flux

Même s'il existe différentes approches pour estimer le dépôt d'énergie dans TRIPOLI-4®, chacune d'entre elles est basée sur la même quantité physique : le flux de neutrons. Par conséquent, la distribution et la variation du flux neutronique seront analysées avant d'aborder l'évolution des paramètres intégraux, tels que le facteur de couplage ou le dépôt d'énergie.

La Figure 5 présente la distribution radiale du flux dans la configuration critique du cœur et la variation relative du flux suite à la dépressurisation pour le transitoire surcritique, obtenue avec le module dynamique. La distribution du flux radial reflète les particularités du cœur du réacteur, telles que la présence du canal hodoscope qui traverse le cœur et de la boucle à eau pressurisée au centre. Étant donné que la pression d'hélium initiale est faible, l'impact des assemblages transitoires sur le flux est minime. La dépressurisation de l'hélium entraîne une augmentation globale du flux dans le cœur, mais la variation relative du flux n'est pas la même de partout. L'augmentation du flux est le plus importante autour des barres transitoires, comme indiqué sur le graphique de droite de la Figure 5, ce qui entraîne une augmentation du flux plus élevée dans la périphérie que dans le centre, conduisant à une distribution finale du flux plus plate. La même chose peut être observée pour la dépressurisation surcritique prompte. De plus, il existe un bon accord entre les résultats *stepwise* et dynamiques. La différence relative entre le flux *stepwise* et le flux dynamique est couverte par les incertitudes statistiques des scores (3%).

Contrairement à la distribution radiale du flux, la distribution axiale du flux ne varie pas pendant ce transitoire. Les paramètres qui pourraient induire une variation dans la distribution initiale du flux axial sont les positions de la barre de contrôle, la pression de l'hélium et l'effet Doppler. La position de la barre de contrôle n'est pas modifiée pendant le transitoire, l'effet Doppler est homogène sur le cœur (la température du combustible n'est pas discrétisée) et la

dépressurisation de l'hélium, bien que localisée radialement, est homogène axialement. Les résultats *stepwise* et dynamiques sont en bon accord.

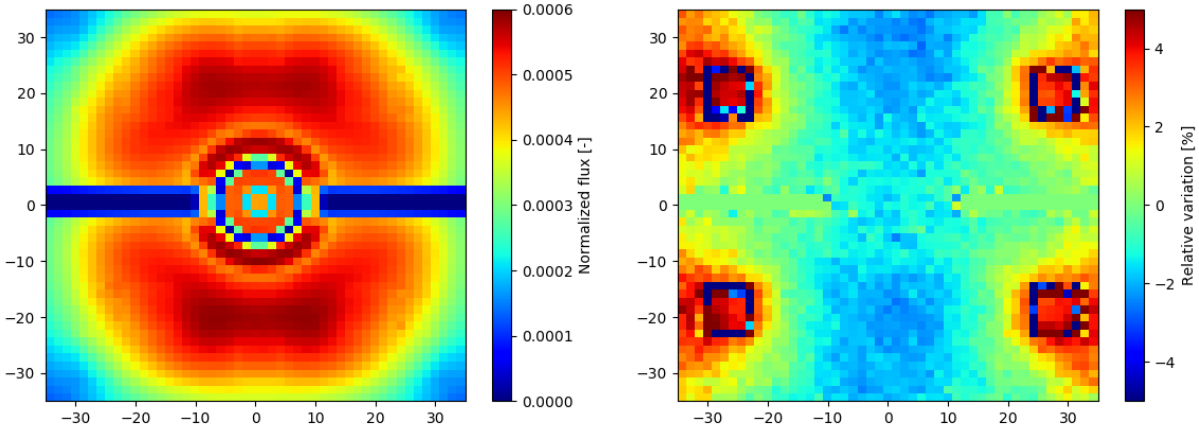


Figure 5. Distribution radiale du flux dans la configuration critique du cœur (à gauche) et variation relative du flux à la fin du transitoire (à droite). Résultats obtenus avec le module dynamique

La Figure 6 présente les spectres de flux neutronique pour la configuration critique, discrétisé en 99 groupes d'énergie, dans le crayon d'essai et le cœur, obtenu avec le module dynamique. Les résultats soulignent que le spectre dans le cœur est plus dur que dans le crayon d'essai. Les spectres de flux calculés avec les modules statique et dynamique sont en bon accord. La différence relative est de l'ordre de l'incertitude statistique. Le flux thermique (<0,4 eV) représente 22%, le flux intermédiaire (0,4 eV à 1 MeV) 46% et le flux rapide (1 à 20 MeV) 32% du flux total. La différence relative entre la distribution des flux finale et initiale est inférieure à 0,5 %.

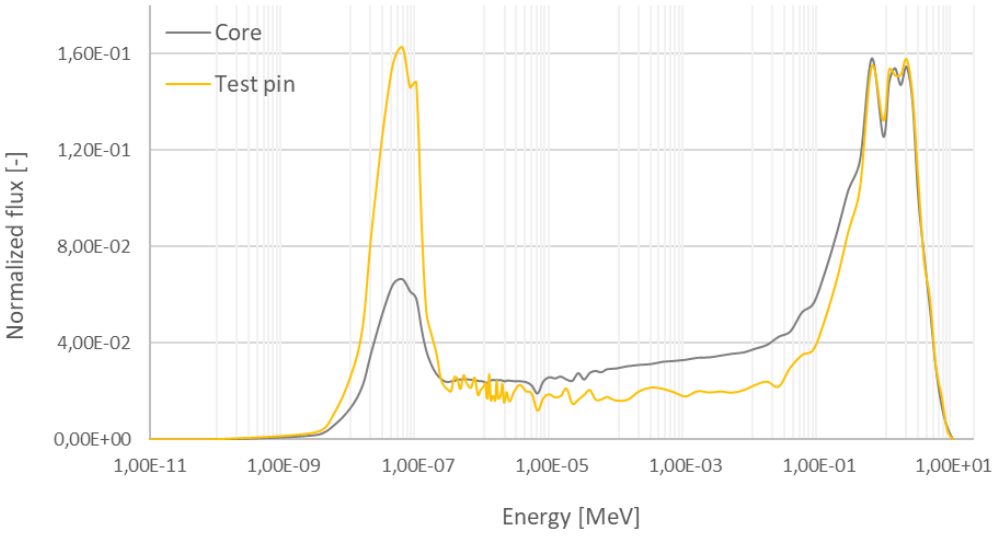


Figure 6. Spectre du flux neutronique par unité de léthargie dans le cœur et dans le crayon d'essai dans la configuration critique du cœur, obtenu avec le module dynamique

Dépôt d'énergie

L'objectif principal de la thèse est de définir une méthodologie de calcul pour estimer le dépôt d'énergie dans le crayon d'essai lors d'un transitoire dans le réacteur CABRI. Cependant, ce n'est pas seulement la valeur absolue du dépôt d'énergie qui nous intéresse, mais aussi son évolution tout au long du transitoire. Cette évolution fournit également des informations concernant un autre aspect important : le couplage entre le cœur et le crayon d'essai.

Transitoire surcritique

Le calcul du dépôt d'énergie est similaire pour les schémas de calcul statiques et dynamiques. Le taux de fission est calculé pour chaque isotope fissile présent et est multiplié par l'énergie de fission correspondante. Les résultats sont cumulés dans les volumes correspondants. Dans le cas du schéma statique, un calcul est exécuté pour chacune des géométries choisies, et en tant que tel, la puissance calculée à chaque géométrie est en fait une valeur de puissance (donc instantanée). Ensuite, les résultats sont normalisés à la puissance du cœur correspondant à cette géométrie, obtenue avec PALANTIR. Une fois la puissance instantanée normalisée calculée, la puissance dépendante du temps est obtenue par interpolation linéaire entre deux valeurs instantanées consécutives. Le dépôt d'énergie est calculé en intégrant la puissance du cœur et du crayon d'essai tout au long du transitoire.

L'observation principale est que le calcul dynamique sous-estime légèrement les résultats de l'approche *stepwise*, qui est basée sur des calculs statiques. En moyenne sur le transitoire, le dépôt d'énergie dans le crayon d'essai est inférieur de 4% lorsqu'il est calculé avec le code dynamique. L'incertitude statistique sur le calcul de la puissance est de 2% (1σ). En comparant le flux pour la configuration critique du cœur, le flux calculé avec le module dynamique était inférieur de 3% au flux calculé par le module statique. Cet écart de 3% peut également être observé pour les taux de réaction, suggérant une erreur systématique qui devrait être prise en compte.

Une autre information importante qui peut être obtenue à partir du calcul de l'énergie est le taux de dépôt d'énergie tout au long du transitoire, plus spécifiquement, les différences dans le taux de dépôt d'énergie dans le cœur et la section d'essai. Avec $E_{rate,n}$ l'énergie déposée au cours du pas de temps n et E_0 l'énergie déposée dans le premier pas de temps, le taux de dépôt d'énergie au temps n est calculé comme suit:

$$E_{rate,n} = \frac{E_n/dt_n}{E_0/dt_0} \qquad \text{(Eq. 1)}$$

La Figure 7 illustre le taux de dépôt d'énergie dans le cœur et dans le crayon d'essai dans l'approche *stepwise*. On peut observer qu'à mesure que le transitoire progresse le de dépôt d'énergie dans le cœur est plus important que dans le crayon d'essai. À la fin du transitoire, le taux de dépôt d'énergie est près de 2% plus élevé dans le cœur que dans le crayon d'essai.

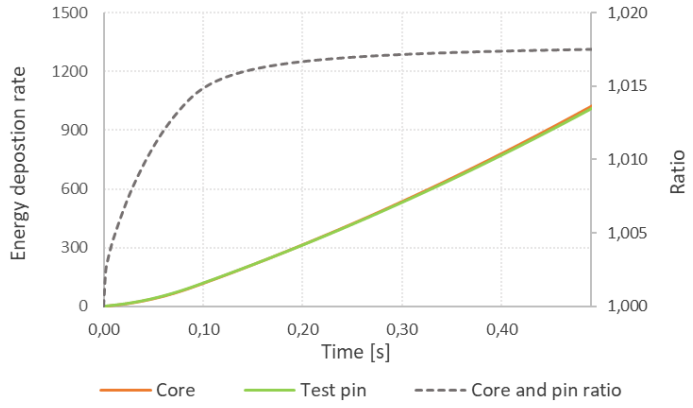


Figure 7. Taux de dépôt d'énergie dans le cœur et dans le crayon d'essai pendant le transitoire. Résultats obtenus avec le module statique

Transitoire surcritique-prompt

Le dépôt d'énergie le plus important se produit pendant le pulse de puissance. Pour 345 MJ déposé dans le cœur, 0,62 MJ est déposé dans le crayon d'essai. Lorsque l'on examine le taux de dépôt d'énergie dans le cœur et dans le crayon d'essai, illustré Figure 8, les mêmes observations que pour le transitoire surcritique peuvent être faites : le taux de dépôt d'énergie dans le cœur est plus élevé que dans le crayon d'essai et cette différence évolue pendant le transitoire. La différence relative entre le taux de dépôt d'énergie dans le cœur et dans la section d'essai augmente de 4% pendant le transitoire, ce qui signifie qu'à mesure que le transitoire progresse, il y a relativement plus d'énergie déposée dans le cœur que dans le crayon d'essai.

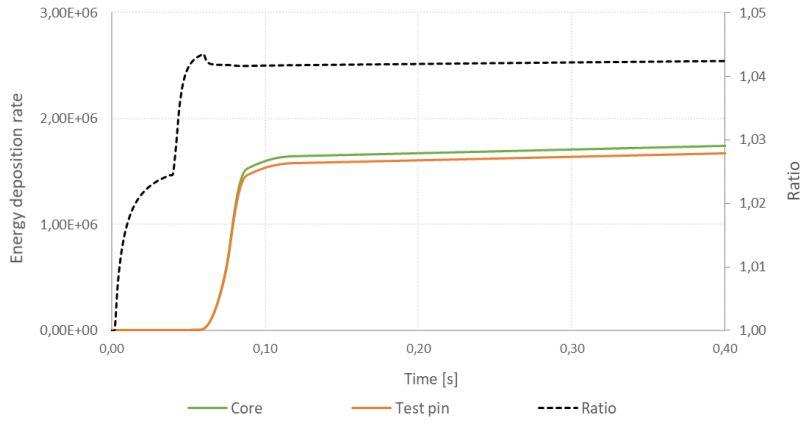


Figure 8 Taux de dépôt d'énergie dans le cœur et dans le crayon d'essai pendant le transitoire. Résultats obtenus avec le module statique

Les paramètres ayant une influence sur le dépôt d'énergie transitoire peuvent être séparés en paramètres expérimentaux, physiques ou de calcul. Les paramètres expérimentaux comprennent la pression d'hélium, la cinétique de dépressurisation (simple ou double dépressurisation, temps d'ouverture des vannes, etc.) et les caractéristiques du crayon d'essai (type de combustible et taux d'irradiation). Les paramètres physiques comprennent les différentes termes d'antiréactivité. En ce qui concerne les paramètres de simulation, ceux-ci comprennent la discrétisation géométrique du combustible (composition isotopique et température), la méthodologie de calcul (dépôt d'énergie estimé à partir des énergies de fission ou basé sur les échauffements nucléaires) et le choix delà bibliothèque de données nucléaires.

L'impact des paramètres expérimentaux et physiques a été étudié au cours de ce travail. La principale conclusion est que la dépressurisation de l'hélium a le plus important impact sur la variation du taux de dépôt d'énergie. Un autre paramètre qui pourrait avoir un impact significatif sur le dépôt d'énergie entre le cœur et le crayon d'essai est le type de crayon d'essai, plus précisément sa composition isotopique. La composition isotopique est définie à la fois par le type de combustible (UO_2 ou MOX) et le taux de combustion du crayon. La Figure 9 présente l'évolution du rapport du taux de dépôt d'énergie dans le cœur et dans le crayon d'essai pour les différents types de crayons. Au début du transitoire, le taux de dépôt d'énergie est similaire pour les différents crayons. L'impact des différentes compositions isotopiques devient apparent avec l'augmentation des températures. Vers la fin du transitoire, le taux de dépôt d'énergie est plus faible pour les combustibles MOX que pour les combustibles UO_2, et pour les combustibles irradiés que pour les combustibles non-irradiés.

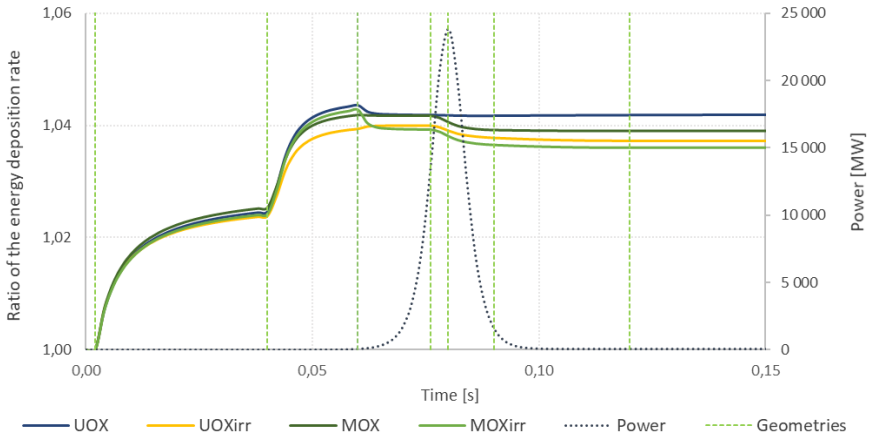


Figure 9. Différence relative des taux de dépôt d'énergie entre le cœur et les différents crayons d'essai

Impact des échauffements nucléaires sur l'estimation du dépôt d'énergie

L'hypothèse principale du calcul du dépôt d'énergie basé sur les énergies de fission est que toute l'énergie générée pendant la fission est déposée là où la fission a lieu. L'objectif de cette étude est de calculer l'échauffement nucléaire dans le crayon d'essai afin de définir la proportion de l'énergie de fission générée dans le crayon d'essai qui se dépose en dehors de celui-ci. Cette proportion est appelée facteur de distribution d'énergie. On évalue également si cette proportion change pendant le transitoire et si elle dépend du type de combustible.

La majeure partie de l'énergie déposée dans le crayon d'essai (~95%) est l'énergie déposée par les particules créées dans le crayon. L'échauffement provenant du cœur représente, selon le type de combustible, 1 à 2% du dépôt d'énergie total. Cette contribution a également été évaluée pour différentes configurations de base et a été jugée constante. Les résultats ont montré qu'environ 11% de l'énergie de fission générée dans le crayon d'essai est effectivement déposée à l'extérieur du crayon. Ce rapport ne change pas pendant la dépressurisation, mais il change en fonction du type de crayon d'essai. Les calculs suggèrent que ce rapport augmente avec l'augmentation de la teneur en matière fissile. Pour les crayons d'essai considérées dans cette étude (UO_2 et MOX frais et irradiés, avec des enrichissements de 6% et 7%, respectivement), ce rapport varie entre 9 et 13%. En d'autres termes, l'estimation du dépôt d'énergie à partir des taux de réaction et des énergies de fission surestime le dépôt d'énergie total dans le crayon d'essai, et un facteur de correction approprié, correspondant au facteur de distribution d'énergie, devrait y être appliqué.

Facteur de couplage

Le facteur de couplage est un paramètre important qui peut être utilisé pour calculer le dépôt d'énergie dans le crayon d'essai en fonction de l'énergie déposée dans le cœur. Plusieurs facteurs de couplage sont définis dans cette section :

- *Le facteur de couplage constant* désigne le facteur de couplage correspondant à la configuration critique du cœur au début du transitoire
- *Le facteur de couplage instantané*, calculé pour chaque configuration choisie
- *Le facteur de couplage stepwise* est calculé par interpolation entre deux facteurs de couplage instantanés
- *Le facteur de couplage dynamique* est donné en divisant la puissance dynamique du cœur et du crayon d'essai
- *Le facteur de couplage révisé* est calculé à partir du facteur de couplage *stepwise* et du facteur de distribution d'énergie

Comme le montrent les résultats précédents, les variations du facteur de couplage pendant le transitoire et son évolution sont principalement déterminées par la variation de la pression d'hélium et par l'augmentation de la température du combustible. L'impact de la variation du

facteur de couplage sur le calcul du dépôt d'énergie dans le crayon d'essai peut être illustré en comparant le dépôt d'énergie total dans le crayon d'essai obtenu avec le facteur de couplage constant, représentatif de la configuration critique du cœur, et obtenu avec le facteur de couplage *stepwise*. Les résultats montrent que l'utilisation du facteur de couplage constant entraîne une surestimation de l'énergie déposée dans le crayon d'essai. Pour une simple ou double dépressurisation à partir de 11.5 bar, cette surestimation est de l'ordre de 6%. Cela souligne que le facteur de couplage à l'état stationnaire n'est pas représentatif du cœur, plus précisément de la distribution d'énergie entre le cœur et le crayon d'essai, pendant le pulse de puissance où environ 85% du dépôt d'énergie se produit.

Ainsi, la notion de facteur de couplage révisé peut être introduite, qui tient compte à la fois de la variation du facteur de couplage, via le facteur de couplage *stepwise* ($C_{stepwise}(t)$) et de la différence entre l'énergie générée et déposée via le facteur de correction (F_C), défini en fonction du facteur de distribution d'énergie. Ce facteur de couplage révisé peut être défini comme suit :

$$C_{revised}(t) = C_{stepwise}(t) \cdot F_C \quad (1)$$

$$F_C = F_{out} + 1 \quad (2)$$

L'impact de la variation du facteur de couplage sur le calcul du dépôt d'énergie pour le crayon d'essai peut être illustré en comparant le dépôt d'énergie obtenu avec le facteur de couplage en régime permanent et le facteur de couplage révisé, comme résumé dans le Table 1 pour une simple et une double dépressurisation à partir de 11.5 bar. Cette étude montre que l'utilisation du facteur de couplage en régime permanent entraîne une surestimation de 20% du dépôt d'énergie dans le crayon d'essai pour ces dépressurisations.

	DEPRESSURIZATION SIMPLE		**DOUBLE DEPRESSURIZATION**	
	Dépôt d'énergie	Variation relative	Dépôt d'énergie	Variation relative
Facteur de couplage constant	0.55 MJ ± 0.31%	-	0.54 MJ ± 0.31%	-
Facteur de couplage révise	0.46 MJ ± 0.31%	-20%	0.45 MJ ± 0.31%	-20%

Table 1. Dépôt d'énergie dans un crayon UO_2

Conclusion

Ces dernières années, la simulation des pulses de puissance CABRI a connu un développement significatif. Ces outils de calcul visaient à un calcul plus précis des pulses de puissance et à la mise en œuvre d'une approche multiphysique. Comme approche complémentaire, ce travail actuel vise à améliorer la capacité de prédiction de certains paramètres d'intérêt des transitoires CABRI.

La transition entre le calcul de Monte Carlo statique et dynamique est réalisée progressivement, en développant deux méthodologies. Deux transitoires sont considérés, un transitoire surcritique, qui permet de comparer les résultats des schémas de calcul *stepwise* et dynamiques, et un transitoire surcritique prompt qui permet une analyse approfondie du processus de dépôt d'énergie. Les géométries représentatives sont choisies en fonction de l'évolution des paramètres physiques (pression et température) et des caractéristiques du pulse de puissance. Il a été constaté qu'une dizaine de géométries suffisent à couvrir un transitoire, et que plus de 15 géométries devraient être évitées en raison des limites de mémoire et de temps de fonctionnement. En ce qui concerne les pas de temps, dans la phase de cinétique rapide, ils doivent être de l'ordre du temps de vie des neutrons, tandis que dans la phase de cinétique lente, des pas de temps de 0,1 s suffisent.

L'analyse a montré que ce schéma de modélisation est capable de reproduire correctement l'injection de réactivité en la comparant aux résultats obtenus avec la cinétique ponctuelle. Cependant, les résultats ont également révélé que le module cinétique mis en œuvre dans TRIPOLI-4® est seulement capable de calculer l'évolution de la puissance dans le cas surcritique, mais pas pour les transitoires surcritiques prompts. Néanmoins, dans le cas du transitoire surcritique, les résultats obtenus avec la méthodologie par étapes sont en bon accord avec les résultats du calcul dynamique et expérimentaux. La validation de la modélisation transitoire est complétée par une analyse de sensibilité sur le calcul de la puissance dynamique du transitoire surcritique. L'étude de sensibilité se concentre sur l'impact des incertitudes des paramètres d'entrée expérimentaux et de modélisation sur le calcul de la puissance. L'analyse a montré que parmi les paramètres considérés, le calcul de la puissance est principalement sensible à l'incertitude sur la pression.

La deuxième partie du travail est consacrée au dépôt d'énergie dynamique. Bien qu'il existe des approches différentes pour estimer le dépôt d'énergie, il est dérivé dans chaque cas de la même quantité physique : le flux neutronique. La distribution et l'évolution du flux neutronique ont été analysés pour les simulations *stepwise* et dynamique pour le cas surcritique et pour les simulations *stepwise* dans le cas des transitoires surcritiques prompts. Afin d'être en mesure de capturer des effets plus fortes, un nouveau transitoire, une simple dépressurisation de 11,5 bar a été envisagée. Les résultats montrent que l'évolution du flux radial est principalement induite par la pression de l'hélium. Dans les cas considérés, le flux a augmenté autour des barres transitoires jusqu'à 40 % après la dépressurisation.

Plus important encore, l'augmentation du flux dans la périphérie (où les crayons transitoires sont situées) est plus importante que l'augmentation du flux dans le centre du cœur (où le crayon d'essai est situé). En d'autres termes cela suggère que contrairement aux hypothèses de calcul actuelles, il y a relativement plus d'énergie déposée dans le cœur nourricier que dans la section d'essai. On a également observé que, bien que le spectre de flux soit plus dur dans le cœur que dans la boucle à eau pressurisée, il ne varie pas pendant la dépressurisation. En ce qui concerne la comparaison des schémas de calcul, le calcul dynamique et le calcul statique sont capables de reproduire la forme du flux à différents stades du transitoire avec un bon accord. Le module dynamique semble cependant sous-estimer le flux absolu de 3%.

Deux limites du schéma de calcul actuel ont été identifiées et quantifiées : l'impact du schéma de dépôt d'énergie et l'hypothèse d'un facteur de couplage constant. Dans le schéma de calcul actuel, toute l'énergie de fission générée est considérée comme étant déposée dans le crayon d'essai. La répartition spatiale réelle de l'énergie de fission est prise en compte dans le schéma de l'échauffement nucléaire et est représentée par le facteur de distribution d'énergie. Pour les crayons considérés dans cette étude celui-ci varie entre 9 et 14% et il comprend la partie de l'énergie générée dans le crayon d'essai qui est déposée à l'extérieur du crayon et la compensation d'énergie due aux particules arrivant du cœur. Ce facteur ne change pas pendant la dépressurisation, et les calculs montrent que ce rapport augmente avec l'augmentation du contenu fissile.

L'énergie déposée dans le crayon peut également être calculée à l'aide du facteur de couplage, qui décrit la distribution d'énergie entre le cœur et le crayon d'essai, et qui est, dans la méthodologie actuelle, définie pour la configuration de cœur critique et considérée comme constante. L'impact de cette dernière hypothèse a pu être observé en utilisant le schéma de calcul *stepwise*, le dépôt d'énergie étant calculé à partir des énergies de fission. Les calculs ont révélé que le facteur de couplage augmente pendant le transitoire (de 6% pour la dépressurisation de 11,5 bar) et que sa variation est impactée par la variation de pression d'hélium en premier rang, et par l'effet Doppler en effet secondaire. Cela signifie également que le changement le plus important du facteur de couplage se produit avant le pic de puissance, c'est-à-dire que le facteur de couplage correspondant à l'état critique n'est en fait pas représentatif de l'impulsion de puissance. Ceci est particulièrement important car la majorité du dépôt d'énergie se produit pendant le pulse.

En d'autres termes, l'estimation du dépôt d'énergie à partir des taux de réaction et des énergies de fission et l'hypothèse d'un facteur de couplage constant surestiment tous deux le dépôt d'énergie total dans le crayon d'essai. Afin de prendre en compte la variation du facteur de couplage et la correction provenant de la distribution spatiale du dépôt d'énergie, le facteur de couplage révisé a été défini, qui correspond au facteur de couplage *stepwise* pondéré par le facteur de distribution d'énergie. Les résultats ont montré que l'utilisation du facteur de couplage en régime permanent pouvait entraîner une surestimation de près de 20% de l'énergie déposée dans la broche de test (selon le transitoire et le type de crayon d'essai). Ainsi,

les travaux présentés dans cette thèse permettent de faire des recommandations sur la méthodologie de calcul des facteurs de couplage, ce qui peut in fine conduire à l'amélioration du calcul des dépôts énergétiques lors d'une expérimentation dans le réacteur CABRI.

PERSPECTIVES

Dans ce qui suit, quelques orientations seront données pour les développements futurs possibles couvrant les domaines suivants : modélisation de la broche d'essai, simulation Monte Carlo cinétique, modélisation multiphysique, calcul du facteur de couplage et validation de cette méthodologie de calcul.

Modélisation du crayon d'essai

Il existe plusieurs axes d'amélioration concernant la modélisation du crayon d'essai et de la boucle à eau pressurisée. Une prise en compte plus précise de l'évolution de la température du crayon d'essai pourrait influencer le facteur de couplage et donc le dépôt d'énergie.

Actuellement, les crayons d'essai sont modélisés avec une composition isotopique homogène et avec la même évolution de température axiale et radiale que les crayons du cœur nourricier. Cependant, par exemple dans le cas d'un combustible d'essai avec un taux de combustion élevé, la distribution uniforme initiale des isotopes fissiles est modifiée en raison de l'augmentation de la capture par neutronique à la périphérie de la pastille, entraînant une accumulation locale d'isotopes transuraniens à ce niveau (*rim region*). Par conséquent, le profil de température radial varie également au cours d'un transitoire. Le comportement du combustible, incluant les variations de température discrétisées axialement et radialement, pourrait être obtenu par un processus itératif avec le code ALCYONE, qui est capable de simuler le comportement du combustible suite à un dépôt d'énergie (Guénot-Delahaie, et al., 2018).

De plus, la boucle d'eau est modélisée dans ce travail comme ayant les mêmes conditions de fonctionnement (pression et température du modérateur) que le cœur nourricier. Afin d'avoir des effets Doppler et modérateur plus réalistes dans le crayon d'essai, la boucle à eau doit être modélisée dans ses conditions de pression et de température nominales. L'implémentation de la modélisation de la boucle d'eau sous pression dans PALANTIR, qui donnerait l'évolution des paramètres physiques dans la boucle d'eau, est en cours.

Simulation Monte Carlo cinétique

Concernant les perspectives pour la simulation Monte Carlo cinétique du réacteur CABRI, deux approches peuvent être distinguées, selon le choix du code Monte Carlo. Dans le cas de simulations transitoires avec TRIPOLI-4® des développements supplémentaires sont nécessaires pour pouvoir simuler des transitoires supercritiques prompts et pour résoudre

l'écart observé entre les valeurs de flux absolus du calcul de criticité et du calcul cinétique. De plus, le traitement de l'effet Doppler doit également être amélioré, par exemple en mettant en œuvre l'élargissement Doppler au vol ou en permettant l'interpolation de température.

Comme alternative, il pourrait être possible d'utiliser d'autres codes stochastiques pour modéliser les transitoires CABRI, comme le code Serpent 2, qui montre également un potentiel dans la simulation transitoire et dans le couplage multiphysique (Syrjälahti, et al., 2015) (Leppanen, 2013) (Aures, et al., 2021).

Couplage multiphysique

Le couplage d'un code Monte Carlo avec un code thermo-hydraulique ne semble pas être l'outil de simulation le plus adapté pour le moment, compte tenu du coût de calcul important et des difficultés observées dans les simulations transitoires supercritiques prompts. Ainsi, au CEA, les recherches actuelles s'orientent vers un couplage entre un code déterministe de transport neutronique (ici APOLLO3®) et un code thermohydraulique cœur et système. Une nouvelle thèse, ayant pour objectif de développer un tel couplage est actuellement en cours (Coissieux, et al., 2022)

Facteur de couplage dynamique

L'étude de la variation du facteur de couplage doit être étendue à d'autres types de transitoires. De plus, les études devraient être poursuivies pour trouver un nombre optimisé de géométries pour modéliser tout type de transitoire et pour cartographier tous les paramètres ayant un impact sur le dépôt d'énergie et le facteur de couplage, ainsi que pour quantifier leur importance.

À terme, un métamodèle pourrait être construit pour définir un facteur de couplage basé sur les paramètres du cœur (conditions de la boucle d'eau sous pression, température du combustible et du modérateur, position des barres de commande). De même, une fois le problème de sous-estimation de puissance résolu, l'analyse doit être étendue aux simulations dynamiques pour les transitoires supercritiques prompts.

Validation des méthodologies de calcul

Il est nécessaire d'effectuer des mesures de dépôt d'énergie pendant le transitoire dans le cœur et dans la le crayon d'essai pour valider expérimentalement le schéma de calcul présenté dans cette thèse. Le cœur de CABRI n'est pas encore équipé d'une instrumentation qui permette de mesurer ni le dépôt d'énergie dynamique dans le crayon d'essai, ni les variations du facteur de couplage. Dans cette optique, une thèse a été lancée récemment dans le but de développer des techniques de mesure et une instrumentation ad-hoc pour cartographier la distribution du flux pendant le transitoire, ouvrant à terme la voie à des mesures dynamiques de dépôt d'énergie.

TABLE OF CONTENT

Affidavit ii
Publications and conferences iii
Acknowledgments v
Abstract vii
Résumé viii
Résumé étendu ix
Table of content xxv
LIST OF FIGURES xxvii
LIST OF TABLES xxxi
LIST OF ACRONYMS xxxii
Introduction 1
1. CONTEXT 3
1.1. Nuclear fuel behavior during a reactivity insertion accident 3
1.1.1. Fuel safety criteria 3
1.1.2. RIA phenomenology 5
1.1.3. Research reactors with transient testing capabilities 8
1.2. The CABRI reactor 9
1.2.1. The CABRI core 10
1.2.2. The pressurized water loop 11
1.2.3. Test device and instrumentation 11
1.2.4. Reactivity insertion system 13
1.2.5. Specific reactor instrumentation 15
1.2.6. Experimental programs 18
1.3. Energy deposition calculation during an experiment in the CABRI reactor 19
1.3.1. Coupling factor definition 19
1.3.2. Steady-state and transient core power measurement 20
1.3.3. Steady-state and transient pin power measurement 21
1.3.4. Energy deposition calculation during a transient 22
2. METHODS AND OBJECTIVES 23
2.1. Theoretical background 23
2.1.1. Generalities 23
2.1.2. Neutron transport equation 27
2.1.2.1. Time-dependent transport calculation 27
2.1.2.2. Steady-state transport calculation 28
2.1.2.3. Point kinetics approximation 29
2.1.2.4. Quasi-static method 31
2.1.3. Fission energy and nuclear heating 31
2.2. Modelling a reactivity insertion accident 33
2.2.1. State of the art on transient simulation with Monte Carlo codes 33
2.2.2. State of the art on the simulation of the CABRI transient 34
2.2.3. Steady-state neutron transport 35

2.2.4. Non-stationary neutron transport 37
2.3. PhD thesis objectives 43
2.3.1. Energy deposition estimated from fission energies 43
2.3.2. Energy deposition based on nuclear heating 47
3. TRANSITION FROM A STEADY STATE TO A TRANSIENT CALCULATION 49
3.1. Modelling a CABRI transient 49
3.1.1. Definition of the representative geometries 50
3.1.2. Implementation of the dynamic module 53
3.2. Justification of the modelling choices 54
3.2.1. Power evolution calculated with point kinetics 55
3.2.2. Dynamic power evolution 57
3.2.3. Limitations of the dynamic module 59
3.3. Sensitivity study on the dynamic power calculation 62
3.3.1. Experimental parameters 62
3.3.2. Simulation parameters 65
3.4. Summary 67
4. FLUX DISTRIBUTION DURING A TRANSIENT 68
4.1. Evolution of the flux during a supercritical transient 68
4.1.1. Radial flux distribution 69
4.1.2. Axial flux distribution 73
4.1.3. Spectrum variation 74
4.2. Evolution of the flux during a prompt supercritical transient 75
4.2.1. Radial flux distribution 76
4.2.2. Axial flux distribution 80
4.2.3. Spectrum variation 81
4.3. Summary 81
5. ENERGY DEPOSITION INTO THE TEST PIN DURING THE TRANSIENT 82
5.1. Energy deposition into the test pin 82
5.1.1. Energy deposition estimated from fission energies 82
5.1.2. Impactful parameters on the energy deposition 87
5.1.3. Energy deposition estimated from nuclear heating 93
5.2. Coupling factor evolution during a transient 98
5.2.1. Coupling factor evolution during a supercritical transient 99
5.2.2. Coupling factor evolution during a prompt-supercritical transient 100
5.2.3. Impact of the fuel pin type on the coupling factor 102
5.2.4. Impact of the depressurization type on the coupling factor 103
5.2.5. Coupling factor and energy deposition 104
5.3. Summary 105
6. CONCLUSIONS AND PERSPECTIVES 107
BIBLIOGRAPHY 112
ANNEXES 116
ANNEX A. Power interpolation in the stepwise methodology 116
ANNEX B. Multiplicity and spectra calculation with DARWIN/PEPIN2 118

LIST OF FIGURES

Figure 1. Evolution des principaux paramètres lors de la dépressurisation supercritique. Résultats obtenus avec PALANTIR. Les lignes vertes verticales représentent les géométries choisies ..... *xii*

Figure 2. Evolution des principaux paramètres lors de la dépressurisation supercritique prompt. Résultats obtenus avec PALANTIR. Les lignes vertes verticales représentent les géométries choisies ..... *xiii*

Figure 3. Comparaison entre la puissance calculée et expérimentale dans le cas du transitoire surcritique. Incertitudes données à 1σ ..... *xiii*

Figure 4. Comparaison entre la puissance calculée et expérimentale dans le cas du transitoire surcritique prompt ..... *xiv*

Figure 5. Distribution radiale du flux dans la configuration critique du cœur (à gauche) et variation relative du flux à la fin du transitoire (à droite). Résultats obtenus avec le module dynamique ..... *xv*

Figure 6. Spectre du flux neutronique par unité de léthargie dans le cœur et dans le crayon d'essai dans la configuration critique du cœur, obtenu avec le module dynamique ..... *xv*

Figure 7. Taux de dépôt d'énergie dans le cœur et dans le crayon d'essai pendant le transitoire. Résultats obtenus avec le module statique ..... *xvii*

Figure 8 Taux de dépôt d'énergie dans le cœur et dans le crayon d'essai pendant le transitoire. Résultats obtenus avec le module statique ..... *xvii*

Figure 9. Différence relative des taux de dépôt d'énergie entre le cœur et les différents crayons d'essai *xviii*

Figure 10. Fuel dispersal mechanism (Rudling, et al., 2016) *5*

Figure 11. Possible fuel failure mechanisms (Rudling, et al., 2016) *6*

Figure 12. Evolution of the radial temperature profile during a RIA (Guénot-Delahaie, et al., 2018) *7*

Figure 13. CABRI reactor and main components (IRSN, 2021) *9*

Figure 14. The CABRI core *10*

Figure 15. Schematic view of the test device *11*

Figure 16. Instrumentation on the lower and upper part of the test device (IRSN, 2021) *12*

Figure 17. Reactivity insertion system *13*

Figure 18. Natural transients with fully opened control valve and different initial helium pressure. Higher helium pressure results in higher peak power and a shorter pulse *14*

Figure 19. Structured transients with the same initial helium pressure but different opening time for the second valve. Shorter opening sequence leads to higher power peak and shorter pulse *15*

Figure 20. Placement of the various detectors in CABRI *16*

Figure 21. Hodoscope detector system (Chevalier, et al., 2018) *17*

Figure 22. Radiative capture and fission cross-section for the ^{235}U isotope *25*

Figure 23. Simplified algorithm of particle history in Monte Carlo simulation (CEA, 2015) *36*

Figure 24. Time evolution of the total neutron flux in the CABRI core computed with TRIPOLI-4® with (green) and without (orange) rescaling the fission neutron number *38*

Figure 25. A schematic representation of a neutron chain with and without forced decay (Sjenitzer, 2013) *40*

Figure 26. Application of the combing method: The total weight of the 6 particles is redistributed over 4 particles, each with a weight of W/4 (Faucher, et al., 2018) *41*

Figure 27. Definition of the instantaneous and stepwise values *46*

Figure 28. Nuclear heating calculation scheme *47*

Figure 29. Radial cut of the CABRI core in the native TRIPOLI-4 geometry *49*

Figure 30. Evolution of the main parameters during the supercritical transient. Results obtained with PALANTIR. The vertical green lines represent the chosen core configurations. *52*

Figure 31. Evolution of the main parameters during the prompt supercritical depressurization. Results obtained with PALANTIR. Vertical green lines represent the chosen core configurations *53*

Figure 32. Power calculated with the point kinetics solver *55*

Figure 33. Power evolution obtained with PALANTIR and using point kinetics. Vertical lines represent the geometry changes *56*

Figure 34. Impact of the number of geometries on the power calculated with point kinetics *56*

Figure 35. Power evolution obtained with PALANTIR and using point kinetics *57*

Figure 36. Comparison between the calculated and experimental power in the case of the supercritical transient. Uncertainties given at 1σ *58*

Figure 37. Comparison between the calculated and experimental power in the case of the prompt supercritical transient *58*

Figure 38. Impact of the modelling parameters on the power evolution in the case of a prompt supercritical transient *61*

Figure 39. Power evolution for various pressure differences. Results obtained with kinetic TRIPOLI-4® and PALANTIR *64*

Figure 40. Impact of the reactivity feedbacks on the power evolution *65*

Figure 41. Sensitivity of the power calculation to the helium purity *65*

Figure 42. Impact of the rescaling factor on the power calculation *66*

Figure 43. Radial distribution of the flux in the critical core configuration (left) and the relative flux variation at the end of the transient (right). Results obtained with the dynamic module *69*

Figure 44. Relative difference between the static and dynamic flux distribution for the critical (left) and final (right) core configuration *70*

Figure 45. Statistical uncertainties on the flux in the critical core configuration for the dynamic (left) and static (right) calculation *70*

Figure 46. Relative variation in the fast (right) and thermal (left) flux between the initial and final core configuration *71*

Figure 47. Radial distribution of the fast (left) and thermal (right) flux in the critical core configuration. Results obtained with the dynamic module *71*

Figure 48. Relative difference between the static and dynamic flux distribution for the critical core configuration for the fast (right) and thermal (left) flux *72*

Figure 49. Relative difference between the static and dynamic flux distribution for the final core configuration for the fast (right) and thermal (left) flux *72*

Figure 50. Axial flux distribution in the test pin and in chosen assemblies in the critical core configuration. Computed with the dynamic module and normalized to 1 ..... *73*

Figure 51. Axial flux distribution computed with the static and dynamic module in the critical core configuration *74*

Figure 52. Neutron flux spectrum per lethargy unit in the core and test pin in the critical core configuration, obtained with the dynamic module *75*

Figure 53. Evolution of the main parameters of the prompt-supercritical transient. Results obtained with PALANTIR *76*

Figure 54. Radial flux distribution for the critical core configuration (left) and the relative variation in the flux following the depressurization (right). The neutron flux is normalized to 1 ..... *76*

Figure 55. Relative distribution of the thermal flux for the critical core and the relative variation of the thermal flux following the depressurization. The neutron flux is normalized to 1 ..... *77*

Figure 56. Relative distribution of the fast flux for the critical core and the relative variation of the fast flux following the depressurization. The neutron flux is normalized to 1 ..... *77*

Figure 57. Relative variation in the flux due to the Doppler feedback (left) and the helium depressurization (right) *78*

Figure 58. Schematic view of the quarter of the core (left), and corresponding assembly-wise temperatures in K (right) *79*

Figure 59. Relative variation in the flux between the discretized and non-discretized core temperatures. *79*

Figure 60. Axial flux distribution in the test pin and several fuel assemblies for the critical core configuration (left) and for the final core configuration (right). Flux normalized to 1 ..... *80*

Figure 61. Neutron flux spectrum per lethargy unit in the test pin and the core in the critical core configuration. Results obtained with the static module and normalized to 1 ..... *81*

Figure 62. Main parameters of the supercritical transient. Results obtained with the PALANTIR code. Vertical green lines represent the chosen geometries *83*

Figure 63. Energy deposition into the test pin, calculated with the static and dynamic module *84*

Figure 64. Energy deposition rate in the core and in the test pin during the transient. Results obtained with the static module *84*

Figure 65. Energy deposition rate in the core and in the test pin during the transient. Results obtained with the dynamic module 85

Figure 66. Evolution of the main parameters of the prompt-supercritical transient. Results obtained with PALANTIR 86

Figure 67. Test pin power and energy deposition during the prompt-supercritical transient 86

Figure 68. Energy deposition rate in the core and in the test pin during the transient. Results obtained with the static module 87

Figure 69. Energy deposition rate in the core and test pin and the relative difference in the energy deposition rate between the core and the test pin 89

Figure 70. Schematic view of the quarter core and the variation in the fission reaction rates between the two core configurations 89

Figure 71. Relative difference in the energy deposition rates between the core and the different test pins 91

Figure 72. Evolution of the parameters of the double depressurization. The vertical lines represent the geometries chosen to model the transient. Results are obtained with PALANTIR 92

Figure 73. Energy deposition into the test pin during the simple and double depressurization 92

Figure 74. Ratio of the energy deposition rate between the core and test pin for the simple (SD) and double (DD) depressurization 93

Figure 75. Delayed beta spectrum for the different isotopes and irradiation time. The spectrum is normalized to 1 95

Figure 76. Delayed gamma spectrum after a 0.2 s irradiation for the different fissile isotopes. The spectrum is normalized to 1 95

Figure 77. Delayed gamma spectrum after 1 hour of irradiation for the different fissile isotopes. The spectrum is normalized to 1 96

Figure 78. Coupling factor variation during the supercritical transient. Results obtained with the stepwise and dynamic methodology 99

Figure 79. Coupling factor variation during the prompt-supercritical transient. Results obtained with the stepwise calculation scheme 100

Figure 80. Coupling factor variation for different fuel pin types. The vertical lines represent the different core configurations 102

Figure 81. Coupling factor and helium pressure evolution during the simple (SD) and double (DD) depressurization 103

Figure 82. Stepwise power evolution obtained by linear interpolation between the instantaneous values 116

Figure 83. Updated stepwise core power evolution 117

LIST OF TABLES

Table 1. Dépôt d'énergie dans un crayon UO2 ..... *xx*

Table 1. Decomposition of the energy released during fission given in JEFF3.1.1. (Santamarina, et al., 2009) *32*

Table 2. Uncertainty of the input parameters *62*

Table 3. Test cases considered for the uncertainty calculation on the dynamic power *63*

Table 4. Total energy deposition in the case of different test pins *90*

Table 5. Energy deposition in the case of the studied depressurizations *91*

Table 6. Prompt power deposition into the test pin for different core configurations *97*

Table 7. Decomposition of the power deposition by spatial distribution and by prompt and delayed components for a fresh UO_2 fuel pin. Values normalized to 1 MW core power *97*

Table 8. Decomposition of the energy deposition by spatial distribution for the critical core configuration, normalized to 1 MW core power *98*

Table 9. Helium pressure, fuel temperature and instantaneous coupling factor for the different core configuration of the 11.5 bar transient *101*

Table 10. Steady-state coupling factor for different test pins *102*

Table 11. Energy deposition into a fresh UO_2 test pin calculated from the energy deposition in the core and the different coupling factor values *104*

LIST OF ACRONYMS

ACRR	Annular Core Research Reactor
BIGR	Bystry Impulsny Graphitovy
BU	Burnup
CATHARE	Code for Analysis of Thermal-hydraulics during an Accident of Reactor and safety Evaluation
CEA	French Alternative Energies and Atomic Energy Commission (Commissariat à l'Energie Atomique et aux Energies Alternatives)
CIP	CABRI International Program
CPUh	Central Processor Unit hour
DBA	Design Basis Accidents
DD	Double Depressurization
DNB	Departure from Nucleate Boiling
ENDF	Evaluated Nuclear Data File
FOM	Figure of Merit
FWHM	Full Width Half Maximum
HBU	High burnup
HPMC	High Performance Monte Carlo Methods for Core Analysis
IAEA	International Atomic Energy Agency
IGR	Impulse Graphite Reactor
IRIS	Installation for Radiography, Imaging and Spectrometry
IRSN	French Institute for Radioprotection and Nuclear Safety (Institute de Radioprotection et de Sûreté Nucléaire)
JHR	Jules Horowitz Reactor
LMFRB	Liquid Metal Fast Breeder
LOCA	Loss of Coolant Accident
LWR	Light Water Reactor
MC	Monte Carlo
McSAFE	High Performance Monte Carlo Methods for Safety Analysis
MOX	Mixed Oxide
MTR	Material Testing Reactor
NEA	Nuclear Energy Agency
NSRR	Nuclear Safety Research Reactor
NURESAFE	Nuclear Reactor Safety simulation platform
OECD	Organization for Economic Co-operation and Development
PCMI	Pellet Cladding Mechanical Interaction
PALANTIR	Projet d'Amélioration des Lois et Approximations en Neutronique et Thermohydraulique pour les Insertions de Réactivité (Project for the Improvement of Laws and Approximations in Neutronics and Thermohydraulics for Reactivity Insertions)
PWR	Pressurized Water Reactor
RIA	Reactivity Injection Accident
REP	Réacteur à Eau Pressurisé

SCF	SUBCHANFLOW
SD	Simple Depressurization
SPARTE	Simulation Prediction and Analysis for RIA Transients and Excursions
SPERT	Special Power Excursion Reactor Tests
QPIRT	Quantitative Phenomena Identification and Ranking Table
TREAT	Transient Reactor Testing Facility
TRIPOLI	Tridimensionnel Poly-cinétique (3D Poli-kinetics)
UO_2	Uranium dioxide
U.S. NRC	United States Nuclear Regulatory Commission
VVER	Water Water Energetic Reactor

INTRODUCTION

Providing safe, reliable and economically viable energy is the cornerstone of nuclear energy production. The most important nuclear safety objective is to guarantee that the public is not exposed to radiological hazards originating from nuclear facilities. Accordingly, one of the main areas of interest of nuclear safety analysis is the behavior of nuclear fuel during operational and accidental situations as it constitutes the main radiation source in a power plant.

The majority of the existing fuel safety criteria were defined in the 1970s by the U.S. Nuclear Regulatory Commission and were based on experimental data from research reactors dedicated to fuel studies. These early fuel tests were focused on fresh or moderately irradiated fuel, in compliance with the average discharge burnup of the existing power plants. The data provided by these experiments showed that the degree of fuel pin damage is in correlation with the energy deposition in the fuel pin. As a consequence, it was defined as a main safety criterion. However, technological progress and research developments in core and fuel management motivated the use fuels with higher burnups or new designs. The lack of experimental data on these fuels led to new experimental programs in France, Japan and Russia in order to verify the adequacy of the regulatory acceptance criteria on fuel damage.

The pressurized water loop, providing representative reactor conditions during the test, the adjustable transient parameters, the versatility and the instrumentation of the test pins that can be used make CABRI, a pool-type pulse reactor owned and operated by the French Alternative Energies and Atomic Energy Commission, a unique research reactor in terms of fuel behavior studies under reactivity insertion conditions. In CABRI, the fuel pin to be examined is placed in a test loop in the center of the core and is subjected to a power transient obtained by the rapid depressurization of the helium-3 neutron absorber gas from the core.

In order to define the initial experimental parameters that would result in the sought transient while ensuring that the operational safety limits are respected, it is imperative to rely on specific computational tools and simulations. Modelling a reactivity insertion accident, an inherently multiphysics phenomenon, requires the coupling of 3D kinetics codes with thermal-hydraulic and fuel behavior codes. Until recently, non-stationary neutron problems, such as a reactivity insertion accident, were solved with deterministic methods, while the stochastic, or Monte Carlo, approach was used as a reference methodology for steady-state calculations.

In the context of the CABRI reactor, there were several efforts made lately in order to develop and validate deterministic simulation tools based on multiphysics modelling, including a neutron point kinetics model, to predict the power pulse and energy deposition during the transient (Clamens, 2018) (Labit, 2020). In recent years, increased computer power and advances in Monte Carlo methods have made it feasible to use stochastic codes to simulate non-stationary states. This is currently the subject of intensive research in particular for the Monte Carlo code TRIPOLI-4® developed at CEA (Sjenitzer, 2013), (Faucher, 2019).

In line with these research goals, the aim of this PhD thesis is to develop a non-stationary calculation methodology for the CABRI reactor that would allow computing the parameters of interest during a power pulse transient. This can pave the way towards multiphysics simulation of non-stationary conditions relying on 3D kinetics models. More precisely, the objective is to assess the dynamic energy deposition into the test pin and to study how the energy deposition rate changes during the power transient using a stochastic code such as TRIPOLI-4®.

The transition from static to dynamic simulations is achieved progressively, by developing two methodologies. The first methodology, referred to as the stepwise calculation scheme, is based on steady-state stochastic calculations. In this methodology, a criticality calculation is run for consecutive core configurations, representative of different stages of the transient. This allows the observation of the variations in the parameters of interest during the transient with the codes already at our disposal, and sheds a light on the most impactful parameters on the energy deposition rate. The fully dynamic simulation of the transient is obtained with the newly developed dynamic module of the TRIPOLI-4® code, which allows the simulation of non-stationary conditions (Faucher, et al., 2018). The aim of this simulation is twofold: to validate the energy deposition calculation scheme and to assess the kinetic module's capabilities.

This thesis report is organized in five chapters. The first chapter gives the context of the PhD thesis alongside a detailed presentation of the CABRI reactor and of the experiments conducted there. The theoretical background of the methodologies used during the work, as well as a state-of-the-art on the transient modelling, are summarized in the second chapter.

The implementation of the methodologies developed during this work to simulate the reactivity insertion transients typical of the CABRI reactor, is detailed in the third chapter. This chapter focuses on the transition from static to dynamic simulations and it includes the validation of the chosen modelling approach and the limitations of the kinetic module.

Chapter 4 and 5 are devoted to the analysis of the dynamic flux distribution and the calculation of the dynamic integral parameters, such as energy deposition into the test pin and core, with an emphasis on the definition of the dynamic coupling factor.

1. CONTEXT

1.1. Nuclear fuel behavior during a reactivity insertion accident

1.1.1. Fuel safety criteria

The most important nuclear safety objective, as defined by the IAEA, is to guarantee that the public is not exposed to radiological hazard originating from nuclear facilities (Nuclear Energy Agency, 2010). Accordingly, one of the main areas of interest of nuclear safety analysis is the behavior of nuclear fuel during operational and accidental situations, as it constitutes the main source of radiation in a power plant. In order to comply with the safety objectives, fuel criteria (safety, operational and design) are defined for both operational and accidental situations with the goal of preventing and mitigating the possible consequences of accidents.

The safety criteria are imposed by the regulatory body and ensure that the fuel damages during design basis accidents (postulated accidents that the reactor is designed to withstand) is within acceptable limits. The criteria can vary from country to country but they all aim to prevent cladding failure, fuel melting and pellet cladding interaction. In the case of reactivity insertion accidents, such as the transient type studied during this work, the safety requirements consist of demonstrating that there is no cladding failure, that only a limited number of fuels experience a boiling crisis and that there is no fuel melting or dispersal in the coolant (OECD, 2012).

The majority of the existing safety criteria was defined in the 1970s by the United States Nuclear Regulatory Commission (U.S. NRC), and was based on experimental data from research reactors dedicated to fuel studies. During these experiments, fuel pins were subjected to a RIA in order to study their behavior and to gain a better understanding of the possible fuel damage mechanisms that occur during these type of accidents. The data provided by these experiments showed that the degree of fuel pin damage is in direct correlation with the peak enthalpy value (Rudling, et al., 2016) stored in the pin, i.e. the energy deposited in the pin. Thus, the value of the radially averaged fuel enthalpy was chosen as a safety criterion.

The experiments showed that cladding fragmentation and fuel expulsion can be observed at an enthalpy value of 280 cal/g, corresponding to the melting of uranium fuel. Given that this amount of inserted energy also causes severe fuel pin deformation, which could lead to the loss of coolable geometry in a power plant, a lower enthalpy value of 230 cal/g was suggested as a more suitable safety limit (OECD, 2012). This value was implemented in most European power plants; in the US however, the 280 cal/g remained as the safety limit. In France, the safety

criteria were set independently for fresh fuel (<225 cal/g) and for irradiated fuel (< 200 cal/g) (OECD, 2012).

These early fuel tests were focused on fresh or moderately irradiated uranium dioxide (UO_2) fuel (up to 33 GWd/t) since the average discharge burnup in the existing power plants was around 40 GWd/t (Sartoris, et al., 2010). The impact of high burnup on safety criteria was emphasized in the findings of two independent experiments from France and Japan with highly irradiated fuel. Contrary to the expectations, in both experiments, REP-Na in the CABRI reactor in France, HBO-1 in NSRR in Japan, the high burnup fuel failure followed by fuel dispersal occurred at significantly lower enthalpies than the defined safety limit. In REP-Na1, the fuel with a burnup of 64 GWd/t failed at an energy deposition of 30 cal/g while in the case of HBO-1 fuel at 50 GWd/t, the cladding failed at an enthalpy value of 60 cal/g (OECD, 1995).

Simultaneously, the technological progress and the research developments in core and fuel management motivated the use fuels with higher burnup and new cladding design (such as Zirlo, an advanced zirconium based alloy developed by Westinghouse (Westinghouse, 2021). This led the authorities to initiate new experimental programs in France, Japan and Russia in order to verify the adequacy of regulatory acceptance criteria on fuel damage for high burnup PWR fuels, both UO_2 and mixed oxide (MOX) fuel.

In 1996, the OECD Nuclear Energy Committee on the Safety of Nuclear Installation decided to review the existing fuel safety criteria around the world in order to comply with the need of an adequate technical basis for nuclear safety criteria, focusing on new fuel designs and high burnup fuel. The resulting reports, (Nuclear Energy Agency, 2010) (OECD, 2012) (OECD, 2013), outlined the process for re-assessment of fuel criteria: the development of best-estimate analysis methods while simultaneously performing experimental studies to validate the best estimate codes and to verify the basis for safety criteria (Rudling, et al., 2016).

The French Institute for Radioprotection and Nuclear Safety (IRSN) implemented the same methodology, as outlined in (Sartoris, et al., 2010). Based on experimental results, a revised safety limit has been determined for fuels with a high burnup (enthalpy lower than 57 cal/g for a burnup between 47 and 58 GWd/t), while for fuels with intermediate burnup (33-47 GWd/t) the safety limits are currently being evaluated (Yamauchi, 2018).

1.1.2. RIA phenomenology

The term Reactivity Initiated Accident (RIA) refers to nuclear accidents involving a sudden and unexpected reactivity increase in the core. The events leading to involuntary reactivity insertion can be classified as control system failures, for example control rod ejection, core overcooling, such as a Main Steam Line Break in PWR, and events caused by boron dilution (Rudling, et al., 2016). These scenarios have been categorized as design basis accidents.

A RIA is characterized by an extremely rapid power excursion with significant energy deposition into the fuel assemblies surrounding the perturbation (the ejected rod for example). Depending on the amount of inserted reactivity, the fuel pins may fail, leading to release of radioactive material in the primary coolant, as shown in Figure 10. Hot fuel and fission gas dispersion in the coolant results in rapid steam generation. Due to the vaporization, the pressure increases around the failed cladding and depending on the amount of ejected fuel mass, the generated pressure wave can damage the surrounding pins as well (Sartoris, et al., 2010).

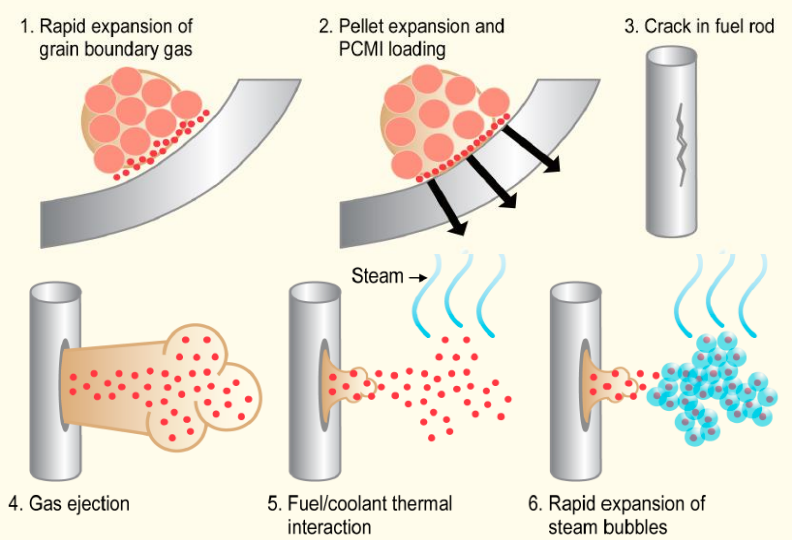


Figure 10. Fuel dispersal mechanism (Rudling, et al., 2016)

This type of accident can be divided into two phases. In the first stage, due to the reactivity insertion and swift power increase, the temperature of the fuel can increase significantly (10^3 to 10^4 K/s), leading to a quasi-adiabatic heating in the fuel pellet (Papin, et al., 1996). As a result, the fuel pellet undergoes a thermal expansion leading to a strong pellet cladding mechanical interaction (PCMI). This phase lasts a few milliseconds, until the Doppler effect terminates the power increase. Given the short time span, there is no heat exchange between the fuel pin and the cladding. The PCMI can induce cladding fracture.

During the second phase, as the heat transfer progresses between the fuel pin, cladding and coolant, the temperature of the cladding can reach temperatures high enough for a boiling

crisis to occur. The boiling crisis, also known as departure from nucleate boiling, implies the formation of a vapor film on the surface of the cladding once the coolant reaches its saturation temperature. This significantly degrades the cladding to coolant heat transfer and causes the cladding to overheat. The overview of the possible fuel failures is shown in Figure 11.

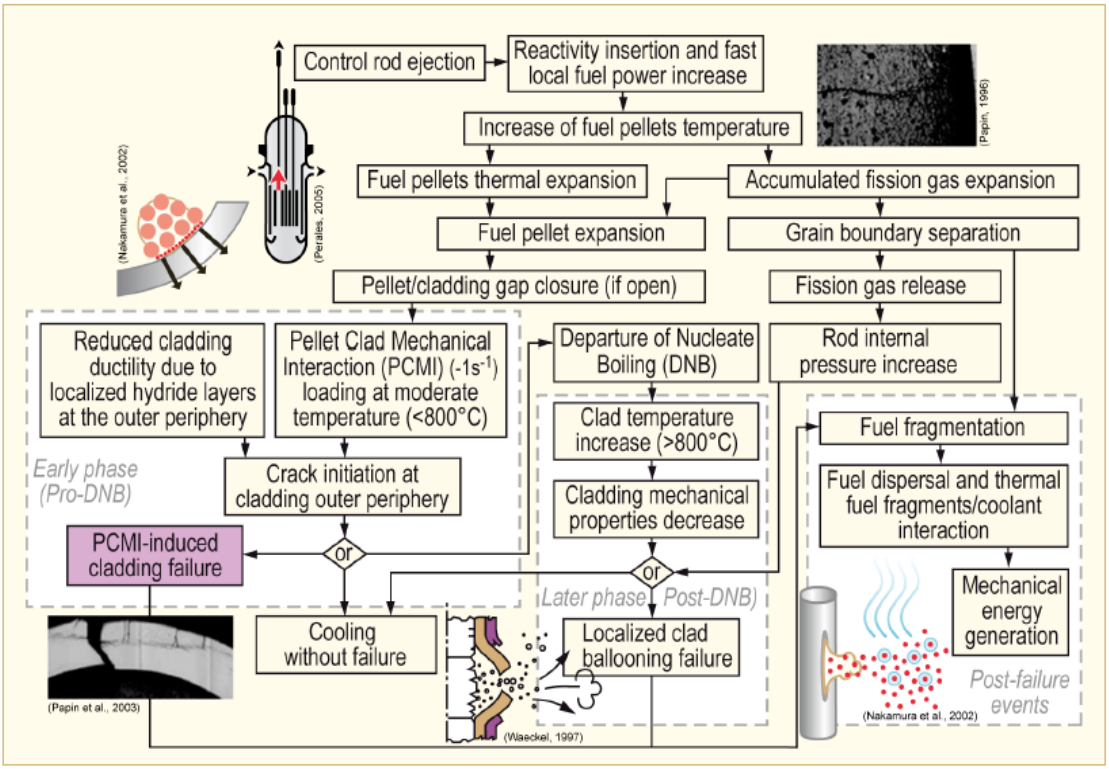


Figure 11. Possible fuel failure mechanisms (Rudling, et al., 2016)

The fuel experiments show that, besides the core coolant conditions and the main characteristics of the power pulse, such as the amplitude and length, the most impactful factor on the fuel failure mechanism during RIA is the burnup of the fuel (Moal, et al., 2018). Irradiation introduces changes in the structure of both the fuel pellet and cladding, and these changes are predominantly detrimental to safety.

Most of the thermo-physical properties of the fuel pellet, such as the thermal conductivity and the melting temperature decrease significantly under irradiation. At the same time, the initial uniform fissile material distribution changes under irradiation due to the enhanced neutron resonance capture on the pellet periphery. This leads to an increased local buildup of transuranium isotopes at the pellet outer ring, called the rim region (CEA, 2009). During the transient, the presence of the rim region influences the radial power and temperature distribution in the pellet, resulting in significantly higher temperatures in the rim zone as opposed to the other fuel regions, as shown in Figure 12. In addition, the rim zone is characterized by reduced grain size and increased porosity, which increase the possibility of fuel ejection in the case of cladding failure.

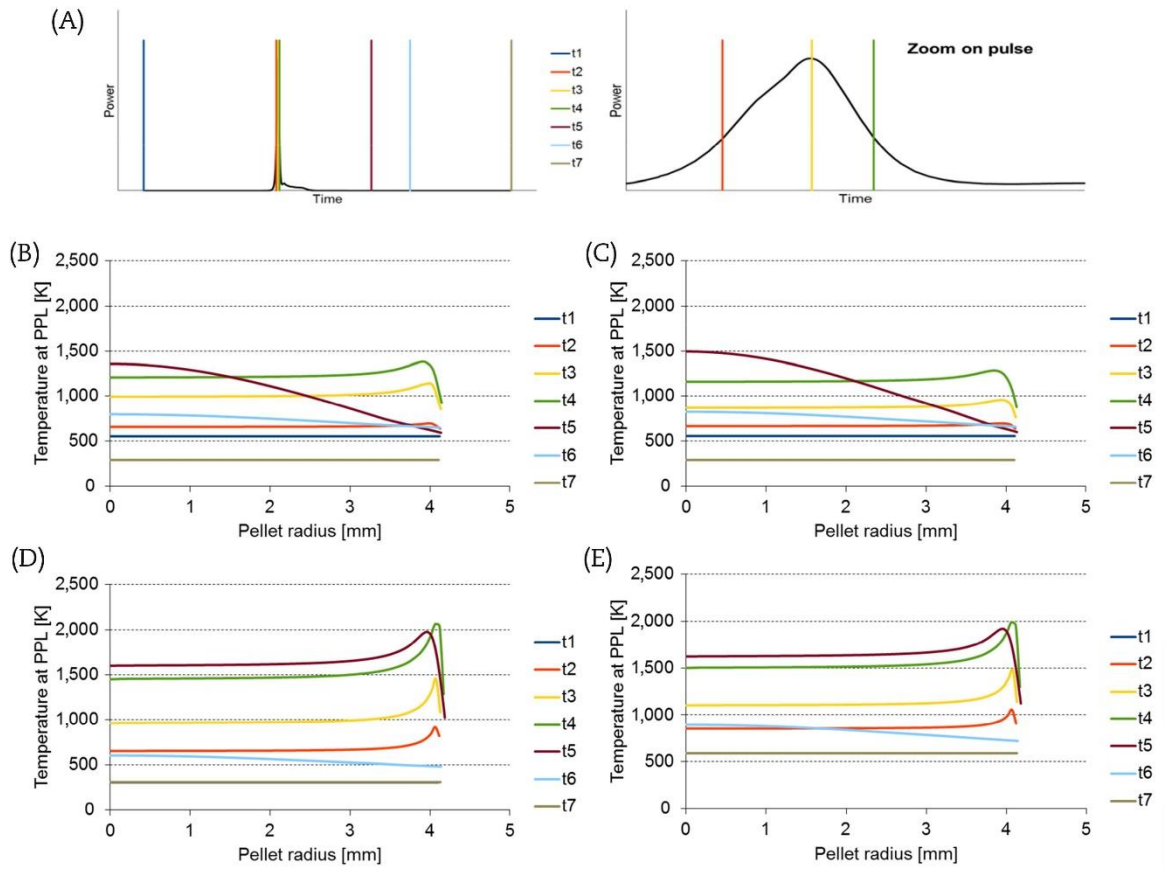


Figure 12. Evolution of the radial temperature profile during a RIA (Guénot-Delahaie, et al., 2018)

The buildup of gaseous fission products or fission gases during irradiation also has a significant impact on the fuel behavior. If the fission gases remain in the fuel pellet, they contribute to fuel swelling. Aggravated by the presence of the rim zone, fission gas accumulation significantly increases the risk of early failure by PCMI. If the fission gas is released from the fuel pellet, the internal pressure increase enhances the possibility of cladding ballooning in the later stage of RIA (Papin, et al., 1996). Radiation damage and the waterside corrosion, along with the subsequent oxidation and hydrogen absorption have been shown to reduce the ductility of the cladding leading to embrittlement. Analysis of the fuel experiments shows that the combined effect of cladding embrittlement and corrosion is the main attributor to high burnup failure modes.

To date more than 1000 experiments have been carried out with fresh fuel and 140 with highly irradiated fuel. The experiments showed that in the case of fresh fuel the severity of fuel damage is dependent of the fuel pellet enthalpy and the possible damage mechanisms are due to the high temperature the cladding can reach during an accident. Irradiated fuels however, tend to fail in the early phase of the RIA at low cladding temperature, as a result of previous irradiation damage.

These experimental programs have been performed in specific research reactors capable of reproducing reactivity insertion accidents. The description of these research reactors and of the main experimental programs are provided in the following section.

1.1.3. Research reactors with transient testing capabilities

Specific research reactors are capable of simulating reactivity insertion accidents in order to study the behavior of given components. The transient research reactors used for RIA simulation and fuel behavior studies are the following (Imholte & Aydogan, 2016):

1. *Transient Reactor Testing Facility (TREAT), USA* – designed by the Argonne National Laboratory and operated by the Idaho National Laboratory, operated since 1959, including a standby shutdown between 1994 and 2017
2. *Special Power Excursion Reactor Tests (SPERT), USA* – a series of destructive transient tests run by Phillips Petroleum Company between 1954 and 1963
3. *Annular Core Research Reactor (ACRR), USA* – developed by the Sandia National Laboratory in 1978, is operating to present day
4. *Nuclear Safety Research Reactor (NSRR), Japan* – owned by the Japanese Atomic Energy Agency and operated by the Tokai Research Establishment is currently under temporary shutdown, having been operated between 1980-2011
5. *CABRI reactor, France* – operated by The French Alternative Energies and Atomic Energy Commission (CEA) between 1963 and 2002 and since 2015, following a 13 year refurbishment period
6. *Impulse Graphite Reactor (IGR), Kazakhstan* – owned by Kazakhstan's National Nuclear Center and operated by the Institute for Atomic Energy since 1961
7. *Bystry Impulsny Graphitovy Reaktor (BIGR), Russia* – owned by the Rosatom State Atomic Energy Corporation and operated by the All-Russian Scientific Research Institute for Experimental Physics, is operational since 1977

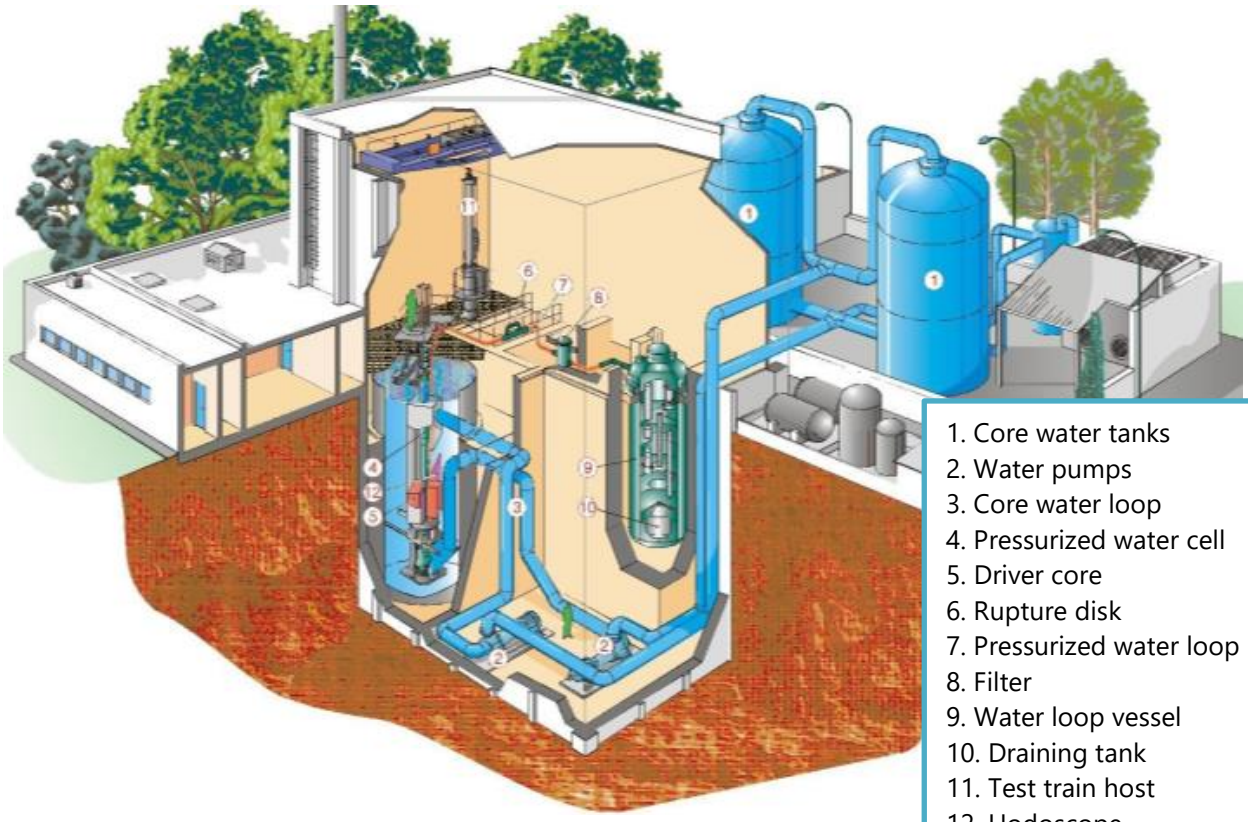
The experiments performed in the TREAT reactor were focused on fast reactor fuels, namely on fuel failure and fuel coolant interaction, whereas advanced reactor fuels (experimental and space reactor fuels) are tested in ACRR. Experiments in the NSRR were conducted with fresh and irradiated LWR fuels, with a burnup up to 50MWd/kgU (Fuketa, et al., 1996). In the case of the CABRI reactor, the initial research program was focused on metallic fuels, while the subsequent experiments were aimed at LWR fuel behavior. The experimental results from the IGR facility assisted the development of Liquid Metal Fast Breeder Reactors (LMFBR), while VVER and high burnup UO_2 fuel behavior was tested in BIGR (Imholte & Aydogan, 2016).

The pressurized water loop, providing representative PWR conditions during the test, the adjustable transient characteristics, the versatility of the test pins that can be used and

advanced instrumentation of the core make CABRI a unique research reactor in terms of fuel behavior studies in RIA conditions.

1.2. The CABRI reactor

The CABRI experimental pool-type pulse reactor is owned and operated by the French Alternative Energies and Atomic Energy Commission (CEA) and is located at the Cadarache research center. It is used to simulate power transients typical of reactivity initiated accidents in order to study the behavior of nuclear fuel pins in accidental situations. These studies are essential to justify the safety criterion of nuclear fuels used in commercial reactors, which is correlated to the energy deposition into the pin. The fuel pin (test pin) to be examined is placed in a test loop in the center of the CABRI core and it is subjected to a power transient. The power excursion is obtained by the rapid depressurization of the helium-3 neutron absorber gas from the transient rods located in the reactor core.



1. Core water tanks
2. Water pumps
3. Core water loop
4. Pressurized water cell
5. Driver core
6. Rupture disk
7. Pressurized water loop
8. Filter
9. Water loop vessel
10. Draining tank
11. Test train host
12. Hodoscope

Figure 13. CABRI reactor and main components (IRSN, 2021)

The reactor, built in 1964, was equipped with a sodium loop in 1977 in order to conduct safety studies related to sodium cooled fast reactors. The sodium loop was also used to study PWR fuel behavior during reactivity accidents. In 2000, a new research direction was defined with the aim of studying fuel behavior in conditions representative of PWRs. To comply with the

new requirements, the sodium loop was replaced by a pressurized water loop. The current design is shown in Figure 13.

1.2.1. The CABRI core

The reactor core (see Figure 14) is composed of 1487 UO_2 fuel pins arranged into 40 fuel assemblies. Given that the assemblies have to withstand multiple power transients, the cladding is made of stainless steel, a material more resistant to transient conditions than the standard Zircaloy. However, stainless steel has also a higher neutron absorption rate, thus the ^{235}U enrichment in the fuel reaches 6%, to compensate for the reduction in the neutron flux. Due to the low operational time of the reactor, the fuel in the driver core is considered to be fresh. The maximum steady-state power is 25 MW and the reactivity control is assured by 6 control rod assemblies, each one containing 23 natural hafnium pins.

The core cooling is ensured by water at ambient pressure and in natural convection for power levels up to 100 kW or in forced convection in the case of higher power levels. A pressurized water loop that contains the test device passes through the center of the core. The core is crossed by the irradiation channel of the hodoscope, a device meant to both monitor the test pin movements and provide a real time power profile for the test pin. The power transients are generated by the reactivity insertion system, which is composed of 4 transient assemblies, a system unique to this reactor. The compact core (60x60x80 cm) is surrounded by an outer graphite reflector block and is submerged in the reactor pool. Description of the main components and instrumentation of the CABRI core are given in the following sections.

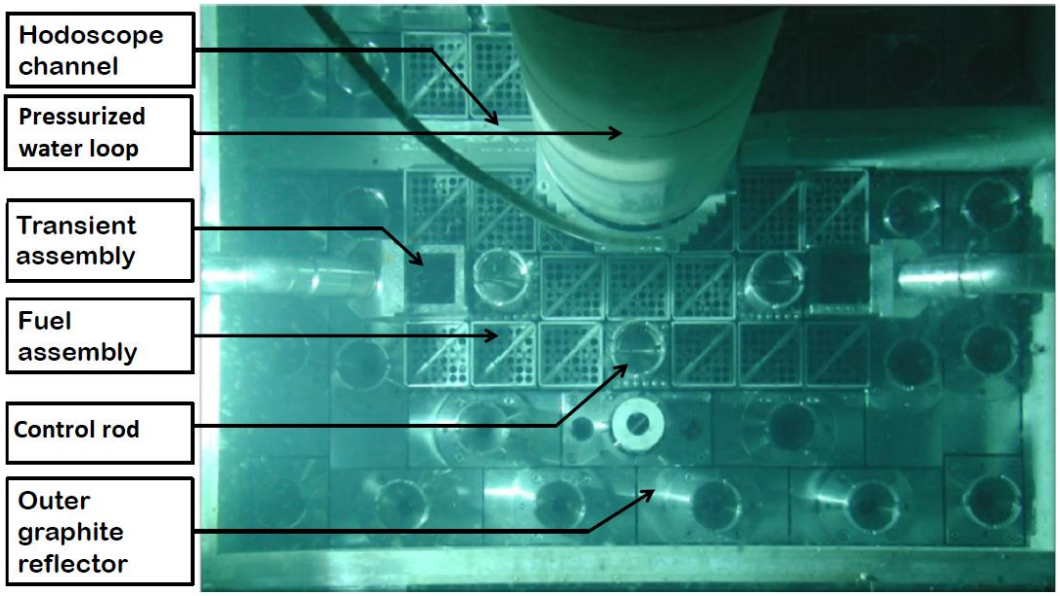


Figure 14. The CABRI core

1.2.2. The pressurized water loop

The pressurized water loop is a separate water loop that passes through the center of the core and contains the test pin. The function of this water loop is to house the test pin and its instrumentation while providing conditions representative of those found in a PWRs, coolant at 155 bar and 280°C with a 4 m^3/s flow rate. There are two main parts of the water loop: the in-pile pressurized water cell, which contains the test device and the test pin, and the out-of-pile containment, which surround the components that produce the necessary thermal-hydraulic conditions (pressurizer, circulation pump, heat exchanger, relief tank etc.).

The instrumentation that the test device is equipped with allows the measurement of flow, pressure, temperature, axial displacement and cladding failure. These measurements are complemented by pre- and post-test non-destructive examinations, completed within the CABRI facility, such as gamma scanning and X-ray tomography. These examinations, performed in the IRSN facility for radiography, imaging and spectrometry (IRIS), supply information on the test pin degradation and possible fission product distribution.

1.2.3. Test device and instrumentation

The test device (see Figure 15) developed by IRSN, is a complex piece of equipment that contains the test pin and its instrumentation. The test pin is located in the test channel. The pressurized water enters the test channel through an energy absorber tube, and exits at the top of the channel tube through the pressurized water outlet. A specific spacer system ensures the correct positioning of the fuel pin and enables the fluid and cladding temperature measurements.

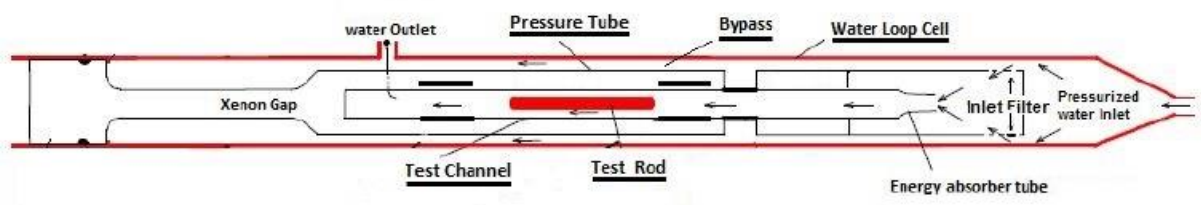


Figure 15. Schematic view of the test device

The test channel and associated instrumentation is surrounded by the pressure tube. In order to insulate the test channel from its environment and to protect its instrumentation, the tube is filled with pressurized xenon gas, 1 bar at the lower section and 2 bar in the higher section. The pressure tube is equipped with filters at the water inlet and outlet to retain the particles that could be ejected during fuel failure.

The test device is equipped with specific instrumentation, shown in Figure 16, with high accuracy, short response time and that are capable of withstanding the transient conditions. The installation of the instrumentation required specific technologies, such as microbrazed passages ensuring leak tightness between instrument cable and test device structures, high temperature connection units and electrical connectors.

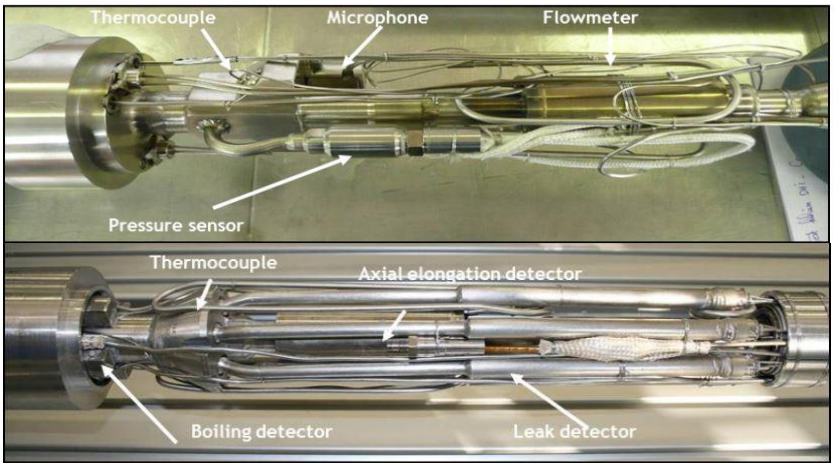


Figure 16. Instrumentation on the lower and upper part of the test device (IRSN, 2021)

The steady-state channel flow rate is measured by two turbine flowmeters while the transient flow rate is measured by two target flowmeters, positioned below and above the test rod. A pressure transducer is also located in the xenon gap to detect possible leaks while an all-or-nothing leak detector is placed in the argon gap.

In total, 30 K-type thermocouples are used for temperature measurements in the test device. These thermocouples, placed on the inner and outer ring of the spacer rings, at various locations of the test channel, provide information about the channel, cladding surface, pressurized water, channel tube outer wall and sensor temperatures. The cladding elongation is measured by a displacement transducer, which is placed above the test rod. In order to detect the onset of water boiling near the cladding surface an ultrasonic wave system, composed of one emitter and three receivers, is employed. The signal of the emitter will change with the presence of bubbles, as a result of variations of the acoustic impedance and dissipated energy in the water.

1.2.4. Reactivity insertion system

The CABRI reactor has a unique reactivity insertion system (see Figure 17) that is capable of injecting up to 4$ external reactivity. The main components of the insertion system are the 4 transient rod assemblies, composed of 24 transient rods each, the control and fast valves, allowing the depressurization of the transient rods, and the discharge tank. The transient rod assemblies are filled with pressurized helium-3 gas. The power pulse is generated by the rapid depressurization of the helium from the transient rods to the discharge tank, by opening of the valves.

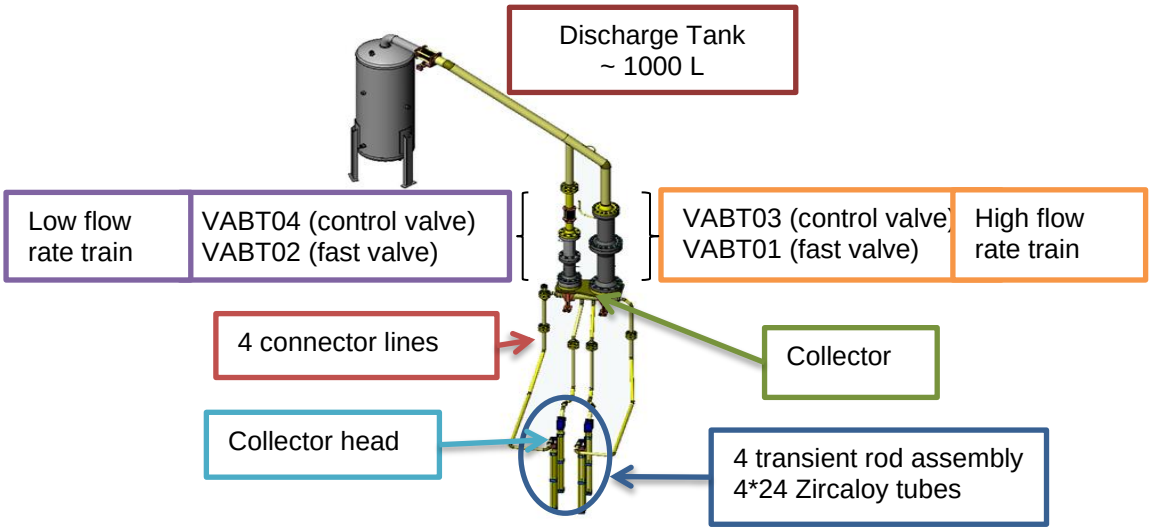


Figure 17. Reactivity insertion system

The main parameters of the power pulse, such as the peak power, the length (described by the full width at half maximum (FWHM)), and the total energy deposition depend on the operational characteristics of the reactor and are adjustable by experiment design. The most influential operational parameters are the reactor power at which the transient is initiated (0.1 MW in the case of the CABRI reactor), the initial pressure of the helium in the transient rods and the kinetics of the depressurization as defined by the valve aperture.

The initial pressure and the depressurization method of the helium (when and which valve opens) determine the maximum core power attained during the test and the duration of the transient. The total energy deposition can be finely tuned with the timing of the control rod drop considering the experimental objectives.

Two types of transients can be carried out in CABRI. In the case of a simple depressurization, or a natural transient, the helium is depressurized through either the high flow rate train (i.e. by the opening of the fast valve) or the low flow rate train (i.e. by opening the slow valve.) The transient's characteristics are defined by the initial pressure of the helium-3 in the transient

rods and the position of the control valve (fully or partially opened). The latter determines the speed of the reactivity insertion. With the same initial helium pressure, increasing the opening of the control valve leads to higher peaks and shorter transients. The simple depressurizations lead to power pulses of 20 GW with a FWHM of ~10 ms.

Figure 18 presents some examples of natural transients and it depicts the influence of the initial helium pressure on the transient's characteristics (same valve aperture).

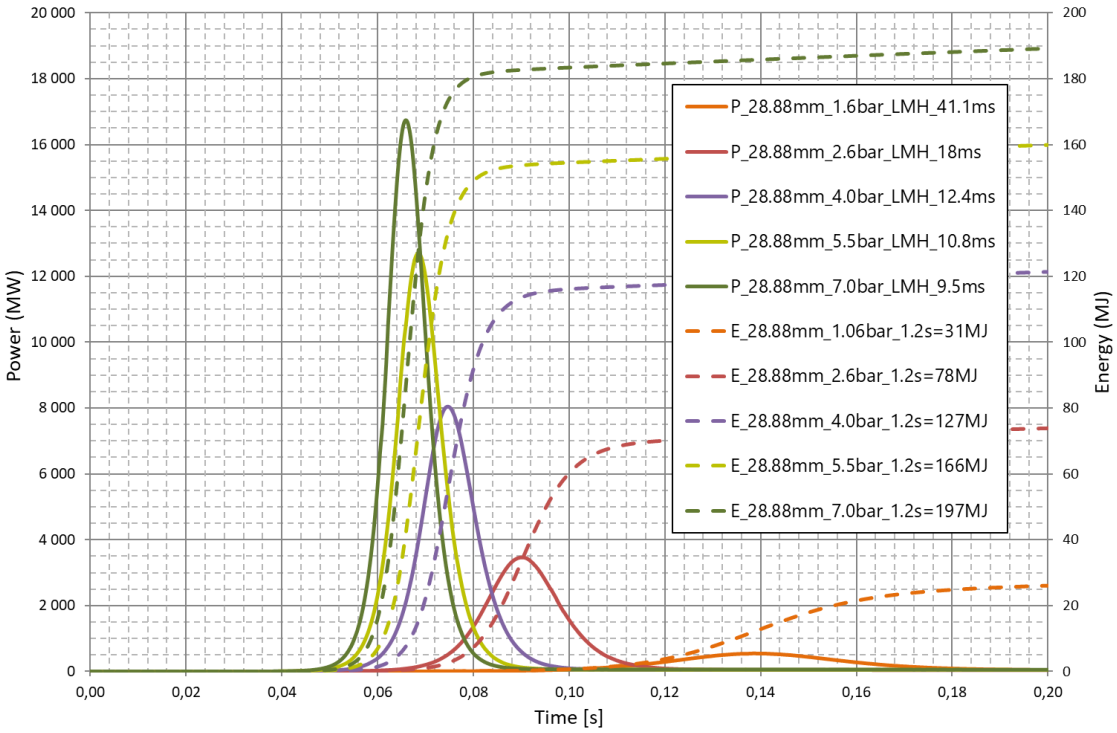


Figure 18. Natural transients with fully opened control valve and different initial helium pressure. Higher helium pressure results in higher peak power and a shorter pulse

However, based on transient calculation results, the characteristic RIA pulse in a PWR is around 25 to 65 ms, which cannot be recreated with simple depressurization. For pulses longer than 30 ms, a so-called "structured" or "double depressurization" has to be performed. In this case, the depressurization is performed in two steps. First, the reactivity insertion is initiated by the opening of the fast valve on the low flow train. The length of the power pulse is increased by the subsequent opening of the fast valve on the high flow train, leading to a secondary reactivity insertion. The characteristics of the transient are determined by the timing of the opening of the second valve, as shown in Figure 19.

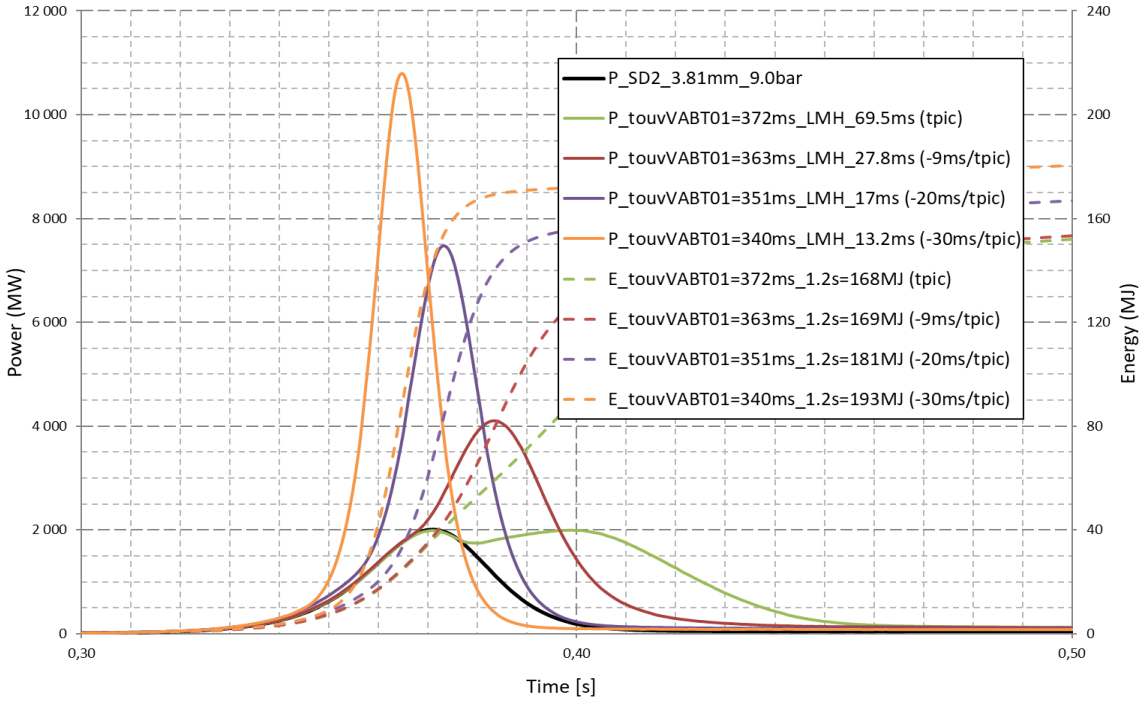


Figure 19. Structured transients with the same initial helium pressure but different opening time for the second valve. Shorter opening sequence leads to higher power peak and shorter pulse

1.2.5. Specific reactor instrumentation

IONIZATION CHAMBERS

Core power monitoring is ensured by two low-level fission chambers and two high-level boron lined detectors during the reactor startup and steady-state operation. The five experimental power chambers (G2.1, G2.2, G3.1.1, G3.1.2 and G3.4) used for transient power measurement are capable of recording signals for power ranging from 100 kW up to 25 GW. Figure 20 shows the placement of the detectors. Low power levels are recorded with the G2 chambers, which saturate around 450 MW, while the power peak is monitored by the G3 chambers. The full transient power trace is reconstructed by combining the signals of the G2.2 and G3.4 power chambers.

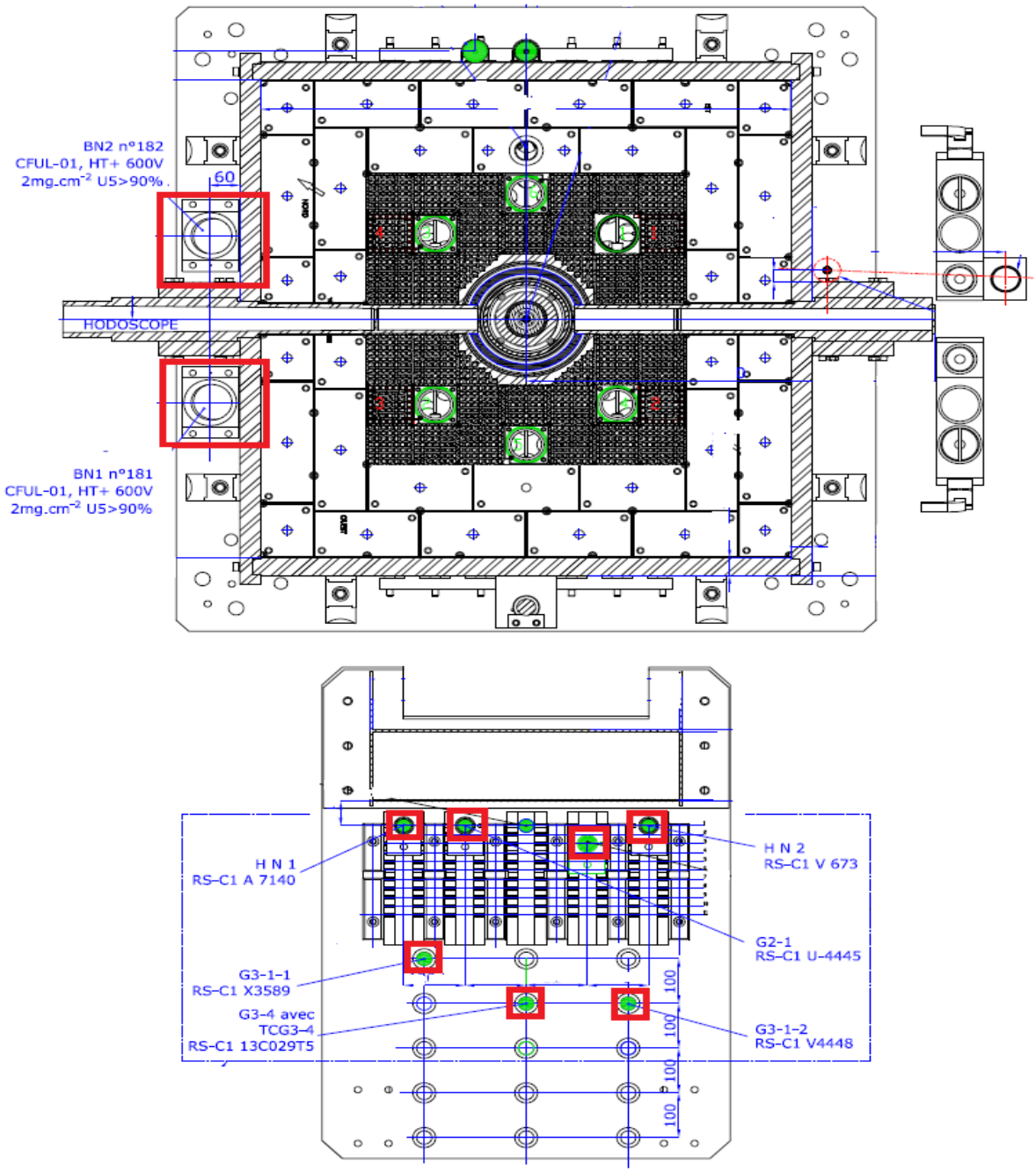


Figure 20. Placement of the various detectors in CABRI

HODOSCOPE

The hodoscope is a unique detector system that monitors the fuel movement during the transient and is able to quantify the amount of ejected fuel following a rod failure. It is composed of the irradiation channel, the collimator and the detectors (Figure 21). The hodoscope is used to determine the initial and final states of the rod, based on the fissile length and axial power distribution measurements taken before and during the transient.

The fast neutrons coming from the test pin and the core are channeled to the detectors through the collimator, which has 153 channels (3 columns of 51 channels). Behind each channel there is a ^{237}Np fission chamber (adapted for the high power range) and a proton recoil detector (suited for low-power measurements). The 51 channels allow the axial characterization of the pin.

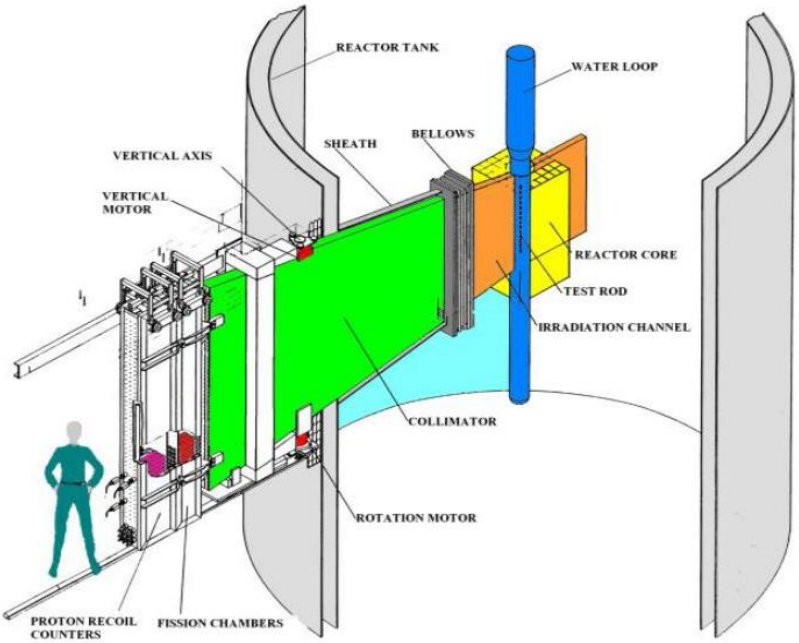


Figure 21. Hodoscope detector system (Chevalier, et al., 2018)

1.2.6. Experimental programs

Originally, CABRI was built for testing Material Testing Reactor (MTR) fuel. In the 1970s, the reactor core was modified to be equipped with a sodium loop and a unique reactivity insertion system, in order to study fuel behavior during RIA. The first experimental programs were aimed at fast reactor fuels and they were followed by experimental programs focused on high burnup PWR fuels, in line with the industry needs of the time.

Fast reactor programs (Clamens, 2018)

CABRI-1 (1978-1987)

The objective of the tests performed during the CABRI-1 program was to investigate the behavior of fast reactor fuels in two types of representative accidental situations, during a power excursion and during a loss of coolant accident. The results of the experiments gave insight in the possible damage mechanisms that can occur within the fuel during these types of accidents.

CABRI-2 (1987-1991)

The main goal of the CABRI-2 program was to produce experimental data for the validation of the calculation codes developed in parallel. Two types of irradiated fast breeder reactor fuel pins, Viggen-4 (solid pellet) and Ophelie-6 (annular pellet), were used in the 12 tests conducted within the experimental program. The experiments clearly showed the impact of the PCMI and revealed that slow transients result in higher cladding temperature than fast ones.

CABRI-FAST (1992-1997)

The third program was dedicated to annular fuel studies. The test pins were subjected to slow power transients, typical of inadvertent control rod withdrawal accidents. These experiments showed that the test pins that survived the PCMI phase failed due to the embrittlement of the cladding as a result of the high temperatures sustained during the transient.

Light water reactor programs (Clamens, 2018)

CABRI REP-Na (1992-2000)

Twelve tests were realized between 1993 and 2001 in the original sodium loop, with the objectives of identifying and quantifying the physical phenomena leading to fuel pin rupture and fuel ejection during the first phase of RIA. These tests were focused on high burnup UO_2 (>60 GWd/t) and MOX (>50 GWd/t) fuels and the results emphasized the detrimental effect of burnup on the safety margins defined before the tests.

The CABRI International Program (2002-)

The CABRI International Program (CIP) is a project run under the auspices of the Nuclear Energy Agency (NEA) and managed and funded by IRSN with support from various French and international partners. This program aims to increase the knowledge of high burnup PWR fuel (UO_2 and MOX) behavior during reactivity accidents in order to validate the current safety criteria. These tests are used for the qualification of new cladding materials as well.

The first two tests of the program were carried out in the original sodium loop in 2002. To ensure a test environment representative of a PWR, this sodium loop was replaced by a pressurized water loop during the refurbishment of the reactor. The implementation of the water loop also allows for study of the boiling phase of the transients. Following the successful qualification tests, the first test in this new environment was performed in 2018.

1.3. Energy deposition calculation during an experiment in the CABRI reactor

1.3.1. Coupling factor definition

The aim of the experiments conducted in the CABRI reactor is to study the fuel pin behavior following a reactivity insertion into the core. More precisely, the aim is to examine whether a certain type of fuel pin can withstand the energy deposition resulting from the given reactivity insertion. However, the energy deposited in the test fuel pin cannot be measured during the transient. Instead, it is calculated from the energy deposited in the core and a coupling factor.

The coupling factor (C) is defined as the ratio between the core power ($P_{core,sst}$) and the test pin power ($P_{pin,sst}$) in a steady-state operation (Eq. (1.1)). It is measured prior to each experiment by performing a thermal balance on the pressurized water loop (Jeury, et al., 2013). The coupling factor is considered valid and constant throughout the transient. This assumption implies that the ratio of the power released in the core and in the test pin is considered constant regardless the operational state of the reactor.

$$C = \frac{P_{core,sst}}{P_{pin,sst}} = \frac{P_{core,tr}}{P_{pin,tr}} \tag{1.1}$$

The coupling factor allows the calculation of the transient pin power ($P_{pin,tr}$, which is not directly measured) from the transient core power ($P_{core,tr}$, measured with the experimental

power chambers). The transient pin power in turn is used to calculate the energy deposition into the test pin during the transient.

Besides the transient energy deposition calculation, the coupling factor plays an important role during the experiment design phase as well. In the case of a CABRI experiment, the energy deposition into the test pin, among other transient characteristics, is imposed by the client. The experiment is preceded by a start-up campaign experiment, with the objective to define the main parameters for the transient rod system, such as the opening time of the valves, the initial helium pressure and timing of the control rod drop, in order to ensure that the requested energy deposition is obtained. The energy deposited in the test pin can be correlated through the coupling factor to the energy deposition in the core, which in turn depends on the initial conditions of the core. Thus, having an estimation on the coupling factor prior to the experiment plays an important role in defining the suitable input parameters in order to meet the target parameters.

1.3.2. Steady-state and transient core power measurement

The primary method for measuring the core power in steady state is by performing a thermal balance on the core water loop, while also considering the different thermal losses that occur in the system:

$$P_{core,sst} = P_{TB} + P_{TL} + P_L + P_\gamma + P_n \tag{1.2}$$

Where $P_{core,sst}$ is the total core power in steady state, P_{TB} is the core power given by the thermal balance, P_{TL} is the amount of thermal power lost through the core water loop wall, P_L describes the thermal loss to the surrounding medium, and P_γ and P_n refer to the thermal losses due to gamma and neutron leakage.

The thermal balance is measured based on the flow rate and temperature measurements from the hot and cold leg of the core-water circuit. In the current design, the top of the core is not fully isolated from the reactor pool. As a result, there is a non-negligible amount of mixing between the warmer primary circuit water and the cold water (20°C) from the reactor pool. Thus, considering only the temperature difference between the hot and cold leg during the thermal balance would lead to an underestimation of the core power. The mixing is taken into account through a mixing factor, P_M, determined experimentally. Accordingly, the core power during a thermal balance is defined as the sum of the raw power ($P_{TB,brut}$) and the amount of thermal loss due to the mixing (P_M) :

$$P_{TB} = P_{TB,brut} + P_M = \rho \cdot c_p \cdot Q \cdot (T_{out} - T_{in}) + P_M \tag{1.3}$$

Where ρ is the water density, c_p is the specific heat capacity, Q is the volumetric flow rate and T_{in} , T_{out} are the inlet and outlet water temperatures.

By measuring the heat exchange rate between the reactor pool and the air in the reactor hall, the amount of heat lost through the reactor pool to the medium (P_L) during a thermal balance was estimated to be less than 0.01% and is considered negligible. The heat dissipated from the cooling circuit to the reactor pool through the circuit walls (P_{TL}) amounts for less than 0.3% of the total core power. The amount of energy dissipated by the photons and neutrons that leak out of the core was estimated to be less than 0.5% of the total core power (0.3% for gamma and 0.15% in the case of neutron heating). Thus, the different thermal losses amount to 0.8% of the core power measured by performing a thermal balance on the core water loop.

The thermal balance measurement is not available during a transient. Instead, the experimental chambers are used to measure the core power throughout the transient.

1.3.3. Steady-state and transient pin power measurement

The pin power, or in other words the power released by the test pin, is measured via a thermal balance on the pressurized water loop ($P_{channel}$) in steady-state:

$$P_{channel} = \rho \cdot c_p \cdot Q_{loop} \cdot (T_{out,loop} - T_{in,loop}) \quad (1.4)$$

However, the power measured by thermal balance on the pressurized water loop includes the thermal power due to the gamma heating, (P_γ) originating from the core, whereas it does not take into account the thermal power dissipated on the structural elements of the pressurized loop (P_{losses}). The latter was estimated to be 0.25% of the total power, and it is thus not considered. Accordingly, the steady-state pin power is defined as follows:

$$P_{pin,sst} = P_{channel} - P_\gamma \quad (1.5)$$

The amount of power due to the gamma heating from particles originating from the core and dissipated in the pressurized water loop was estimated as:

$$P_\gamma = C_\gamma \cdot P_{core} \quad (1.6)$$

with C_γ being equal to 0.09 kW/MW based on previous measurements.

1.3.4. Energy deposition calculation during a transient

The core power profile during a RIA test is reconstructed from the signals of the G2.2 (at low power) and the G3.4 (at high power) ionization chambers. Integrating the reconstructed power traces gives the energy deposition into the core as shown in the following:

$$E_{core,tr}(t) = \int_0^t P_{core,tr}(x)dx = P0_{G2}\left[\int_0^{ts} \frac{P_{G2}(x)}{P0_{G2}}\,dx + \int_{ts}^t \frac{P_{G3}(x)}{P0_{G2}}\,dx\right] \quad (1.7)$$

In order to compensate the lower sensitivity of the G3.4 chamber and to take advantage of the better sensitivity of the G2.2 chamber at low power levels, the core power, and thus the energy deposition, is normalized to the steady-state power measured by the G2.2 chamber ($P0_{G2}$).

Finally, the transient energy deposition in the pin is calculated from the transient core power and the coupling factor as:

$$E_{pin,tr}(t) = \int_0^t P_{pin,tr}(x)dx = \frac{1}{C}\int_0^t P_{core,tr}(x)\,dx \quad (1.8)$$

2. METHODS AND OBJECTIVES

There are two main objectives of the PhD work: modelling and simulating a reactivity insertion transient and the calculation of the energy deposition into a test pin during the transient. This chapter gives an overview on the calculation methodologies used during this work. The first section presents of the theoretical elements needed to understand the methodologies and analysis presented later on. It is divided into two topics: reactor kinetics, describing the time-dependent neutron population evolution including the aspects pertinent to a reactivity insertion, and nuclear heating, which covers the fission energy generation and deposition. The second section is focused on the presentation of the different calculation codes used during this work, along with an in-depth presentation of the newly developed kinetic module of the TRIPOLI-4® code. It also includes a state of the art on modelling of non-stationary situations as well as on the modelling and the energy deposition calculation specific to the CABRI transients. Finally, the third section of this chapter is devoted to the presentation of the energy deposition calculation scheme developed during this work.

2.1. Theoretical background

2.1.1. Generalities

One of the key parameters in reactor physics is the neutron flux, which gives the total path covered by all neutrons per unit time in a given volume. It is calculated using the neutron density, as shown below:

$$\phi = n \cdot v \tag{2.1}$$

Where ϕ : is the neutron flux [neutrons · $cm^{-2}s^{-1}$]
n : is the neutron density [neutrons · cm^{-3}]
v : is the neutron velocity [$cm \cdot s^{-1}$]

The probability of interaction between a neutron and a nucleus in its path is described by the cross-section, which actually represents an effective target area for the interaction. Whether it refers to the target area for a single nucleus or all nuclei in a volume, the cross-section is denoted microscopic or macroscopic. The latter incorporates the impact of the density of the target nuclei on the interaction probability.

The rate of interaction in a given volume, otherwise known as the reaction rate, can be calculated from the neutron flux and the cross-section as follows:

$$RR = \phi \cdot \Sigma = \phi \cdot \sigma \cdot N \quad (2.2)$$

Where RR : is the reaction rate [interaction $s^{-1}cm^{-3}$]

Σ : is the total macroscopic cross-section [cm^{-1}]

σ : is the total microscopic cross-section [barn = 10^{-24} cm^2]

N : is the atomic density [cm^{-3}]

A specific cross-section, and accordingly reaction rate, can be defined for each interaction in the reactor. The total cross-section is given by the sum of the specific cross-sections. The most important neutron-induced interaction are the following (Reuss, 2008):

- *Elastic scattering* (n,n): the incident neutron scatters off the nucleus without absorption; the kinetic energy of the system is conserved, but its direction is changed
- *Resonance elastic scattering* (n,n): emission of a neutron from the compound nucleus formed after the absorption of the incident neutron; the initial state of the target nucleus does not change
- *Resonant inelastic scattering* (n,n'): emission of a neutron from the compound nucleus formed after the absorption of the incident neutron; the target nucleus is in excited state following the ejection of the neutron
- *(n, 2n) reaction*: resulting in the ejection of two neutrons
- *Capture*: The neutron is absorbed by the nucleus, creating a compound nucleus. The capture can be followed by the emission of light charged particles (eg. (n,p); (n, α) reactions) or photons (n,γ).
- *Fission* (n, f): following the absorption of the incident neutron the nucleus splits in two, or sometimes three, fission fragments while ν (0< ν <7) neutrons are emitted

The cross-section, among other nuclear data such as neutron angular distribution, decay data, fission product yield and fission spectra are stored in evaluated nuclear data files for example the ENDF/B-VIII (Brown, et al., 2018) or the JEFF3.1.1 (Santamarina, et al., 2009) nuclear data libraries. An example of cross-sections is given in Figure 22. Three cross-section regions can be distinguished: 1/v region at low energies (<0.1 eV), where the cross-section decreases with increasing incident energies; the resonance region (~0.1 eV to 100 keV), where each resonance represents an excitation level of the compound nucleus formed after the absorption of a neutron, and finally the fast neutron region (>100 keV), where the cross-section decreases significantly.

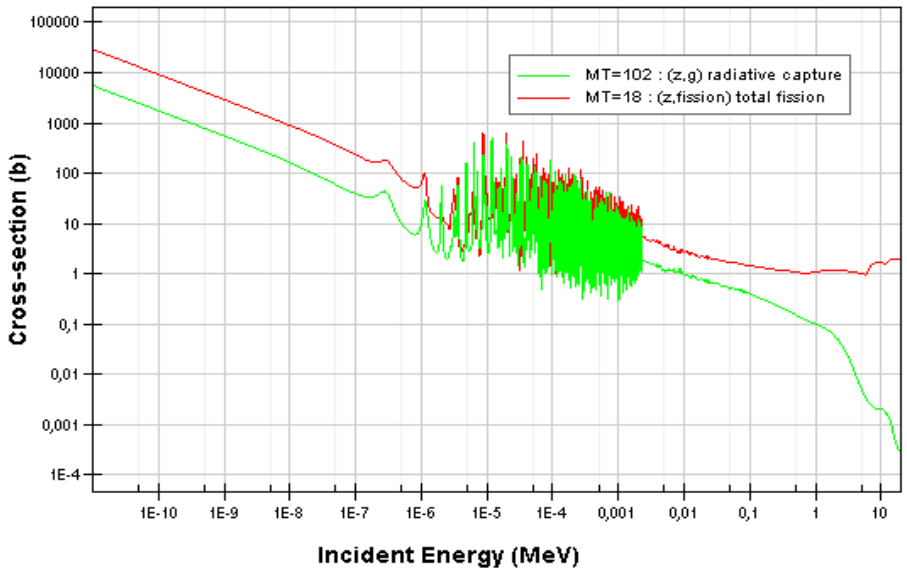


Figure 22. Radiative capture and fission cross-section for the ^{235}U isotope

Amongst the different interaction types in a reactor core, the fission is of particular interest. The reactor operation, might it be commercial or research, is based on stable, self-sustained fission chains, where there are just enough free neutrons generated from a fission to induce further fission events. Based on the time of their appearance, the neutrons created after fission are referred to as prompt or delayed. Prompt neutrons are emitted immediately after fission, in about 10^{-15} seconds. The delayed neutrons are emitted after the decay of given fission products, named precursors. The decay takes place within a timescale ranging from fraction of seconds to hours following the fission, defined by the decay constant λ of the precursors, which describes the probability of the nucleus to decay per unit time and which differs from nuclei to nuclei (Ott & Neuhold, 1985). Since there are too many precursors (~150) for them to be treated individually, they are grouped, based on their mean lifetime, in either 6 or 8 precursor families, denoted with i. Each family is described by a delayed fraction $\beta_i(t)$ and decay constant λ_i.

The energy of the delayed neutrons is lower than the energy of the prompt neutrons, meaning that they are more efficient in inducing fissions (they need less time for slowing down and there is less chance for being absorbed or leaking out of the system) (Reuss, 2008). In order to account for this, the delayed fraction is weighted by an importance function $\phi'(\vec{r}, E)$, which represents the probability that a neutron introduced at a position *r* and energy *E* will result in a fission. The weighted parameter is the effective delayed neutron fraction, denoted β_{eff}.

In reactor physics a self-sustained fission chain is described through the effective multiplication factor (k_{eff}), which is defined as the ratio between the neutron production reaction rate and the sum of the absorption reaction rate and neutron leakage. The multiplication factor reflects how the neutron population varies from one generation to another and it can be used to

describe the reactor state. In reactor physics another term, the reactivity (ρ), is introduced to describe the departure of the reactor from an equilibrium state. It is calculated from the multiplication factor and is usually expressed in *per cent mille* (pcm = 10^{-5}):

$$\rho = \frac{k_{eff} - 1}{k_{eff}} \tag{2.3}$$

Based on the reactivity and the effective multiplication factor, the reactor states can be classified as follows:

- → *Subcritical state* when the multiplication factor is lower than 1, corresponding to a reactivity lower than 0. In this case, without external intervention, the neutron population decreases over time.
- → *Critical state* when the effective multiplication factor is equal to 1, and the reactivity is equal to 0. In this case the neutron production and loss is in equilibrium and the reactor is operating at steady power (state).
- → *Supercritical state* in the case of an effective multiplication factor superior to 1, corresponding to a reactivity higher than 0. In this case the neutron population is exponentially increasing in time without external intervention. If the reactivity is higher than the β_{eff}, it is referred to as *prompt-supercritical state*.

Another important parameter closely related to the reactivity is the reactivity feedbacks. Reactivity feedbacks refer to the inherent response of the reactor system to a reactivity change. Reactors are designed in a way that ensures that the reactivity feedback is negative, meaning that a power increase resulting from an accidental reactivity insertion can be mitigated without external intervention.

A reactivity insertion is usually followed by a power and temperature increase. The latter changes the properties of the different materials in the core that can ultimately result in a negative reactivity insertion. For example, the moderator density decreases with increasing temperatures. Sufficiently high temperatures can even lead to its vaporization. Both of these effects decrease the neutron moderation in the core, ultimately leading to a lower reactivity. It is known as the moderator feedback. However, since the heat transfer between the fuel and moderator is not instantaneous, this feedback is only a secondary effect for power stabilization.

The main feedback is the Doppler feedback. This effect is linked to the Doppler broadening of resonance capture cross-sections of the isotopes following a temperature increase. This results in an increased neutron capture in fertile isotopes and ultimately in a decrease of neutrons available for fission. This effect is instantaneous, and in the case of reactivity insertion accidents, it can terminate the power surge.

The time-dependent behavior of the neutron population following a reactivity insertion is detailed in the following sections.

2.1.2. Neutron transport equation

The evolution of the neutron population as a function of time and space is described with the Boltzmann equation (transport equation). Two forms of the transport equation are presented in the following, the transport equation describing a time-dependent (kinetic calculation) and the transport equation describing a steady-state operation (static calculation), usually corresponding to the critical core configuration.

2.1.2.1. Time-dependent transport calculation

The goal of a kinetic calculation is to determine the behavior of the neutron flux $\psi(\vec{r}, E, \vec{\Omega}, t)$ in a time-dependent system starting from a given initial condition. This is also referred to as the angular flux which represents the number of neutrons of velocity v perpendicularly crossing a unit surface in $\vec{r}$ perpendicular to $\vec{\Omega}$, per unit energy E, per unit of solid angle in the $\vec{\Omega}$ direction, at a given instant t. Integrating the angular flux over the angles results in the scalar flux $\phi(\vec{r}, E, t)$ (CEA, 2015).

Such system is described by the time-dependent Boltzmann equation (2.4) coupled with the precursor concentration equation (2.5). The following is the integro-differential form of the neutron transport, expressed as a balance equation between the production and removal rate of neutrons:

$$\begin{aligned}\frac{\partial n(\vec{r}, E, \vec{\Omega}, t)}{\partial t} \;=\; & -\vec{\Omega} \cdot \vec{\nabla}\psi(\vec{r}, E, \vec{\Omega}, t) - \sum_k N_k(\vec{r}, t)\, \sigma_k(E)\psi(\vec{r}, E, \vec{\Omega}, t) \\ & + \sum_k N_k(\vec{r}, t) \int_0^\infty dE' \int_{4\pi} d\vec{\Omega'}\; \sigma_{s,k}(E' \to E, \vec{\Omega'} \to \vec{\Omega})\psi(\vec{r}, E, \vec{\Omega'}, t) \\ & + \frac{1}{4\pi}\Big(\sum_k N_k(\vec{r}, t) \int_0^\infty dE'\, \upsilon_{p,k}(E')\, \sigma_{f,k}(E')\chi_{p,k}(E' \to E)\phi(\vec{r}, E', t) + \sum_k \sum_i \lambda_i^k C_i^k(\vec{r}, t)\chi_{d,i}^k(E)\Big) \\ & + S_{ext}(\vec{r}, E, \vec{\Omega})\end{aligned} \tag{2.4}$$

The first term describes the rate of change of neutron density $n(\vec{r}, E, \vec{\Omega}, t)$, i.e. the number of neutrons per unit volume in $\vec{r}$, per unit energy in E, per unit of solid angle in the $\vec{\Omega}$ direction, at a given instant t. It can be also be expressed with the angular flux $\psi(\vec{r}, E, \vec{\Omega}, t)$ as follows:

$$\frac{\partial n(\vec{r}, E, \vec{\Omega}, t)}{\partial t} = \frac{1}{v}\frac{\partial \psi(\vec{r}, E, \vec{\Omega}, t)}{\partial t} \tag{2.5}$$

The first term on the right hand side describes the neutron leakage from the studied volume and the second term represents the neutron disappearance resulting from the absorption and scattering of the neutrons (i.e. neutrons that are removed from the given phase space due to the change in their direction and energy following a scattering interaction). The notations are as follows: $\overrightarrow{\Omega}$ is the phase defining the neutron's direction, $N_k(\vec{r})$ is the concentration of nuclide *k* and $\sigma_k(E)$ refers to the total microscopic cross-section of the nuclide.

Neutrons can also arrive to energy E and direction $\overrightarrow{\Omega}$ after scattering at their previous energy E' and direction $\overrightarrow{\Omega'}$. This is described by the third term, where $\sigma_{s,k}$ is the microscopic scattering cross-section and it comprises the elastic, inelastic and (n, 2n) scattering cross-sections.

The fourth term describes the neutron production due fission. This includes both the prompt and delayed neutron production. The notations are: $\upsilon_{t,k}(E')$ is the average neutron number (prompt and delayed) emitted after a fission, $\sigma_{f,k}(E')$ is the microscopic fission cross-section and $\chi_{p,k}(E' \rightarrow E)$ is the energy spectrum of the prompt neutrons. Finally, the last term describes the neutron production from external sources (for example the neutrons resulting from the spontaneous fission of heavy nucleus).

The precursor population evolution can be expressed as follows (CEA, 2015):

$$\frac{\partial \mathrm{C}_i^k(\vec{r},\mathrm{t})}{\partial \mathrm{t}} = -\lambda_i^k \mathrm{C}_i^k(\vec{r},\mathrm{t}) + N_k(\vec{r}\,)\beta_i^k \int_0^\infty dE'\, \upsilon_{t,k}(E')\, \sigma_{f,k}(E')\phi(\vec{r},E',t) \tag{2.6}$$

Where C_i^k is the precursor concentration of group i, λ_i^k is the mean decay constant of the nuclide *k*, and β_i^k is the delayed neutron fraction for the precursor group i. The first term on the right hand side represents the precursor loss, the precursor decay, while the second term gives the number of precursors created through fission.

2.1.2.2. Steady-state transport calculation

In a case of a steady-state transport the time dependence can be omitted. A steady state also implies a constant neutron population, meaning that the neutron loss is equal to the neutron gain. Furthermore, in steady-state calculation there is no difference made between the delayed and prompt neutrons and thus the emission spectrum is approximated with the prompt neutron emission. Then the time-dependent neutron transport equation can be re-written as:

$$\overrightarrow{\Omega}\cdot\vec{\nabla}\psi(\vec{r},E,\vec{\Omega}) + \sum_k N_k(\vec{r})\,\sigma_k(E)\psi(\vec{r},E,\vec{\Omega}) =$$

$$= \sum_k N_k(\vec{r}) \int_0^\infty dE' \int_{4\pi} d\overrightarrow{\Omega'}\ \sigma_{s,k}(E'\to E,\overrightarrow{\Omega'}\to\vec{\Omega})\psi(\vec{r},E,\overrightarrow{\Omega'}) + \qquad (2.7)$$

$$+\frac{1}{4\pi}\sum_k N_k(\vec{r}) \int_0^\infty dE'\,\upsilon_{t,k}(E')\,\sigma_{f,k}(E')\chi_{p,k}(E'\to E)\phi(\vec{r},E') + S_{ext}(\vec{r},E,\vec{\Omega})$$

The transport equation is solved numerically based on either deterministic or stochastic methods. Deterministic methods are based on solving the transport equation by discretizing the phase space (energy, direction and space). The discretization allows relatively fast calculations at the cost of introducing approximation errors. On the other hand, the stochastic (or Monte Carlo) methods simulate a large number of neutron histories based on which the macroscopic quantities of interest (neutron flux, effective multiplication factor, reaction rates etc..) can be estimated without introducing approximations. The down-side of the statistical methods is the significant computation time needed to obtain acceptable statistical errors (CEA, 2015).

2.1.2.3. Point kinetics approximation

Point kinetics is a simplified formalism describing the kinetic behavior of a system. It is based on the approximation that the neutron flux $(\psi(\vec{r}, E, \vec{\Omega}, t))$ can be factorized in two functions, an amplitude function $(n(t))$ and a shape function $(\varphi(\vec{r}, E, \vec{\Omega}))$, where only the amplitude function is time-dependent while the spatial distribution of the flux is considered constant, as written in equation (2.8) (Reuss, 2008). This way the reactor can be reduced to a point, hence the name of this approximation.

$$\psi(\vec{r}, E, \vec{\Omega}, t) = n(t)\cdot\varphi(\vec{r}, E, \vec{\Omega}) \qquad (2.8)$$

The evolution of the neutron population, described by the amplitude function, is defined by the effective multiplication factor (or reactivity), the mean generation time (Λ) and the delayed neutron parameters, otherwise referred to as the kinetic parameters. The mean generation time is the average time elapsed between the emission of a prompt neutron and the fission caused by it. It is closely related to the neutron lifetime (l), which is the time elapsed between the birth and the disappearance of a neutron. In a critical state the generation time is equal to the lifetime ($l = \Lambda\cdot k_{eff}$).

The point kinetics equations can be obtained by considering a balance equation system of the neutron ($n(t)$) and the precursor ($C(t)$) densities. Formally, it is expressed as:

$$\frac{\partial n(t)}{\partial t} = \frac{\rho(t) - \beta(t)}{\Lambda(t)} n(t) + \sum_i \lambda_i C_i \tag{2.9}$$

$$\frac{\partial C_i(t)}{\partial t} = \frac{\beta_i(t)}{\Lambda(t)} n(t) - \lambda_i C_i \tag{2.10}$$

In the neutron balance equation, the first term represents the prompt neutron production in the given generation while the second term describes the delayed neutron production following the decay of precursors. Similarly, the precursor population balance is given by the number of precursors created during the given generation and the disappearance of precursors due to their decay. This equation system is solved for each i precursor family apart.

The general solution to the point kinetics differential equation system, can be written as (CEA, 2015):

$$n_j(t) = \sum_{j=0}^{6} A_j \exp(\omega_j t) \tag{2.11}$$

$$C_i(t) = \sum_{j=0}^{6} B_{ij} \exp(\omega_j t) \tag{2.12}$$

The time constant ω has to satisfy the following condition, otherwise known as the inhour equation:

$$\rho = \omega \left[\Lambda + \sum_{j=0}^{6} \frac{\beta_i}{\lambda_i + \omega} \right] \tag{2.13}$$

The importance of the inhour equation lies in the fact that it links the reactivity (insertion) to the time constant, which in turn will determine the speed of the exponential power variation. The inverse of this time constant is called the reactor period, *T*.

In the case of high reactivity insertions, such as the prompt supercritical transients, the prompt neutrons alone are able to offset the neutron loss. This also means that population increase is driven by the prompt neutrons, meaning that the time constant is in the order of magnitude of the prompt neutron generation lifetime (~20 μs). The corresponding time constant is called the prompt inverse period and it can be approximated as:

$$\omega = \frac{\rho - \beta}{\Lambda} \tag{2.14}$$

Whereas for a reactivity insertion lower than the effective delayed neutron fraction (a supercritical transient) the delayed neutrons are still needed to make up for the neutron loss.

Then, due to the long mean precursor lifetime, the time constant is in the order of tenths of seconds, which makes it feasible to control the reactor. Then the time constant can be approximated as:

$$\omega \cong \frac{\rho}{\tau} = \frac{\rho}{\Lambda + \sum_i \frac{\beta_i}{\lambda_i}} \tag{2.15}$$

2.1.2.4. Quasi-static method

The point kinetics method assumes that the neutron flux distribution is time-independent, which can be reasonably used for steady-state operations, but it is not applicable for non-stationary situations. The time dependence of the flux, important in a transient simulation, can be accounted for by using the quasi-static method. Similarly to point kinetics, this method also relies on the factorization of the flux into an amplitude ($n(t)$) and a shape ($\varphi(\vec{r}, E, \vec{\Omega}, t)$) function, where the amplitude is time-dependent and can be obtained via point kinetics (Dulla, et al., 2008). The needed kinetics parameters in turn are defined by the shape function. Most importantly, in the quasi-static method the shape function is also time dependent, but in the original definition it is set to the initial flux distribution, follows:

$$\psi(\vec{r}, E, \vec{\Omega}, t) = n(t) \cdot \varphi(\vec{r}, E, \vec{\Omega}, t) \tag{2.16}$$

2.1.3. Fission energy and nuclear heating

Following a fission event the nucleus splits into two, rarely three, smaller nuclei, called fission fragments. Fission fragments are emitted in excited states and de-excite by emitting neutrons and gamma photons, called prompt neutrons and gammas. Once de-excited, the fission fragments are called fission products. They can contain an excess of neutrons and are generally β-emitters. The disintegration of these fission products leads to the emission of so-called delayed particles: neutrons, photons, electrons etc.

The fission event is accompanied by ~200 MeV energy release. The energy generated during fission appears as the kinetic energy of the particles created during the fission and the subsequent decay events. This energy is then conveyed to the surrounding medium through specific interactions, characteristic to each particle type, which also defines the spatial repartition of the carried energy. These interactions represent the fundamental mechanism for energy deposition in the reactor, i.e. *nuclear heating*.

Fission is a highly exothermic reaction, with a reaction heat of about 200 MeV. Table 2 summarizes the distribution of the energy generated during fission between the different particles, including the characteristic range of motion of these particles. The majority of the fission energy (~87%) is transmitted to the fission fragments, which interact strongly with the surrounding atoms, causing their ionization. The created electron will then reunite with the positive ion, resulting in energy deposition in the form of heat. The distance travelled by the latter is in the range of microns, and as such, the fission products deposit their energy in the fuel pin. Similarly, the beta particles, i.e. electrons or positrons, transfer their kinetic energy, representing ~3% of the recoverable energy, primarily to the fuel pin through ionization with a motion range of millimeters.

Energy	U-235 [MeV]	Pu-239 [MeV]	Pu-241 [MeV]	Range
Fission products (FP)	169.12 ± 0.49	175.78 ± 0.40	175.36 ± 0.68	~μm
Prompt neutrons	4.79 ± 0.07	6.06 ± 0.10	5.99 ± 0.13	1-10 cm
Prompt γ	6.97 ± 0.50	6.75 ± 0.47	7.64 ± 0.69	10 cm -1 m
Delayed neutrons	0.007 ± 0.002	0.003 ± 44e-6	0.005 ± 0.001	1-10 cm
Delayed γ	6.33 ± 0.05	5.17 ± 0.06	6.40 ± 0.09	10 cm -1 m
Delayed β	6.50 ± 0.05	5.13 ± 0.06	6.58 ± 0.09	~mm
Neutrinos and antineutrinos	8.75 ± 0.07	7.14 ± 0.09	8.85 ± 0.12	∞
Total energy	202.47 ± 0.13	206.21 ± 1.18	210.83 ± 0.25	μm - cm
Recoverable energy	**193.72 ± 0.15**	**199.07 ± 1.09**	**201.98 ± 0.28**	**μm - cm**

Table 2. Decomposition of the energy released during fission given in JEFF3.1.1. (Santamarina, et al., 2009)

On the other hand, both the neutrons and the gamma rays can travel outside of the test pin and deposit their energy, ~3% and ~7% respectively, along the way. These neutral particles do not ionize directly the surrounding medium, instead they create charged particles along their path, which in turn convey their kinetic energy to the medium. The kinetic energy of the antineutrinos, representing about 5% of the total energy, is non-recoverable since they do not interact with the reactor materials.

Nuclear heating is defined as neutron and gamma (or photon) heating, indicating the neutral particle that led to the production of charged particle, responsible for the temperature increase.

There can be a further distinction made between the contribution of the prompt and the delayed particles to the nuclear heating.

The prompt neutron heating is due to the fission fragments resulting from neutron interactions and the recoil energy of the nucleus following neutron diffusion (Lemaire, 2015). The delayed neutron heating consists of the energy deposition due to the delayed neutrons emitted following a prior neutron interaction. The prompt gamma source comprises the photons emitted right after a fission reaction, a radiative capture or an inelastic neutron scattering. The gammas emitted after the decay of the fission products and activation products represent the delayed gamma source. Depending the composition of the studied region, one or the other type of nuclear heating predominates. Neutron heating is more prominent in the fissile materials (mainly coming from fission reactions) and in the moderator, and gamma heating is dominant in the non-fissile materials.

2.2. Modelling a reactivity insertion accident

2.2.1. State of the art on transient simulation with Monte Carlo codes

Multiphysics calculations have been an active research area in reactor simulations for some time (Sanchez-Espinoza, et al., 2021). The objective of this research is to obtain high fidelity simulation tools by coupling neutronics, thermal-hydraulics and/or thermo-mechanical codes, which can be used to model multiphysics and multiscale reactor phenomena. The final goal is to develop and validate such simulation tools which can be used for both steady-state and transient simulation and which can be employed for full-scale reactor simulations. At the beginning only the deterministic neutronics codes were considered for multiphysics coupling, however in recent years the interest in using Monte Carlo codes has raised due to the significant increase in computing power.

The interest in the multiphysics simulation is mirrored in the activities of international expert groups and the increasing number of research projects funded on the subject. These include projects like HPMC (Demaziere, et al., 2020), NURESAFE (Demaziere, et al., 2020)and McSAFE (Sanchez-Espinoza, et al., 2021). The HPMC project aimed at developing multi-physics codes for depletion calculations with feedbacks and at developing and implementing time-dependent Monte Carlo methods.

In the framework of the McSAFE project the main goal was to transition from proof of principle simulations to realistic industry-like simulations. The developments covered the multiphysics coupling, full-core depletion calculations and dynamic Monte Carlo simulations for transient analysis. The neutronics codes included were TRIPOLI (Brun, et al., 2015), SERPENT (Leppanen, et al., 2015), MONK (Richards, et al., 2019) and MNCP (Goorley, 2014). On the thermo-

hydraulics side the subchannel code SUBCHANFLOW (SCF) (Imke & Sanchez, 2012) is favored to CFD codes due to the high computational and memory need of the latter. Finally, for the thermo-mechanics solver the TRANSURANUS (Schubert, et al., 2011) code was chosen.

The first kinetic simulations, albeit on fuel assembly scale, were realized by Sjenitzer and Hoogenboom (2013). These simulations included specific kinetic methods such as tracking separately the neutron and precursor population, forced precursor decay, branchless collision, and combing. Sjenitzer (2015) performed the first coupled time-dependent Monte Carlo simulation between TRIPOLI-4® and SCF for a mini-core of 3x3 assemblies for both steady-state and transient (reactivity insertion) conditions. In parallel, kinetic modules were included in SERPENT2 (Leppanen, 2013) and OpenMC (Mylonakis, et al., 2017).

These methods, especially the variance reduction techniques, were further improved in the framework of a PhD work conducted at CEA aimed at developing a non-stationary coupling scheme between TRIPOLI-4® and SCF (Faucher, 2019). Kinetic simulation were performed on realistic system such as the SPERT III-E core in different core configurations (steady-state, reactivity insertion of approximately 0.5$, rod-drop) and on a TMI-1 mini-core benchmark for a reactivity insertion of ~0.5$. The coupling scheme proved to be operational and in good agreement with results obtained with the Serpent2 and SCF coupling (Faucher, et al., 2021).

2.2.2. State of the art on the simulation of the CABRI transient

The main tool used for CABRI experiment prediction and safety studies is the DULCINEE code. DULCINEE is a multiphysics code based on the coupling of a 1D thermal-hydraulic module with a point kinetics module to calculate the core power (Ritter, et al., 2012). It allows for steady-state and transient calculations as well. To improve the prediction of the physical characteristics of the transient, such as the power peak, transient length and energy deposition, the SPARTE code was developed in the framework of a PhD thesis (Clamens, 2018). SPARTE uses DULCINEE's main program to simulate CABRI power transients. These improvements are based on the implementation of surrogate models for physical parameters such as the helium density, the Doppler coefficient and axial neutron flux distribution.

Consecutively, a new modelling tool called PALANTIR has also been developed (Labit, 2020). It is based on CATHARE (Geffraye, et al., 2011), which is a reference code developed for transient analysis related to system thermal-hydraulics studies in PWR and sodium-cooled fast reactors. PALANTIR relies on the coupling of a point-kinetics model (taking into account 3D reactivity feedback effects for neutronics), a multi-1D model for core thermal-hydraulics, a model of the helium depressurization device and a fuel behavior model taking into account the gap closure in fuel rods during the transient. It simulates the power and thermal-hydraulics characteristics

(fuel and moderator temperature) of the driver core and reactivity evolution during the transient.

Currently there is a new calculation tool being developed with the goal to become a reference tool for multiphysics coupling in the CABRI reactor. It is based on the coupling of a neutronics deterministic code, APOLLO3® (Schneider, et al., 2016), with a thermal-hydraulic code yet to be defined (Coissieux, et al., 2022).

The aforementioned models rely on point kinetics for the neutronics calculations. The reference, stochastic, code used for neutronics calculation in CABRI is the Monte Carlo code TRIPOLI-4®. With the considerable efforts and progress made in the transient and multiphysics modelling with stochastic codes in general and TRIPOLI-4®, (Sjenitzer, 2013) (Faucher, 2019), it will be possible to also consider a calculation scheme based on the coupling of 3D kinetics codes with thermal-hydraulics to simulate the CABRI transients. This modelling implementation needs to be progressive, from simplified models to the use of more accurate models for a best-estimate simulation, in order to get a comprehensive approach of the pulse phenomenology.

This PhD work represents the first stage of this process. It is focused on implementing the kinetic module of the TRIPOLI-4® code in order to simulate the reactivity transients in CABRI. Using TRIPOLI-4® also has the added benefit of explicitly modelling the test pin and pressurized water loop (not present in DULCINEE, SPARTE nor PALANTIR), which makes it possible to evaluate the dynamic energy deposition into the test pin and the dynamic coupling factor. The TRIPOLI-4® code is detailed in the following section, with emphasis on the newly developed kinetic module and its implementation.

2.2.3. Steady-state neutron transport

Monte Carlo simulations are known as exact methods, as they solve the neutron transport equation for any given geometry without introducing approximations. The physical quantities of interest are estimated by simulating a large number of neutron histories, where the neutrons are followed individually and their characteristics are sampled based on the physical laws. Then the error of the computed results is only statistical (Sjenitzer, 2013) and it follows the $1/\sqrt{N}$ law, *N* being the number of neutron histories simulated. This implies that the accuracy of the results can be adjusted with the number of simulated histories. However, an acceptable statistical error requires a significant number of histories, which comes at a high computational cost.

To improve the convergence of the calculations without increasing the simulation time, specific variance-reduction and population control methods are applied. The neutrons are provided with a statistical weight, which is updated at every interaction. As the name suggests, these methods lower the variance of the scores, resulting in better accuracy, and ensure that the

neutron population does not disappear or to grow out of bounds in non-stationary cases (CEA, 2015).

The particle history refers to the chain of events between the appearance and disappearance (through leakage or capture) of a particle. The general algorithm of a particle history is depicted in Figure 23. The particles are tracked throughout the Monte Carlo simulations beginning with the particle sampling from the given distribution (position, angle, energy). The path travelled until the next interaction is sampled based the cross-sections. At the boundary of the systems the particle is reflected or it leaks out, meaning that the particle history is ended. At each collision the interaction type and the collided nuclide is defined according to their cross-section. In case of a scattering, the characteristics of the scattered neutron are sampled again, followed by sampling the new path length. In case of a fission, the number of neutrons emitted and their characteristics are sampled, while a capture means the end of the neutron history.

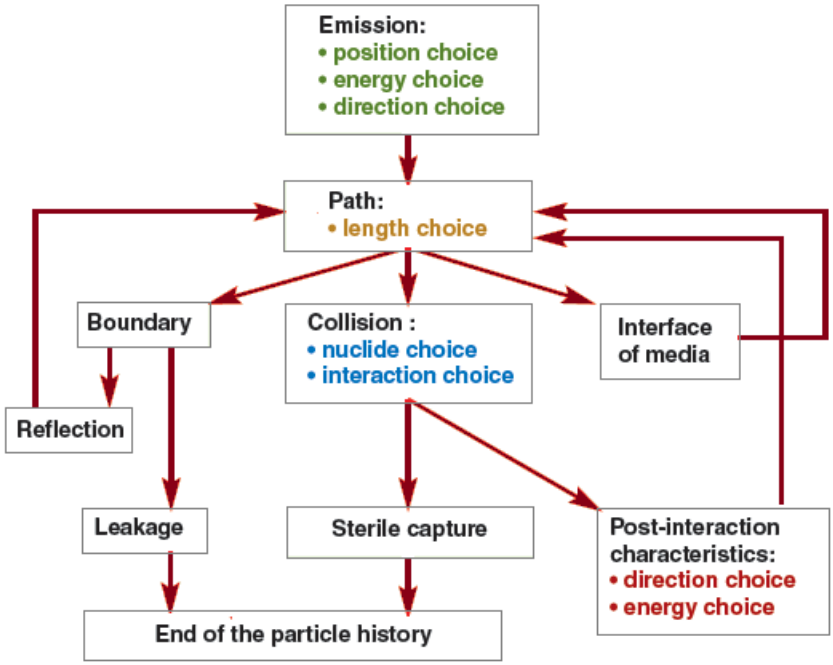


Figure 23. Simplified algorithm of particle history in Monte Carlo simulation (CEA, 2015)

The physical quantitates are evaluated through estimators. For example the flux can be estimated either with a track length path (defined as wl, where w is the weight of the particle and l the path length between two collisions) or a based on the total collision number (defined as $w/\Sigma(\vec{r}, E)$). Then the flux in a volume is given by scoring the chosen estimator for each event and multiplying these results with the corresponding cross-sections gives the reaction rates.

The stochastic code used during this work was the TRIPOLI-4® a 3D continuous-energy neutronics code developed at CEA for particle transport simulations (Brun, et al., 2015).

TRIPOLI-4® can simulate neutral particles (neutrons and photons) and charged particles (electrons and positrons). The neutrons are organized in batches and are simulated consecutively. In criticality mode, an initial guess neutron source is set for the first batch and the neutrons generated from fission are used as the sources for the next generation. This is referred to as the power iteration method, and the physical quantities are scored once convergence is attained (Brun, et al., 2015). In fixed-source criticality mode each batch begins with the same imposed source and the fission neutrons produced can be either discarded or explicitly simulated. In shielding mode the source is also fixed but the particles cannot create new fission neutrons and they are followed until they disappear. Fixed source mode and shielding mode are used for radiation protection and shielding analysis, while criticality mode is used to obtain the core characteristics such as k_{eff}, flux shape etc.

2.2.4. Non-stationary neutron transport

In static Monte Carlo calculations there is no distinction made between the prompt and delayed neutron population. Both are considered to be released instantaneously with the approximation that the delayed neutrons have the same energy spectrum as the prompt neurons. In kinetic calculations, especially for fast kinetics phenomena such as a reactivity insertion, the neutron and precursor populations need to be accounted for independently. This presents major challenges due to both the size and time scale differences of the two populations. The prompt neutron generation time is ~20 μs while the precursor mean lifetime is ~0.1 s (Ott & Neuhold, 1985). In other words, the precursor disappearance happens with orders of magnitude slower than the fissions, i.e. the precursor creation. This leads to an unbalanced ratio between the precursor and neutron population in the order of 10^4 in case of a typical PWR.

The treatment of the neutron-precursor system and the introduction of the time dependence required the development of specific simulation techniques. These techniques include the critical source sampling, population importance, the development of new variance reduction and population control methods (Faucher, et al., 2018), briefly presented in the following sections.

2.2.4.1. Critical source generation

A transient implies the departure of a critical system from its stationary state. For the kinetic simulation this implies a preliminary step consisting of the definition of the critical source. The critical source generation corresponds to solving the steady-state transport equation (2.7) and sampling the neutron and precursor population at the equilibrium. A regular power iteration is run over a large number of inactive cycles (neutron generations) and the values sampled during these cycles are not considered for statistical sampling. During the last inactive cycle,

the critical flux is converted into neutron and precursor densities. These particles are then injected into the kinetic calculations at t_0, and followed until the defined stopping time.

The number of the neutrons at equilibrium is defined as (Sjenitzer, 2013):

$$n^{eq}(\vec{r}, E, \vec{\Omega}) = \frac{\psi(\vec{r}, E, \vec{\Omega})}{\upsilon \, \Sigma_t(\vec{r}, E)} \tag{2.17}$$

Where $\psi(\vec{r}, E, \vec{\Omega})$ is the collision density, i.e. the number of neutrons entering a collision at a defined point, and υ is the neutron speed and Σ_t the macroscopic total cross-section.

The precursor source is given by (Sjenitzer, 2013):

$$C^{eq}(\vec{r}) = \frac{1}{\bar{\lambda}} \iint \nu_d(E') \frac{\Sigma_f(\vec{r}, E')}{\Sigma_t(\vec{r}, E')} \psi(\vec{r}, E, \vec{\Omega}) d\vec{\Omega}' dE' \tag{2.18}$$

Where $\bar{\lambda}$ is the family averaged decay rate of the combined precursors, ν_d is the number of delayed neutrons and Σ_f the macroscopic fission cross-section.

In kinetic calculations even small deviations from criticality can lead to a system that will drift away from the stationary state without any external reactivity change. This is especially important because the multiplication factor is rarely exactly 1.00000 even for a critical configuration, due to the possible uncertainties concerning the nuclear data, geometry, material balance and technological parameters. To overcome this problem, the number of neutrons produced by fission has to be rescaled by the multiplication factor obtained from a preliminary criticality calculation. The evolution of the flux for the same configuration with and without rescaling, and without external reactivity modification is shown in Figure 24.

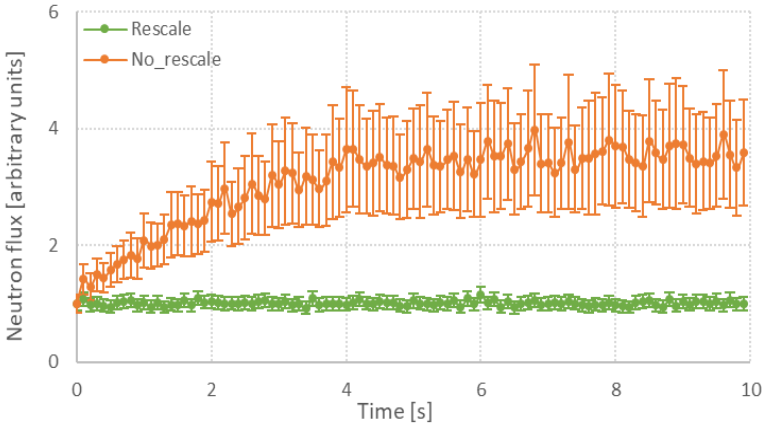


Figure 24. Time evolution of the total neutron flux in the CABRI core computed with TRIPOLI-4® with (green) and without (orange) rescaling the fission neutron number

2.2.4.2. Introduction of the time dependence

In steady-state simulations, the phase space consists of space, energy and angle coordinates. As such, the events are recorded independently of their time of occurrence. In order to allow time-dependent particle tracking, in kinetic simulations the particle histories are simulated over consecutive time intervals, and each particle is assigned a time label. The scores are added over the time steps and the different variance reduction and population methods are applied at the end of the time bins. The simulation time grid and time steps are defined by the user according to the problem at hand.

In steady-state calculations when a particle crosses a time bin, its trajectory is not changed but the scores are counted according to the scoring mode. If a collision estimator is used, each collision is taken into account in the time bin when was produced. If a track length estimator is used, only the track before the boundary is counted in the score of the boundary. In dynamic calculation however, a particle is followed until it is absorbed, leaked out or arrives at the time boundary. During its existence, a particle can create new particles that will be simulated right after the current particle. However, at the time boundary, all particles must be stopped and stored for the next time bin, since the system properties can be changed at the time boundary. Once all particles in the current time bin have been simulated, the scores are calculated, population control is performed and the system's properties are changed (if needed). The definition of the simulation time grid and time bins is an important step of the kinetic simulation.

2.2.4.3. Forced decay

The abundant precursor population and their long decay time compared to neutron lifetime means that in an analog Monte Carlo simulation no neutron would be produced between the creation of the precursors and its decay (see Figure 25). Since the precursor decay can be a relatively long process, this would mean that there could be time bins without neutrons, leading to variance jumps between time bins. In order to decrease the variance, the decay of the precursors is enforced at each simulation step. To not introduce a bias, the weight of the produced delayed neutron is adjusted accordingly. Once a precursor has decayed, it is added to the buffer particles (i.e. they do not contributed to the scores) for the next time step, while the produced delayed neutrons are tracked in the current time step.

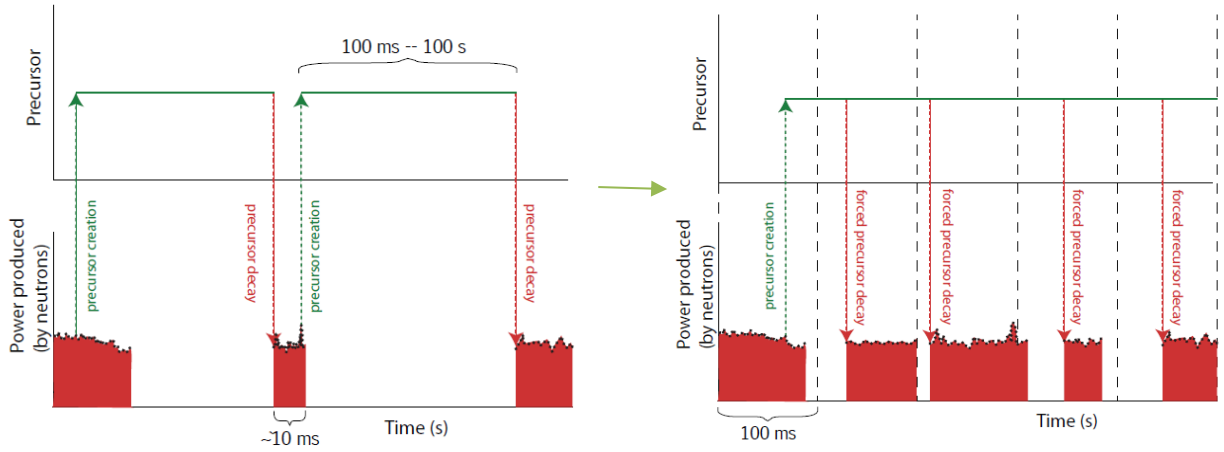


Figure 25. A schematic representation of a neutron chain with and without forced decay (Sjenitzer, 2013)

2.2.4.4. Population control

To avoid the neutron and precursor populations disappearing or growing out of bounds in a sub- or supercritical system, control mechanisms have to be applied. There are two population control mechanisms that can be used: *Russian roulette and splitting* or *combing*.

Russian roulette and splitting can be applied separately for neutrons and precursors. The only difference being that in the case of precursors, the roulette is applied based on the expected weight of the delayed neutron resulting from the decay of the precursor. If the weight of a particle falls under a pre-defined threshold, Russian roulette is applied to the particle, i.e. the particle is either removed with a given probability, or its weight is increased based on its probability of survival. In the case where the weight of the particle exceeds the defined threshold, the particle is split into n identical particles, with $1/n^{th}$ of the weight of the initial particle.

The second type of population control used in TRIPOLI-4® is the combing method. At the end of a given time step, the current neutron or precursor particle, with its associated total weight (W), is combed into M particles (value set by the user) with the total weight of W. The mechanism is depicted in Figure 26. The value of ξ, which determines the first particle to be copied, is a random variable.

It was found in (Faucher, 2019) that the combing method is more efficient that Russian roulette and splitting, specifically in cases where there is a significant population size variation.

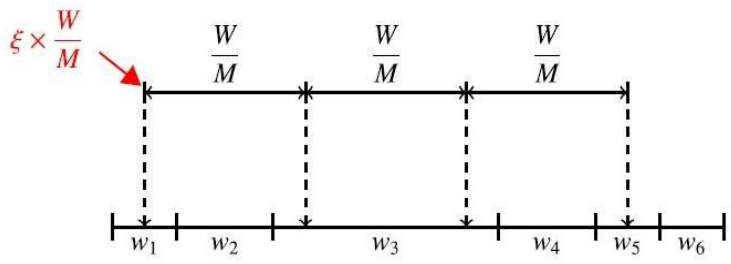


Figure 26. Application of the combing method: The total weight of the 6 particles is redistributed over 4 particles, each with a weight of *W/4* (Faucher, et al., 2018)

2.2.4.5. Population importance method

The weight of a delayed neutron is proportional to the time step. Thus, in case of a fast transient, the simulation of which requires a fine discretization in time, the weight of most of the delayed neutrons will be too small and they will be killed by Russian roulette. Ultimately, this would lead to under-sampling issues since there would not be enough delayed neutrons to initiate fission chains.

To overcome the under-sampling of neutrons when using short timescales, a time-dependent importance scheme was implemented in TRIPOLI-4®. This importance scheme relies on the introduction of importance factors, representing the actual number of physical neutrons and precursors the simulated, for the neutron (precursor) populations. The user can define a different importance ratio (*R*) for each simulation time step *i*, if needed, as $R = I_{N,i}/I_{C,i}$, where $I_{N,i}$ and $I_{C,i}$ are the neutron and precursor importance factors. Then, at the beginning of each time step, the importance factors are calculated by the code based on the current particle weights, while also preserving the total neutron and precursor population weight ($W_{N,i}, W_{C,i}$), as follows:

$$W_{N,i} \cdot I_{N,i} = W_{N,i+1} \cdot I_{N,i+1} \tag{2.19}$$

$$W_{C,i} \cdot I_{C,i} = W_{C,i+1} \cdot I_{C,i+1} \tag{2.20}$$

$$W_{N,i} + W_{C,i} = W_{N,i+1} + W_{C,i+1} \tag{2.21}$$

In application this means that when a neutron creates a precursor, the precursors weight is multiplied by *R*, while the created neutron's weight is divided by *R* when the precursor decays. The scores in turn are multiplied by their corresponding importance factors (I_N and I_C).

The optimal importance ratio depends on the kinetic parameters, inserted reactivity and simulation time grid (i.e. time steps). Several studies were conducted in (Faucher, 2019) regarding the definition of an optimal importance ratio. The impact of the choice of the

importance ratio was compared based on the efficiency of the calculations, which is described by a figure of merit (FOM), defined as:

$$\mathrm{FOM} = \frac{1}{\sigma^2 \mathrm{T}} \tag{2.22}$$

Where σ is the standard deviation of the score and T is the simulation time.

It was observed that while the gain in the FOM is more important for smaller time steps, the optimal importance ratio actually does not depend on the time step length. There is a wide range of optimal importance ratio for a given transient and for a core configuration with kinetic parameters typical of a PWR, a ratio of 10^{-3} is a good generic choice.

A correlation can also be defined between the optimal importance ratio and the time step. If *n* is the number of neutrons and *c* is the number of precursor in a given time step *dt*, then the number of neutron can be expressed as:

$$\mathrm{n} = \mathrm{c} \cdot (1 - \mathrm{e}^{-\lambda \mathrm{dt}}) \tag{2.23}$$

On the other hand, the number of neutrons can also be expressed with the help of the importance factor and importance ratio. The number of neutrons (precursors) N_n (N_c) present in the simulation multiplied by the neutron (precursor) importance factor I_n (I_c), equals the number of the physical neutrons (precursors) simulated. The ratio of the neutrons and precursors can be expressed as:

$$\frac{N_n \cdot I_n}{N_c \cdot I_c} = \frac{N_n}{N_c} \cdot R = \frac{n}{c} = (1 - e^{-\lambda dt}) \tag{2.24}$$

Then the optimal importance ratio (R_{opt}) is given by:

$$R_{opt} = \frac{(1 - e^{-\lambda \cdot dt})}{\frac{N_n}{N_c}} \tag{2.25}$$

The value for the ratio of simulated neutrons and precursors (N_n/N_c) was defined as 0.025, based on a test case presented in (Faucher, 2019) where the optimal importance ratio had been already found. With the decay constant being 0.125 s^{-1} for a PWR type of reactor, the optimal importance ratio can be calculated as:

$$R_{opt} = \frac{1 - e^{(-0.125 \cdot dt)}}{0.025} \tag{2.26}$$

It is important to note that the importance ratio has a significant impact on the simulation time. The smaller the importance ratio, the more neutrons are simulated leading to a significant increase in the simulation time.

2.3. PhD thesis objectives

Besides modelling and simulating a RIA transient, the main goal of the thesis was to calculate the dynamic energy deposition into the test pin and the dynamic coupling factor. The coupling factor is currently measured and calculated in steady state, with the reactor being at nominal conditions, and it is assumed constant and valid for the transient state. There are several approximations introduced by this assumption, such as not taking into consideration the possible influence of the helium depressurization and the reactivity feedbacks on the neutron flux and spectrum. Both of these could modify the value of the previously estimated coupling factor.

In order to improve the current energy deposition calculation methodology by taking in to account these effects, the stepwise calculation methodology was developed, which allows observing the possible variations in the parameters of interest with the static TRIPOLI-4® already at our disposal. Then, as a second methodology, the transient is simulated with the kinetic module of TRIPOLI-4®.

There are two approaches used to calculate the dynamic energy deposition using TRIPOLI-4®. In the first approach, the energy deposited is estimated based on the energy released following a fission event, using either the static or the kinetic module in TRIPOLI-4®, while in the second approach the energy deposition is calculated based on nuclear heating, and was only tested using the static TRIPOLI-4® module, due to computational limitations.

2.3.1. Energy deposition estimated from fission energies

The parameters of interest (energy deposition and coupling factor) are computed with the static or kinetic TRIPOLI-4®. This methodology is based on the assumption that the energy released during a fission event is deposited entirely at the place where the fission took place. The power is obtained by multiplying the fission reaction rates computed by TRIPOLI-4® for each fissile isotope present in the studied volume with the corresponding fission energy (refer to Table 2). Then the energy deposition is calculated by integrating the power over the duration of the transient. This integration, although straightforward in the case of the dynamic scheme where the results are time-dependent by default, requires further considerations in the case of the stepwise methodology.

2.3.1.1. STEPWISE CALCULATION SCHEME

The stepwise calculation scheme is based on the quasi-static method. The neutron flux shape is computed by running criticality calculations for the configurations representative of the different stages of the transient. The amplitude function, which in this case corresponds to the power, can be obtained via either a point kinetics solver or by normalizing the static results to the power evolution obtained with PALANTIR. In the former case, the kinetic parameters needed to obtain the power are computed during the criticality calculations. The power computed with the point kinetics solver is used to validate the modelling choices, as it is detailed in section 3.2. The latter methodology, used to obtain a time-dependent power, is detailed in the following.

By default in a static TRIPOLI-4® calculation, the scores are normalized to 1 source neutron. In order to scale the results to the actual core power a normalization factor needs to be defined. With $\tau_{fission,i,n}$ being the fission reaction rate in the core computed by TRIPOLI-4® in criticality mode for the n^{th} geometry, $E_{fission,i}$ being the energy released during fission for the fissile isotope i and $P_{core,n}$ the core power calculated with PALANTIR and corresponding to the chosen geometry, the normalization factor (N_n) of the given core configuration is defined as:

$$N_n[-] = \frac{P_{core,n}}{\sum \tau_{fission,i,n} \cdot E_{fission,i} \cdot 1.602 \cdot 10^{-19}} \tag{2.27}$$

By definition this calculation scheme allows the calculation of the instantaneous parameters, associated with a given core configuration. The instantaneous power (P_{inst}) is calculated from the normalized fission reaction rates ($\tau_{fission}$) and fission energies ($E_{fission}$) taking into account the individual contribution of each fissile isotope i for each volume considered:

$$P_{inst,dt}^{core} = \sum \tau_{fission,i}^{core} \cdot N_n \cdot E_{fission.i} \tag{2.28}$$

$$P_{inst,dt}^{pin} = \sum \tau_{fission,i}^{pin} \cdot N_n \cdot E_{fission.i} \tag{2.29}$$

However, the instantaneous power is not enough to calculate the energy deposition. For that the time-dependent power is needed. The time depended power the power is linearly interpolated between two instantaneous values with the assumption that the power remains constant after the final core configuration (since there is no significant change in the core parameters following the final geometry).

More precisely, the linear interpolation between two consecutive steps (t_{n+1} and t_n) can be written as:

$$P_i = P_n + \frac{P_{n+1} - P_n}{t_{n+1} - t_n} \cdot (t_i - t_n) \tag{2.30}$$

Where P_i is the interpolated power at time t_i, and P_{n+1} and P_n are the instantaneous core power calculated at step t_n and t_{n+1}respectively. This interpolation is done for both the core and test pin power, and the resulting power curve is referred to as the stepwise power. This is a first approximation and depending on the geometry choices, it might lead to an over- or underestimation of the time-dependent power (compared to the computed or experimental power). Thus, more intermediate power normalization steps might be needed. A detailed stepwise power calculation is presented in the ANNEX A.

Once the time-dependent power is obtained, the energy deposition in the core and in the test pin (E_{dep}), referred to as the stepwise energy deposition, is calculated by integrating by the trapezoidal rule the stepwise core and pin power:

$$E_{dep} = \sum_i E_i = \sum_i E_{i-1} + \frac{P_i - P_{i-1}}{2} \cdot (t_i - t_{i-1}) \tag{2.31}$$

Where E_i is the energy deposited at time t_i, P_i and P_{i+1} are the interpolated power at time t_i and t_{i+1} respectively. In addition, an instantaneous coupling factor (C_{inst}) can also be calculated for each core configuration as the ratio of the core and test pin power presented in Eq. 2-7.

$$C_{inst} = \frac{P_{core,n}}{P_{pin,n}} = \frac{\sum \tau_{fission,i}^{core} \cdot E_{fission.i}}{\sum \tau_{fission,i}^{pin} \cdot E_{fission.i}} \tag{2.32}$$

Similar to the power interpolation, a time-dependent coupling factor can be calculated by interpolating between two consecutive instantaneous coupling factors. This is referred to as the stepwise coupling factor (C_{step}). A graphical representation of the instantaneous and stepwise values are shown in Figure 27.

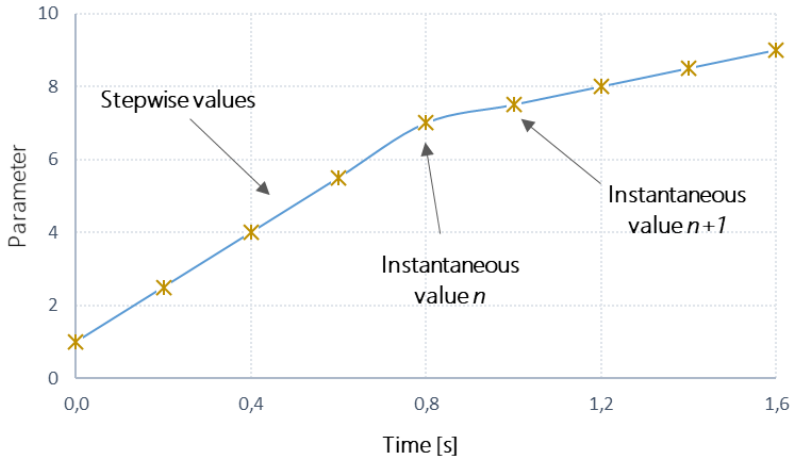


Figure 27. Definition of the instantaneous and stepwise values

2.3.1.2. DYNAMIC CALCULATION SCHEME

In the dynamic calculation scheme, the scores need to be normalized only to the steady-state power, i.e. to the core power at the critical core configuration. Secondly, since the results are inherently time-dependent and defined for a chosen time scale, there is no need for power interpolation. Then for each time step dt the power can be rewritten as:

$$P_{dyn,dt}^{core/pin} = \sum_i \tau_{fission,i}^{core/pin} \cdot E_{fission.i} \cdot N \tag{2.33}$$

Multiplying the power by the time step gives the energy deposition over that time step. Then summing the energy deposition over all n time steps gives the energy deposition throughout the transient:

$$E_{dyn}^{core/pin} = \sum_n P_{dyn,dt}^{core/pin} \cdot dt \tag{2.34}$$

Finally, the dynamic coupling factor ($C_{dyn,dt}$) is also calculated at each dt time step, as the ratio of the core and test pin power:

$$C_{dyn}(t) = \frac{P_{core}\ (t)}{P_{pin}(t)} = \frac{\tau_{fission,i}^{core}(t) \cdot E_{fission.i}}{\tau_{fission,i}^{pin}(t) \cdot E_{fission.i}} \tag{2.35}$$

2.3.2. Energy deposition based on nuclear heating

In order to account for the spatial distribution of the energy generated during fission, the energy deposition can be calculated from nuclear heating. In the case of power reactors, nuclear heating is expressed in terms of energy deposition (W/g) in a given volume. TRIPOLI-4® computes the energy deposition for each transported particle based on the energy balance method (Peron, 2014), by subtracting the energy carried away by transported particles from the available initial kinetic energy.

In order to be able to estimate the prompt and delayed nuclear heating, a two-step calculation scheme is needed. This scheme, summarized in Figure 28, was first developed for the assessment of nuclear heating in the heavy reflectors of GEN-II reactors during a previous thesis (Ravaux, 2013) reproduced later for the Jules Horowitz Reactor (JHR) in (Lemaire, 2015) and later implemented for the CABRI reactor. First, the prompt heating is calculated with TRIPOLI-4® in criticality mode. The delayed source, needed for the delayed heating calculation, is obtained with the DARWIN depletion code (Roque, et al., 2002) and it is propagated during a fixed-source TRIPOLI-4® calculation, in order to get the delayed energy deposition. These calculation steps are detailed in the following sections.

The prompt heating is obtained by running a criticality TRIPOLI-4® simulation with 4 particles, (n, γ, e-, e+). The code estimates the local energy deposition in every volume of interest (i.e. the different structures of the pressurized water loop, including the test pin) and for each particle. The energy deposited by neutron is referred to as the neutron heating, while the gamma heating covers the sum of the energy deposited by photons, electrons and positrons.

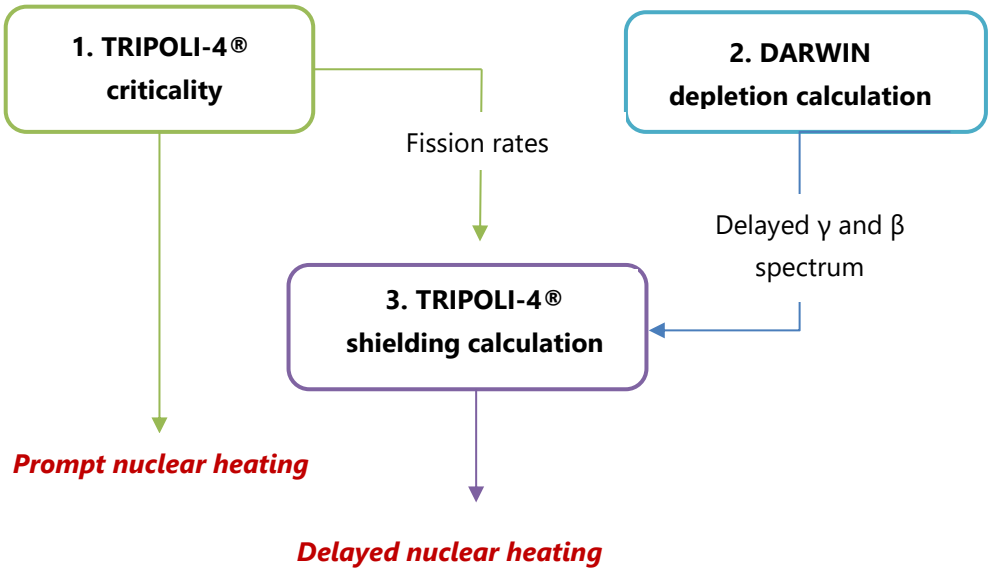


Figure 28. Nuclear heating calculation scheme

The delayed heating is computed with TRIPOLI-4® in a fixed source simulation mode. The delayed nuclear heating is calculated by running a fixed-source TRIPOLI-4® simulation in shielding mode with 3 particles (gamma, electron and positron) for each component of the delayed source: the delayed gamma and beta emissions following the fission of the existent isotopes.

In order to be able to define the delayed source in a fixed source calculation, such as needed for the delayed heating calculation, the spectrum and the multiplicity (the number of emitted particles/rays) of the source have to be determined with the PEPIN module of the DARWIN depletion code. DARWIN is a code package, developed at CEA dedicated to fuel cycle studies. The PEPIN2 module calculates the evolution of the concentration of the fission and activation products following a fission event (in the current case) by solving the Bateman equation. From this concentration, the code is able to determine the mass, the activity, the residual heat, the number of emitted particles and the spectrum for each time step and for each energy group.

Given the short time scale of the CABRI test (~1 hour of irradiation time), the variation in the fuel composition is considered negligible. The aim of this step is to define the delayed β and γ emissions of a given fissile isotope over the irradiation time. Cooling time is not considered since the parameter of interest is the energy deposition during the transient. Integrating these emissions over the irradiation time gives the average delayed emission spectrum and multiplicity for the given fissile isotope. The detailed delayed spectrum calculation steps, based are presented in the ANNEX B.

3. TRANSITION FROM A STEADY STATE TO A TRANSIENT CALCULATION

3.1. Modelling a CABRI transient

A continuous depressurization cannot be simulated with the stochastic codes available. As a result, depressurization is modelled as step-depressurization, represented by a succession of core configurations with decreasing pressure, referred to as *intermediate geometries* or *core configurations*. The same representations are used in both the stepwise and the dynamic scheme, given the capability of the kinetic module to handle changing geometries within a simulation (Faucher, 2019). In the case of the dynamic calculation scheme, a simulation time grid and the corresponding importance factors also need to be determined in addition to the intermediate geometries.

The reactor core, including the test loop, is accurately modelled with both a native TRIPOLI-4® (shown in Figure 29) and a ROOT geometry (Brun, et al., 2003), required for the kinetic module. The nuclear data library used for both the static and kinetic calculations is the CEAV5.1.2 library, obtained from the JEFF-3.1.1 nuclear data library.

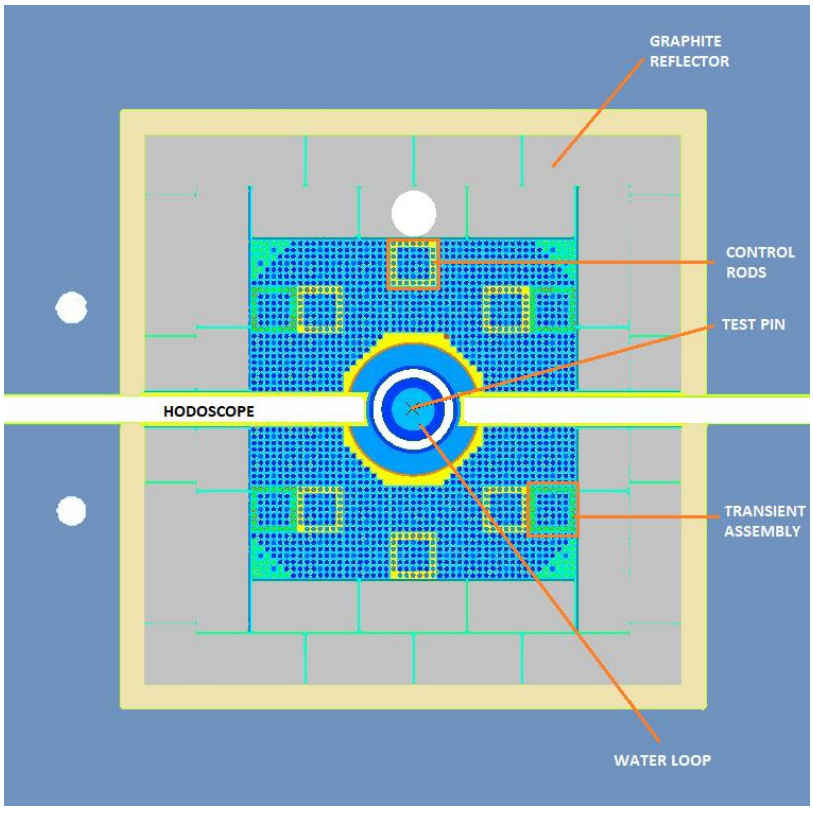


Figure 29. Radial cut of the CABRI core in the native TRIPOLI-4 geometry

Two types of transients are considered during this work: a supercritical and a prompt-supercritical transient, modelled based on the commissioning tests performed in 2017. The commissioning tests refer to depressurizations carried out without a test device in the pressurized water loop, with the aim is to verify the good operation of the different reactor systems and components. In the simulations presented in work, a test pin is included. It is identical to the pins of the core, but with a length of 50 cm instead of 80 cm, which is the typical length for the test pins used for the CABRI transients.

The next sections present the modelling choices and their justification for the two test cases. The latter is based on the comparison of the power curve obtained with the stepwise and dynamic methodology against the power evolution obtained with PALANTIR and the experimental power. A sensitivity study on the dynamic modelling as well as a discussion about the limitations of this module are also included.

3.1.1. Definition of the representative geometries

The reactivity insertion specific to the CABRI reactor consists of a rapid helium depressurization in the transient rods, followed by a power and subsequent fuel temperature increase. This temperature increase results in a Doppler feedback. Depending on the reactivity injection and the fuel temperature attained, it also leads to the expansion of the fuel pin and in the increase of the moderator temperature (through the heat exchange between the fuel and the moderator). While the Doppler feedback is instantaneous, the expansion of the fuel and the increase of the moderator temperature, and thus, the corresponding reactivity feedback, is a slower process.

As discussed in (Labit, 2020) it takes ~30 ms for the cladding to start to heat up and ~130 ms for the moderator temperature to increase following the temperature increase of the fuel. Therefore, the importance of the different phenomena that take place during a transient can be ranked based on the transient type (i.e. the reactivity injection and the pulse length) as it was done in the framework of a quantitative phenomena identification and ranking table (QPIRT) presented in (Labit, 2020). This QPIRT revealed that the most important phenomena for any type of transient is the reactivity injection and the Doppler feedback. On the other hand, the feedbacks related to the fuel expansion and moderator temperature increase become significant only for transients characterized by an important energy deposition in the core (> 200 MJ) and a long (>30 ms) power pulse.

The transients discussed during this work are either low energy transients (such as the supercritical case) or fast (short pulse) transients with moderate to high energy injection. In other words, the impact of the moderator and fuel expansion feedback is negligible. As such, any intermediate core configuration can be represented by a corresponding helium pressure and fuel temperature. The pressure and temperature variations during the transient are

obtained with the PALANTIR code. Intermediary geometries are then selected at each instant where either the pressure drop is larger than a given threshold or the temperature increase is superior to a threshold value. These pressure and temperature difference thresholds are defined case by case in order to capture the impact of the reactivity insertion and of the Doppler feedback on the energy deposition. The geometry change is instantaneous and the instant of the geometry update is defined by the geometry choice. The chosen test cases and the chosen intermediate geometries are presented next.

Supercritical transient

A depressurization from 0.73 bar was chosen for the supercritical test case. The depressurization corresponds to a reactivity insertion of approximately 560 pcm, turning the reactor into a supercritical system. The initial core power is 0.1 MW and maximum power attained during this transient is 0.7 MW, resulting in an energy deposition of 0.56 MJ in the core. The helium pressure and fuel temperature variation is presented in Figure 30. Due to the low energy injection, the moderator temperature increase is negligible (<1 K).

The fuel temperature increases by 3 K. With the current simulation options and code version, it is not possible to use temperature interpolation; instead, tabulated temperatures have to be used. However, around 300 K the tabulated temperatures are 294 K, 300 K and 314 K. Thus, the lowest tabulated temperature difference around 300 K is 6 K, and as a result, the 3 K fuel temperature increase during this transient could not be modelled. As currently the test pin is not modelled in PALANTIR and there is no experimental data on the fuel pin temperature variation from the commissioning tests, the choice was made to model the test pin behavior based on the fuel pins in the driver core. Similarly, the pressurized water loop is modelled as having the same condition as the reactor core: ambient pressure and 20°C moderator temperature. In the driver core, every fuel pin is considered to have the same temperature and temperature variation throughout the transient. This impact of this approximation is discussed later.

Thus, the choice of geometries for this transient was defined solely based on the helium pressure. As such, an intermediate geometry was defined at each point where the pressure decreased by 25%. The chosen core configurations are shown in Figure 30. The dynamic simulation starts from the critical core configuration. The time where the given pressure was attained during the experiment defines the instants of the geometry change in the dynamic calculation. Then the first geometry change, which signifies the start of the depressurization, happens at 0.003 s, followed by geometry changes at 0.015 s, 0.035 s and finally at 0.09 s. The transient is simulated until 1 second, and the rod drop is not modelled.

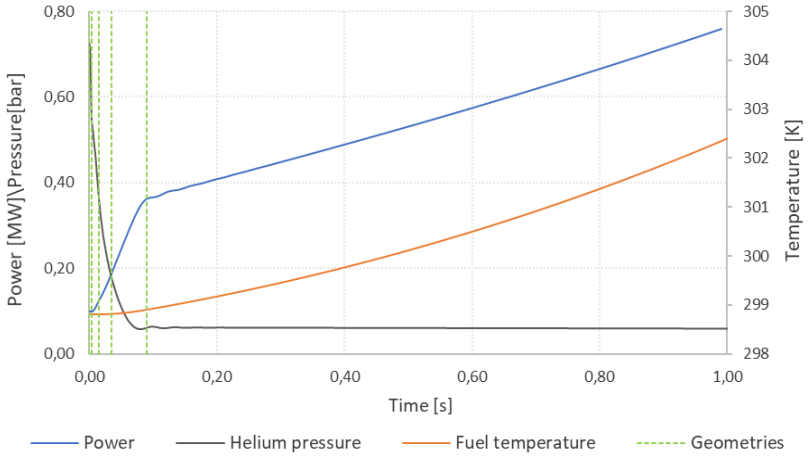


Figure 30. Evolution of the main parameters during the supercritical transient. Results obtained with PALANTIR. The vertical green lines represent the chosen core configurations.

Prompt-supercritical transient

A depressurization from 1.4 bar with a moderate reactivity insertion of 860 pcm was considered as a test case for the prompt-supercritical transient. This results in a power peak of 230 MW and in an energy deposition of 22 MJ at 1 second. The power surge is terminated by the Doppler feedback. The helium pressure and fuel temperature variation is presented in Figure 31. The geometries are chosen as to account for the reactivity insertion (helium depressurization) and the Doppler feedback (fuel temperature increase).

An intermediate geometry is chosen when either the pressure difference between the current and previous configuration is greater than 0.4 bar or the temperature increase is greater than 25°C, starting from the critical core configuration. Similarly, to the supercritical transient, the test pin temperature and temperature evolution is the same as the fuel temperature evolution in the driver core, which is defined as the average of the assembly-wise temperatures given by PALANTIR.

The dynamic simulation starts from the critical core configuration and the geometry changes happen at 0.005, 0.015, 0.03, 0.055, 0.06, 0.1, 0.15, 0.17 and 0.19 second. The transient is simulated until 0.6 seconds and the rod drop is not modelled.

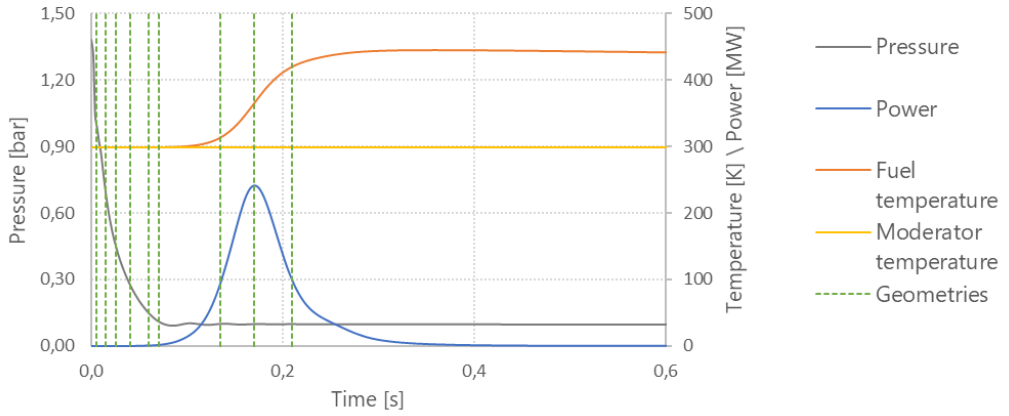


Figure 31. Evolution of the main parameters during the prompt supercritical depressurization. Results obtained with PALANTIR. Vertical green lines represent the chosen core configurations

3.1.2. Implementation of the dynamic module

Asides from the definition of the geometries and geometry change instants, the kinetic module requires the definition of the simulation time grid, more specifically the simulation time steps, and the associated importance ratio. The importance ratio is proportional to the actual time step and the analytical expression for the optimal time step is presented in Chapter 2.2.4.5. In order to have an accurate representation of the transients, these parameters have to be calculated case by case, taking into account the specificities of the transient. The definition of other specific kinetic parameters, such as the rescaling factor or population control method, is generic and not dependent on the transient to be modelled.

The time step length needs to be defined in order to reflect the time behavior of the neutron population, which in the case of a reactivity insertion, can be described through two distinct phases.

In the fast kinetics phase, the characteristic neutron variation time can be described as the inverse of the prompt neutron decay constant: $\Lambda/(\beta - \rho)$. Based on the test cases presented in (Faucher, 2019), considered as reference for kinetic calculations, it was found that 5 time steps over a time span of 8 times the characteristic neutron variation time captures well the fast phase of the transient. This time grid then needs to be associated with an importance ratio to favor the delayed neutron production. In the slow kinetics phase, representing the asymptotic power increase, longer times steps, in the order of a 0.1 s, are sufficient. This also implies that the importance ratio is no longer needed.

Furthermore, if there is a geometry change during the simulation, the instant of the geometry change needs to be part of the time grid. Finally, when defining the number of time step it should be taken into account that the running time is proportional to the square of the number

of time steps. In the case of the supercritical transient, this resulted in 0.009 s time steps during the fast phase and 0.025 s time steps during the slow phase, while in the case of the prompt supercritical transient, this gives 0.005 s time steps for the fast phase and 0.1 s time steps for the slow phase.

3.2. Justification of the modelling choices

Two aspects need to be considered when choosing the intermediate geometries. The spatial and spectral neutron flux variation during the transient has to be accounted for and the reactivity insertion has to be correctly modelled.

The first aspect is ensured by taking into account the variation of the physical parameters that affect the neutron population evolution. For the two test cases and current modelling approximations (fuel expansion is not considered and the control rod drop is not modelled) these parameters are the helium pressure, inducing flux variation around the transient rods, and the fuel temperature, which defines the Doppler feedback. As such, the geometries are chosen in order to be representative of the main stages of the transient. In the case of the prompt supercritical transient the main stages are the early phase, where there is depressurization but no fuel temperature change, the pulse, where there is a significant temperature increase, but minimal pressure variation and the final stage, where both the pressure and temperature stabilized.

On the other hand, it is the reactivity insertion that drives the power evolution. This aspect is not essential for the stepwise methodology, since the power evolution is obtained by normalizing the instantaneous results to the calculated or experimental power curve. However, it is paramount in the case of the dynamic methodology, where the power evolution is calculated from the reactivity insertion defined by the chosen geometries.

To ensure that the reactivity insertion is representative, the power evolution is computed using the point kinetics equations (2.9) and (2.10), which gives an estimate of the power evolution dictated by the chosen geometries. The parameters needed for solving the point kinetics equations, such as the reactivity, prompt neutron lifetime and the effective delayed neutron fraction are obtained by running a static calculation for each geometry. The power calculated with point kinetics is compared to the power obtained with PALANTIR. This represents the first validation step.

The next and final validation step is to compare the dynamic power evolution obtained with the kinetic TRIPOLI-4® with the experimental power.

3.2.1. Power evolution calculated with point kinetics

The power evolution is calculated by solving equations (2.9) and (2.10), where the kinetic parameters, such as the delayed neutron fraction, generation time and reactivity were obtained by running a criticality calculation for the chosen geometries. In (Clamens, 2018) it was shown that the uncertainty on the kinetic parameters due to nuclear data does not have a significant impact on the power calculation. Nevertheless, in order to obtain the sensitivity of the point kinetics calculation to the calculation uncertainty (0.2% in case of the delayed neutron fraction and generation time and 5 pcm for the reactivity) additional calculations were run with the kinetic parameters varied according to their statistical uncertainties.

The results are summarized on Figure 32. The uncertainties on the effective delayed neutron and generation time does not impact significantly the power calculation, the final power variation is under 1%. On the other hand, the uncertainty on the total reactivity insertion has great impact on the power calculation: 1 pcm uncertainty equals to roughly 1% variation in the final power. Thus, for the future results, 5% uncertainty will be applied on the power calculation with point kinetics. Unless mentioned otherwise, the statistical uncertainties presented throughout this work are given at 1σ.

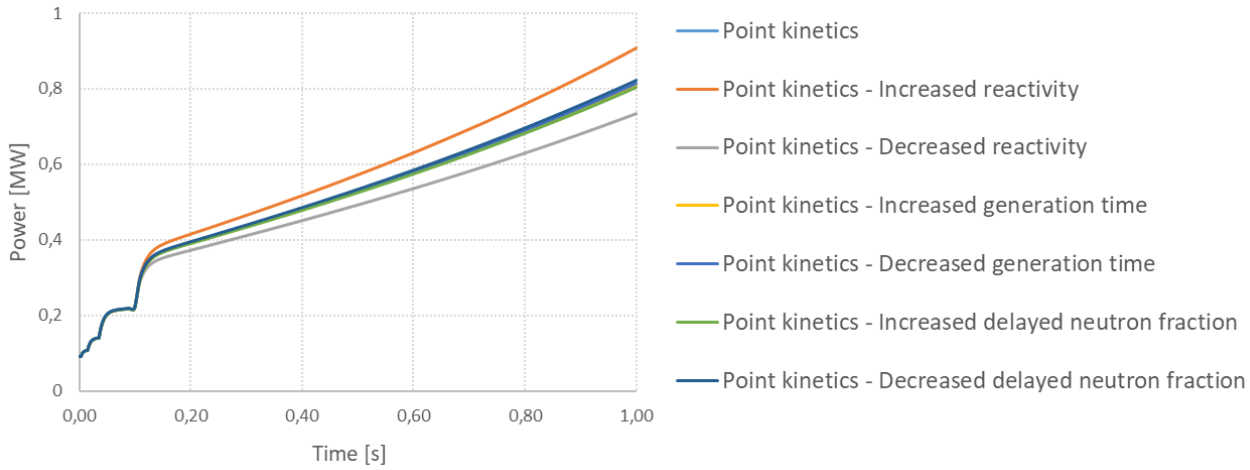


Figure 32. Power calculated with the point kinetics solver

Supercritical transient

Figure 33 shows the power evolution predicted by point kinetics in comparison with the power calculated with PALANTIR. The power jumps observed at the beginning of the calculation correspond to the geometry changes. The power underestimation observed in the early phase of the transient suggests that more intermediate geometries could be considered. However, the trend of the power evolution suggest that the total reactivity injection is well represented

with the current modelling. The power evolution obtained with point kinetics is in a good agreement with the power evolution obtained with PALANTIR.

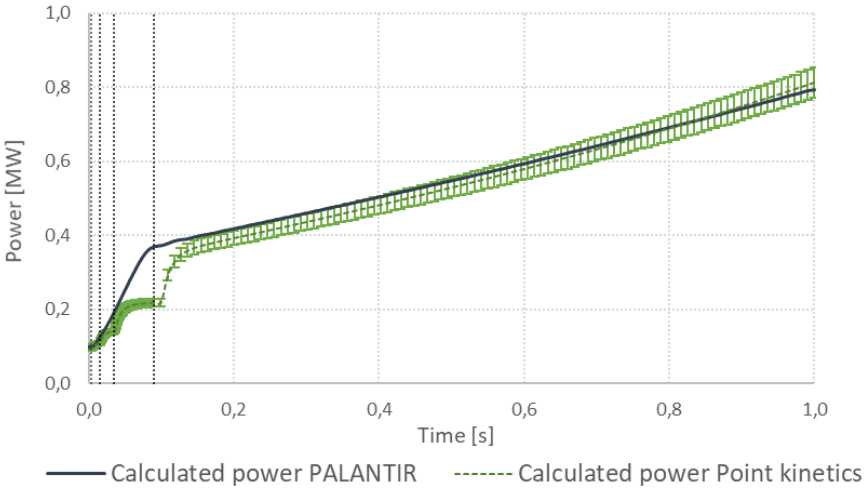


Figure 33. Power evolution obtained with PALANTIR and using point kinetics. Vertical lines represent the geometry changes

Finer reactivity steps (i.e. more intermediate geometries) would mean a better agreement between the calculated powers during the early phase of the transient, as demonstrated in Figure 34. Nevertheless, it does not influence the long-term evolution of the power, which is driven by the total reactivity insertion. Keeping in mind the high computational cost of the dynamic calculation (detailed in Chapter 2), and the good agreement in the long-term power evolution regardless the number of intermediate geometries, the original modelling with 3 intermediate geometries is retained for the dynamic simulation.

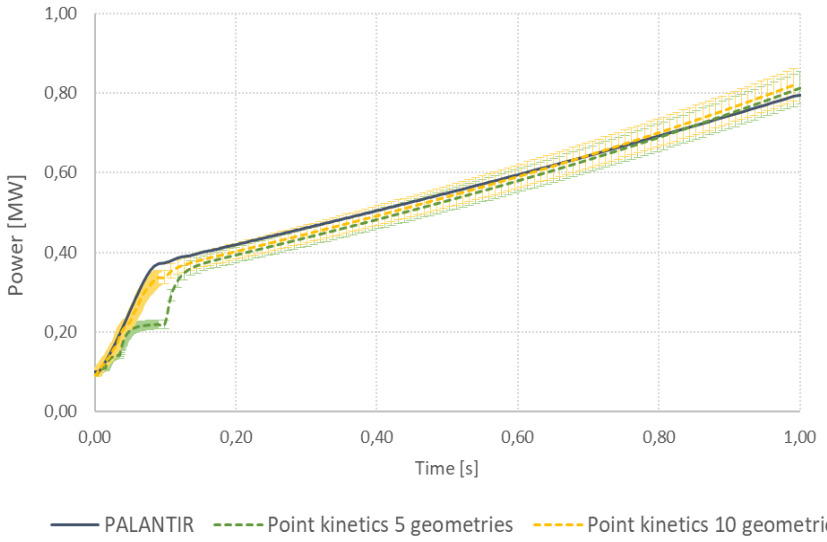


Figure 34. Impact of the number of geometries on the power calculated with point kinetics

Prompt supercritical transient

The power calculated with the point kinetics solver for the prompt supercritical test case is shown in Figure 35. This power evolution is in good agreement with the power computed with PALANTIR concerning both the power peak and the timing of the power pulse. Similarly, to the supercritical case, the impact of a finer depressurization steps was also considered, but it introduced no considerable improvement. As a result, the original modelling with 10 intermediate geometries was retained for the dynamic simulation.

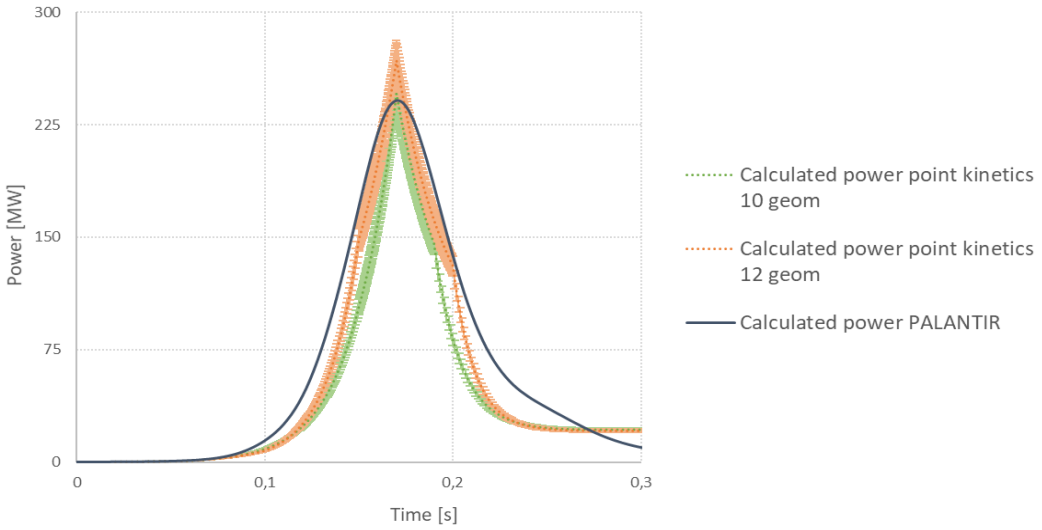


Figure 35. Power evolution obtained with PALANTIR and using point kinetics

3.2.2. Dynamic power evolution

As the last step, the dynamic power was computed for both the stepwise and dynamic transient and compared with the corresponding experimental and PALANTIR power curves.

Supercritical transient

The comparison between the calculated and experimental power evolution in the case of the supercritical transient is illustrated in Figure 36. The dynamic power evolution is in good agreement with the experimental and calculated power throughout the transient, validating the geometry and modelling choices and the kinetic module. The discrepancy between the experimental and calculated curve with the TRIPOLI-4® dynamic module is within the statistical uncertainty of the dynamic calculation, it is ~4% at 1σ.

The average discrepancy between the dynamic and experimental power is ~3%, which is within the statistical (4%) and measurement uncertainties (3%, (Clamens, 2018)), respectively.

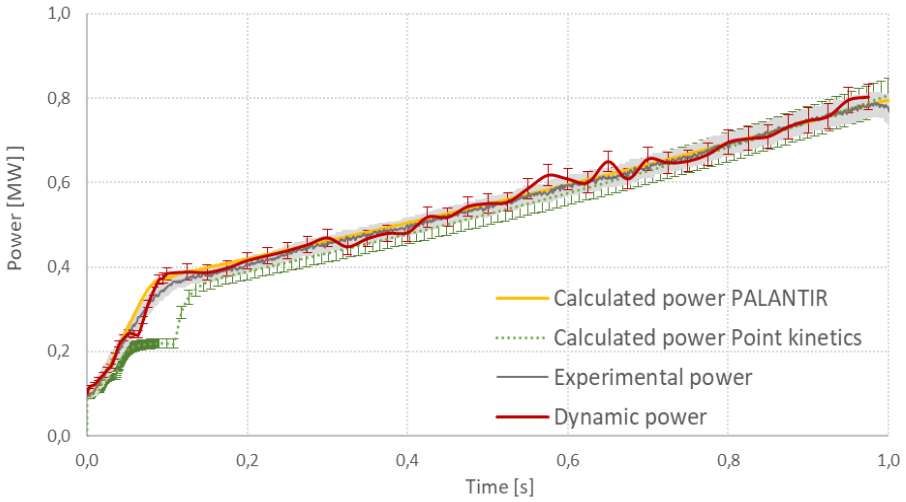


Figure 36. Comparison between the calculated and experimental power in the case of the supercritical transient. Uncertainties given at 1σ

Prompt supercritical transient

In the case of the prompt-supercritical transient it was found that, when calculating with the kinetic module, the power peak is underestimated by a factor of 100 (see Figure 37), although the timing of the peak is correct. In addition, this type of power underestimation was found to be characteristic to other prompt-supercritical transients analyzed, invalidating the results of the kinetic simulation.

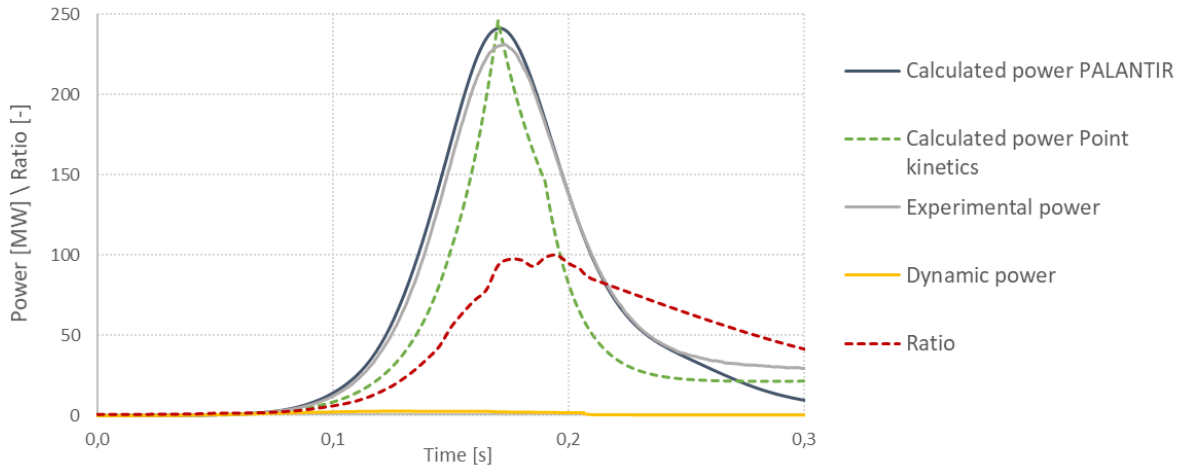


Figure 37. Comparison between the calculated and experimental power in the case of the prompt supercritical transient

An extensive study was conducted to investigate with the help of the code developer team the reasons to this underestimation problem. The consensus at the moment of writing is that the underestimation is not due to the modelling choices (supported by the point kinetics calculations) but is a limitation of the current kinetic module. A discussion on the observed limitations of the current kinetic code version is presented the following section.

3.2.3. Limitations of the dynamic module

One known constraint of the kinetic code is its significant running time, in the order of thousands of CPUh (Faucher, 2019) even for simplified models and moderate reactivity insertion. This was expected to be even more taxing in the case of prompt-supercritical transients where the power (neutron population) is governed by the prompt neutron lifetime (refer to equation (2.14)).

The simulation performed during this work revealed an additional limitation for the prompt-supercritical transients, namely that the power peak is significantly underestimated. The impact of these limitations on the modelling choices is discussed in the following section.

Running time

To give some perspective, our available computational resource is ~22000 CPUh per calculation. An average criticality calculation for the CABRI reactor, with a 0.1% accuracy on the flux in the test pin, takes 1500 CPUh. On the other hand, a dynamic calculation for the lowest reactivity insertion needs 13000 CPUh for an accuracy of 3% on the flux in the test pin.

There are several parameters that influence the running time, such as the transient type, the simulation time steps (and implicitly the number of geometries) and the importance ratio (implicitly, the number of simulated neutrons). It was observed early on that the most impactful parameter on the running time was the transient type, i.e. critical or prompt-supercritical transient. With the earliest version of the kinetic module simulating a supercritical transient with 10 million particles took 13000 CPUh, while in the case of a (slightly) prompt supercritical transient with the similar simulation parameters took 20000 CPUh. Based on these observations, an updated version of the code, with an optimized combing method for population control, was tested. This improvement greatly reduced the running time, allowing to extend the simulation domain to prompt-supercritical transients.

The simulation of a fast transient, such as the transients considered for this study, requires a fine time mesh with corresponding importance ratio. It was shown in (Faucher, 2019), the simulation time is proportional to the square of the number of time steps, thus, for each case, a compromise has to be found between the time domain covered by simulation and the number of time steps in order to maximize the accuracy of the results. For the prompt-

supercritical transients simulated (with a reactivity insertion lower than 900 pcm), ~60 time steps seemed to be a good compromise.

Ultimately, the long running time limits the number of neutron histories that can be simulated, resulting in a relatively high statistical error. This proved to be a limiting factor in the case of the supercritical transient, where the variations predicted in the parameters of interest were in the order of 2%, while the statistical error on the dynamic parameters were in the order of 3 to 5%. This meant that no conclusion could be drawn from the dynamic results concerning the evolution of these parameters during the transient.

Power underestimation

The type of power underestimation observed in the case of the prompt-supercritical transients suggested a normalization problem or an overall underestimation of injected reactivity. There are two normalizations steps in the dynamic calculation: the normalization factor and the normalization to the initial core power. Both of these steps are inherent to the calculation and are defined the same way as for the supercritical case. Furthermore, as it will be presented in the next section, the uncertainty in the power calculation due to the normalization and the rescaling factor is in the order of 3%, which does not explain the underestimation observed in the power evolution, which is in the order of 10000%. On the other hand, the power peaks calculated with point kinetics calculations when validating the geometry choices were in good agreement with the expected power peak, suggesting that the reactivity injection in the dynamic simulation is not underestimated.

In order to explain the power underestimation, the impact of the modelling parameters was also considered. More precisely, the impact of the geometry choice and the impact of the time step length. The impact of the geometry choice was analyzed by running two additional simulations: one where the number of geometries was increased and one where the depressurization was modelled as an instantaneous depressurization. Due to the long simulation time, in the former case the power evolution was simulated only until the power peak. In the case of the instantaneous depressurization, the critical core configuration was replaced by the core configuration with the lowest pressure but with no fuel temperature change at 0.15 seconds, followed by three more geometry changes, where only the fuel temperature is changed to account for the Doppler feedback. The possible impact of the simulation time steps was also considered, by comparing the power calculated with increased and decreased time steps. The variation of the time steps is in the order of 20%.

As it can be seen on Figure 38, using a finer modelling for the depressurization has no significant impact on the power peak attained, while the instantaneous depressurization results in an even greater power underestimation. The maximum power in this case is only 0.78 MW. The results showed that the decreased time step length had a negligible impact on the

maximum power attained, while increasing the timesteps resulted in a power 10% higher power peak, which is insignificant considering the discrepancy between the calculated and experimental power peak.

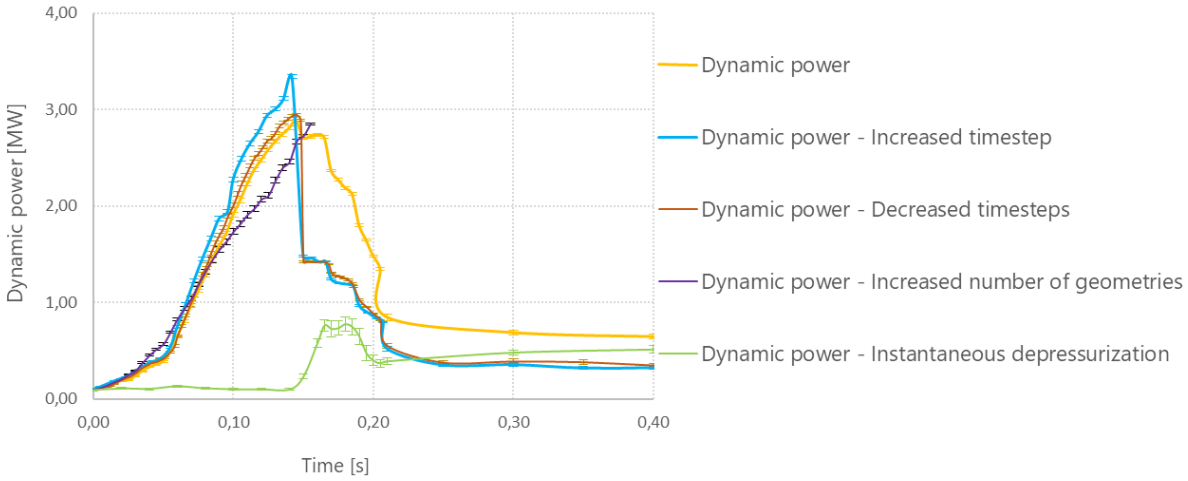


Figure 38. Impact of the modelling parameters on the power evolution in the case of a prompt supercritical transient

Similar studies were conducted for other prompt-supercritical transients as well, with initial pressures ranging from 1 to 1.4 bar and a maximum reactivity insertion of 870 pcm. The power evolution showed the same underestimation as observed in the case of the 1.4 bar depressurization. The reason for the power underestimation for prompt supercritical transient is not yet known, and it requires further analysis. However, the fact that the power calculated with point kinetics is in good agreement with the experimental power suggests that the problem might be originating from the kinetic code itself.

3.3. Sensitivity study on the dynamic power calculation

The final step of this study was to carry out a sensitivity analysis on the dynamic simulation. More specifically, the aim of this analysis was to evaluate how the uncertainty of the some of the experimental and simulation input parameters, summarized in Table 3 affect the uncertainty of the dynamic power calculation. Given the current constraints, the sensitivity study was limited to the supercritical transient.

	Parameter	Uncertainty type	Uncertainty (1σ)
Experimental	Helium pressure	Measurement	0.01 bar
	Helium purity	Measurement	0.08%
Simulation	Rescaling factor	Calculation	5 pcm
	Normalization factor	Calculation	2%

Table 3. Uncertainty of the input parameters

Further approximations and biases can be introduced by the test pin modelling choices, specifically in the discretization of the test pin, both in regard to the fissile content (for example in the modelling of the rim zone) and the temperature. At this stage, the discretization of the test pin and in turn, the uncertainties due to the associated approximation made are not considered. Similarly, the uncertainties and biases introduced by nuclear data (such as the kinetic parameters and cross sections) were not considered.

The sensitivity analysis regarding the experimental and simulation input parameters is presented below.

3.3.1. Experimental parameters

The supercritical transient is driven by the pressure difference between the critical core configuration and the final core configuration. Two parameters that influence the pressure difference are the uncertainty on the pressure measurement and the uncertainty on the purity measurement. The former is defined as 0.035% of the nominal pressure and an additional 0.01 bar due to the measurement noise, and the latter has an absolute uncertainty of 0.8% (Clamens, 2018).

The experimental pressure difference is 0.7206 - 0.038 = 0.6825 bar. Taking into account the uncertainty on the initial and final pressure, the uncertainty on the pressure difference (ΔP) is:

$$\Delta P = 0.683\ bar\ \pm 0.020\ bar$$

The helium purity during the commissioning test was 99% with a 0.08% absolute uncertainty. Adapted to the pressure difference, this result in the following:

$$\Delta P_{purity} = (\Delta P * 0.99) \pm 0.11\ bar = 0.676\ bar \pm 0.11\ bar$$

The uncertainty on the helium purity is in the same order of magnitude as the uncertainty on the pressure measurement, so a priori no extra calculations are needed, since the conclusions can be drawn from the results of the pressure calculations.

To conclude, the different cases considered to calculate the relative difference on the power calculation due to the uncertainty on the helium pressure are summarized in Table 4. The consistency of the result is evaluated by comparing the results given by PALANTIR and the power computed using the kinetic TRIPOLI-4®.

	Initial pressure [bar]	Final pressure [bar]	Pressure difference [bar]
Nominal values	0.7206	0.038	0.683
Calculation #1 dPMin	0.7206	0.058	0.663
Calculation #2 dPMax	0.7206	0.018	0.703

Table 4. Test cases considered for the uncertainty calculation on the dynamic power

The results are shown in Figure 39. A fluctuation can be observed in the kinetic scores and the calculated core power, on the account of the low convergence of the dynamic calculation. Thus, in order to have a representative value on the uncertainty on the power calculation, instead of looking at the relative difference on the final power, an average relative difference is considered. This average is calculated by computing the relative difference between the power calculated for the different cases for each time step starting from the time of the last geometry change until the end of the transient and averaging it. This methodology is applied throughout this chapter.

As it can be observed, the uncertainty of the pressure measurement, which represents 3% of the total pressure difference, has a significant impact on the power calculation. In case of the dynamic calculation, 3% of pressure variation leads to a ~19% variation in the power, while in the case of the PALANTIR calculation, the power varies by 9% at 1σ. The main difference between the two calculation scheme is that the dynamic scheme does not account for the different feedbacks (in this particular test case). The impact of the different feedbacks on the

power calculation was assessed with the help of the point kinetics solver and the reactivity curve given by PALANTIR.

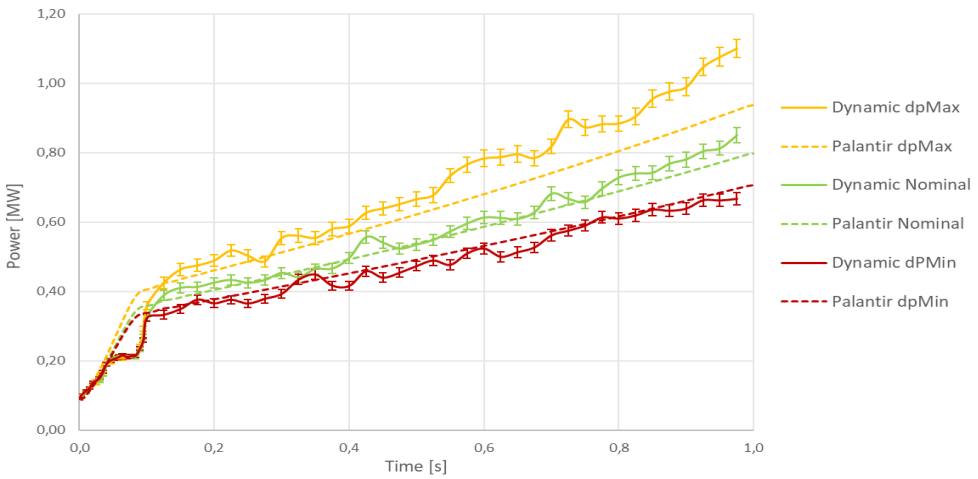


Figure 39. Power evolution for various pressure differences. Results obtained with kinetic TRIPOLI-4® and PALANTIR

PALANTIR provides the decomposition of the total reactivity insertion into the external, Doppler, moderator and expansion reactivity. The external reactivity accounts for the reactivity introduced with the helium depressurization. Thus, it corresponds to the total reactivity insertion modelled in the dynamic calculation. The Doppler feedback, which is the most important reactivity feedback, amounts to 10 pcm negative reactivity insertion during the depressurization. On the other hand, the reactivity feedback due to the moderator temperature increase and the fuel expansion is negligible in this case, corresponding to less than 1 pcm by the end of the transient.

The impact of the feedbacks is demonstrated in Figure 40, detailed for the dpMax case, which is the most sensitive to it. This figure presents the power evolution calculated with the point kinetics solver where the reactivity injection was defined based on the reactivity injection calculated by PALANTIR. Two cases are presented: one where the reactivity injection equals the total reactivity injection (accounting for the depressurization and the different feedbacks) and when it equals the external reactivity (i.e. no feedbacks). It can be observed that the former case corresponds to the power evolution given by PALANTIR (as the code uses point kinetics as well when calculating the power). The latter case, which corresponds to the reactivity injection modelled in the dynamic scheme, indicates that not taking into account the different feedbacks overestimates the power by 5%, which explains the discrepancy in the results shown in Figure 39, and it underlines the importance of accounting for the Doppler feedback in the dynamic power calculation.

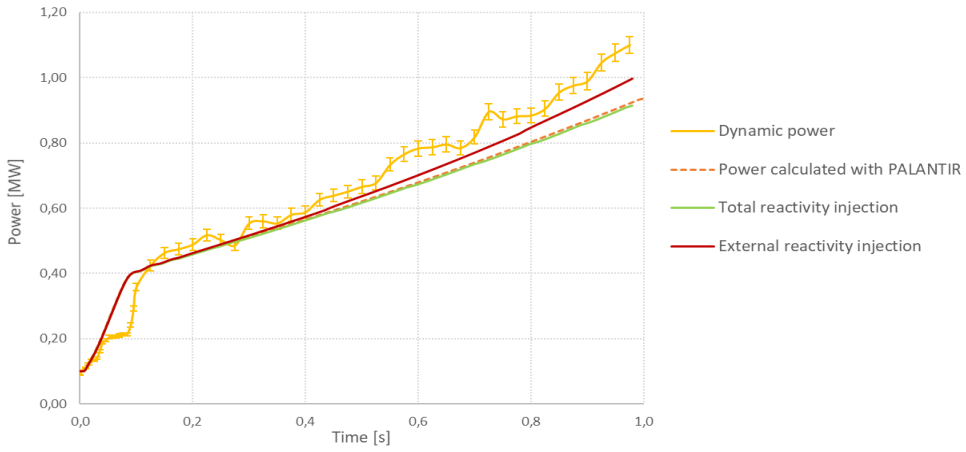


Figure 40. Impact of the reactivity feedbacks on the power evolution

Finally, accounting for the helium purity corresponds to a decrease of the nominal pressure difference of 1%. As illustrated in Figure 41, this has no significant impact on the power calculation and it can be neglected.

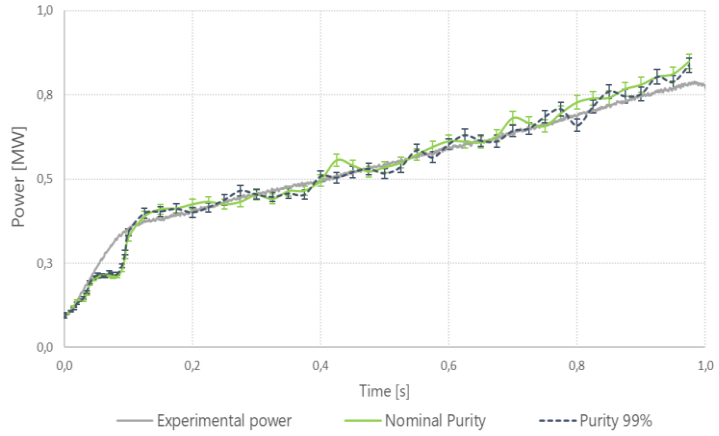


Figure 41. Sensitivity of the power calculation to the helium purity

3.3.2. Simulation parameters

Two sources of uncertainty are considered in the case of the dynamic calculations: the rescaling factor, which corresponds to the multiplication factor of the critical core configuration and the normalization factor. The normalization factor is calculated from the core power and total fission reaction rates in the critical core configuration and it is applied to every dynamic score during the post-processing phase.

Rescaling factor

The statistical uncertainty on the effective multiplication factor, computed by running a criticality calculation for the critical core configuration, is 5 pcm. The impact of this uncertainty on the kinetic calculation is evaluated by running two additional calculations where the given rescaling factor is either the upper or the lower limit of the original factor. The results of the two calculations are displayed in Figure 42. The 10 pcm difference in the rescaling factor results on average in 11% difference in the calculated power, while the statistical uncertainty on the power calculation is ~3%, emphasizing that the uncertainty of rescaling factor has a significant impact on the power calculation.

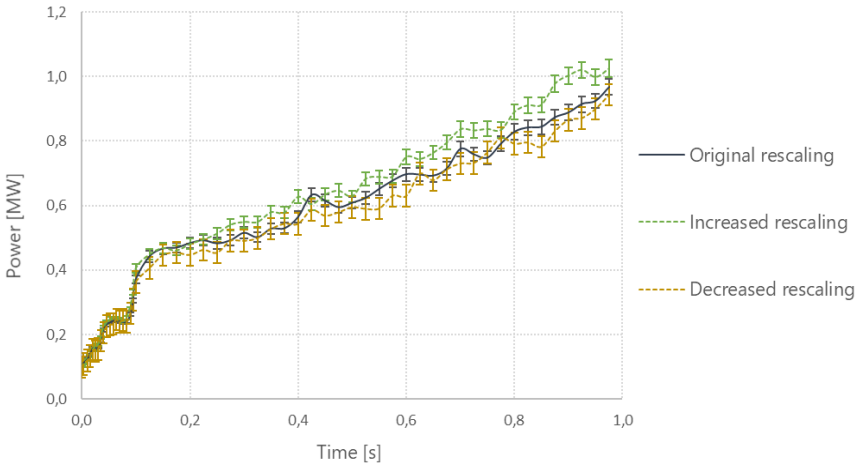


Figure 42. Impact of the rescaling factor on the power calculation

Normalization factor

The primary uncertainty source in the normalization factor is the statistical uncertainty on the total reaction rate, which is in the order of 2%. However, there is another aspect specific to the dynamic calculation to consider when defining the normalization factor that could lead to biased results. It was observed that the kinetic results tend to fluctuate when a stationary condition is simulated. Furthermore, the flux and the reaction rates were underestimated (~3%) early in calculation. This uncertainty should be accounted for by the following way. First, the critical state should be simulated over 10 time steps of 0.1 seconds, following which the depressurization starts. Then in order to capture the order of magnitude of the fluctuations in the dynamic scores, the scores relevant to the steady state should be defined as the average of the scores over those 10 time steps. With this in consideration, the relative uncertainty on the normalization factor is 1.6% at 1σ. Since the normalization factor is applied to all scores, this uncertainty applies to the power calculation as well.

3.4. Summary

This chapter deals with the implementation of the stepwise and dynamic calculation scheme for a supercritical and a prompt-supercritical transient. The depressurization was modelled with a set of consecutive core configurations and the analysis based on the point kinetics solver showed that this modelling scheme is able to correctly represent the reactivity insertion. The implementation of the kinetic module requires the definition of the simulation timesteps and the corresponding importance ratio. During the fast phase, the time steps should be defined based on the characteristic neutron population variation time with the associated importance ratios calculated from equation (2.26). In the slow kinetics phase times steps in the order of a 0.1 s are sufficient and the importance ratio is not needed.

The dynamic simulations showed that with the current modeling choices, in the case of the supercritical transient, the dynamic power is in good agreement with the experimental and PALANTIR results. The discrepancy between the dynamic and experimental power is within the associated uncertainties. However, the prompt supercritical simulations revealed that the kinetic module implemented in TRIPOLI-4® is not yet able to correctly calculate the power evolution in the case of a prompt-supercritical transient.

The analysis of the modelling is supplemented with a sensitivity analysis on the dynamic power calculation, focused on the impact of the uncertainties concerning the helium pressure and the uncertainties due to the simulation parameters. The analysis showed that the power calculation is the most sensitive to the uncertainty on the pressure measurement, a 3% measurement uncertainty leading to 9% discrepancy in the power calculation at 1σ. The uncertainty due to the simulation parameters amounts to 4% at 1σ, and it can be mitigated by decreasing the statistical uncertainty of the preliminary criticality calculation. Overall, considering the statistical, measurement and simulation uncertainties, the uncertainty of the dynamic power calculation increases to 10%.

4. FLUX DISTRIBUTION DURING A TRANSIENT

Even though there are different approaches for estimating the energy deposition, each of them is based on the same physical quantity: the neutron flux obtained with TRIPOLI-4®. Therefore, the neutron flux distribution and variation will be analyzed before addressing the evolution of the integral parameters, such as the coupling factor or the energy deposition.

The first part of this chapter is focused on both the flux evolution during a supercritical transient and on the differences between the results obtained with the static and the dynamic modules of TRIPOLI-4®. The second part deals with the dynamic flux distribution in the case of a prompt supercritical transient, obtained the static version of the code.

4.1. Evolution of the flux during a supercritical transient

An in-depth presentation of the supercritical transient and its modelling in the stepwise and dynamic methodologies is given in Chapter 3. The main parameters, relevant to the following analysis, are summarized below.

A simple depressurization from 0.72 bar was chosen as the supercritical test case. This transient is modeled with 5 consecutive geometries, each described by a pair of helium pressure and fuel temperature. Due to the low amount of reactivity insertion and moderate power increase, there is no significant temperature (fuel or moderator) increase during this transient. In other words, the Doppler feedback is not taken into consideration in this case.

To avoid repetition while presenting the results of the static and dynamic calculation scheme, the flux evolution will be presented primarily through the dynamic results, since this methodology provides the actual time-dependent results. Then, at each step, these dynamic results will be compared with the corresponding static result. This allows for the accounting of the possible discrepancies between the two methodologies and for the assessment of the accuracy of the static calculation when used for a transient simulation.

The radial distribution of the flux will be discussed first, followed by the axial flux distribution and the flux spectrum variation. The aim is not only to look at the overall flux distribution and its variation during the transient, but also to focus on the possible differences, if applicable, between the flux variation in the pressurized water loop and the flux variation at the core level.

4.1.1. Radial flux distribution

Figure 43 presents the radial distribution of the flux in the critical core configuration and the relative variation in the flux following the depressurization. The results are obtained with the dynamic module and the flux is normalized to unity. The radial flux distribution reflects the particularities of the core structure, such as the presence of the hodoscope channel and the pressurized water loop with its associated structures in the center. Since the initial helium pressure (i.e. helium concentration) is low, the impact of the transient assemblies on the flux is minimal. On the other hand, this also means that the control rods have to be inserted down to the mid-core plane, resulting in an important flux decrease around the control rods.

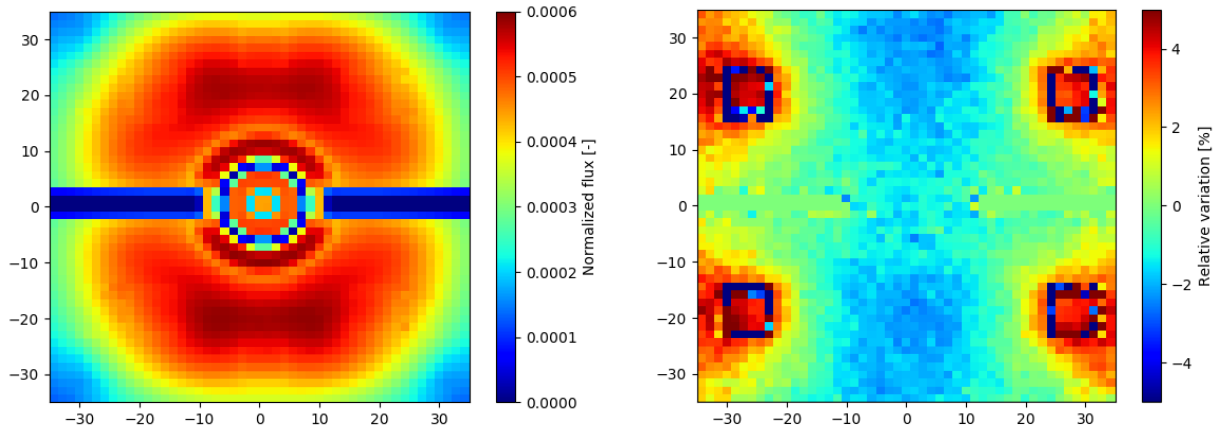


Figure 43. Radial distribution of the flux in the critical core configuration (left) and the relative flux variation at the end of the transient (right). Results obtained with the dynamic module

The null flux in the hodoscope channel and in given structures in the pressurized water loop is due to the choice of the flux estimator. In the presence of voided volumes, such as the pressurized water loop and hodoscope channel it is suggested to use track estimators instead of collision estimators to be able to compute the flux. However, the track estimator is not yet compatible with the development version of the code, and as such, the flux was computed with the collision estimator throughout the calculations presented in the thesis.

The helium depressurization leads to an overall flux increase in the core. However, the flux variation rate is not the same in every location. It is the most important around the transient rods, as shown on the right plot in Figure 43. This results in a higher flux increase in the periphery than in the center, leading to a flatter flux distribution in the final stage of the transient.

Regarding the flux distribution obtained with the static module (shown in Figure 44), the relative difference between the static and dynamic flux is less than 1% for the critical and less than 2% for the final core configuration. However, a systematic flux overestimation can be

observed in the pressurized water loop in the dynamic calculation. Keeping in mind that the statistical uncertainty of the static flux is under 1% and around 2% in the case of the dynamic results (when computed for the radial mesh), the discrepancies observed are within statistical uncertainties.

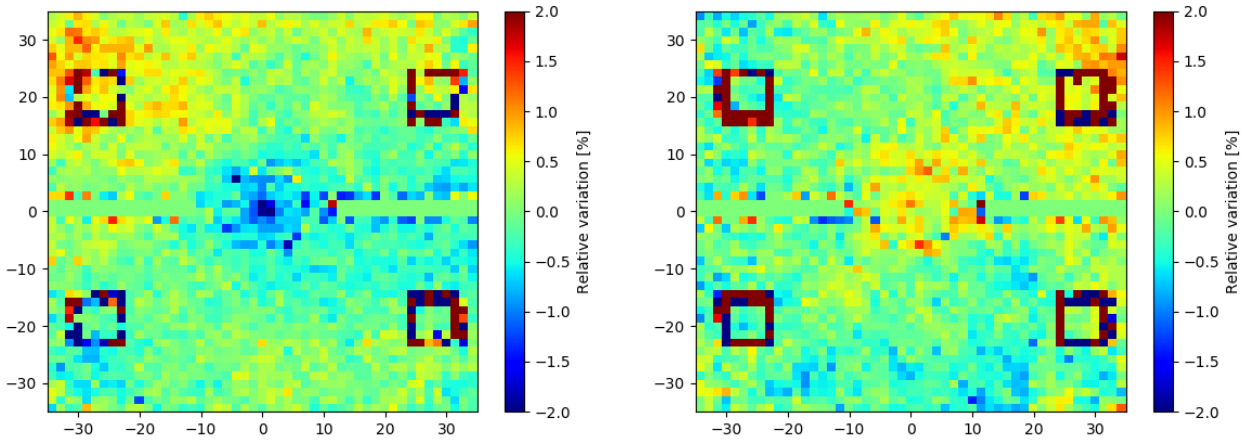


Figure 44. Relative difference between the static and dynamic flux distribution for the critical (left) and final (right) core configuration

The radial distribution of the statistical uncertainties is presented in Figure 45. As expected, the uncertainty is inversely proportional to the flux in a certain volume, and, as such, the highest uncertainties can be found in the transient rods, water loop and hodoscope. On average, the uncertainty of the flux in the transient rods is one order of magnitude higher than the uncertainty in the nominal fuel rods. The distribution of the uncertainties is similar between the static and dynamic calculation, the dynamic uncertainties however are significantly higher than the static uncertainties. On average, the latter reach 0.06%, while the dynamic uncertainties are around 1.8%.

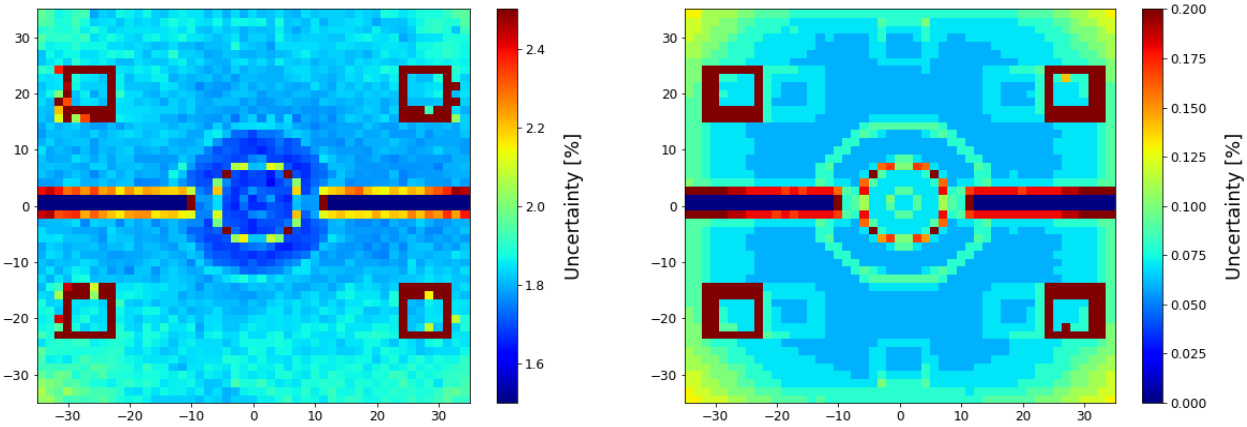


Figure 45. Statistical uncertainties on the flux in the critical core configuration for the dynamic (left) and static (right) calculation.

Even though the flux distribution itself is not impacted by the simulation mode, the total flux computed in the dynamic mode is 3% lower for the initial critical state than the flux computed in steady-state, with the statistical convergence on the total flux being lower than 0.5% on these scores in both modes. The only difference between the calculations is the simulation mode (static or dynamic). The reason for this discrepancy is not yet clear and is currently being investigated.

Figure 47 shows the radial distribution of the fast and thermal flux for the critical core configuration, obtained with the dynamic module. The fast flux is peaked towards the center of the driver core, while the thermal flux reaches its maximum in the center of the core, due to the moderation of the fast flux in both the water loop and in the surroundings of the pressurized water loop structure. The depressurization has the similar impact on both the fast and thermal flux distribution, as displayed in Figure 46. The increase around the transient rod (this increase is slightly higher for thermal neutrons), and the relative flux increase is more important in the periphery than in the center of the core.

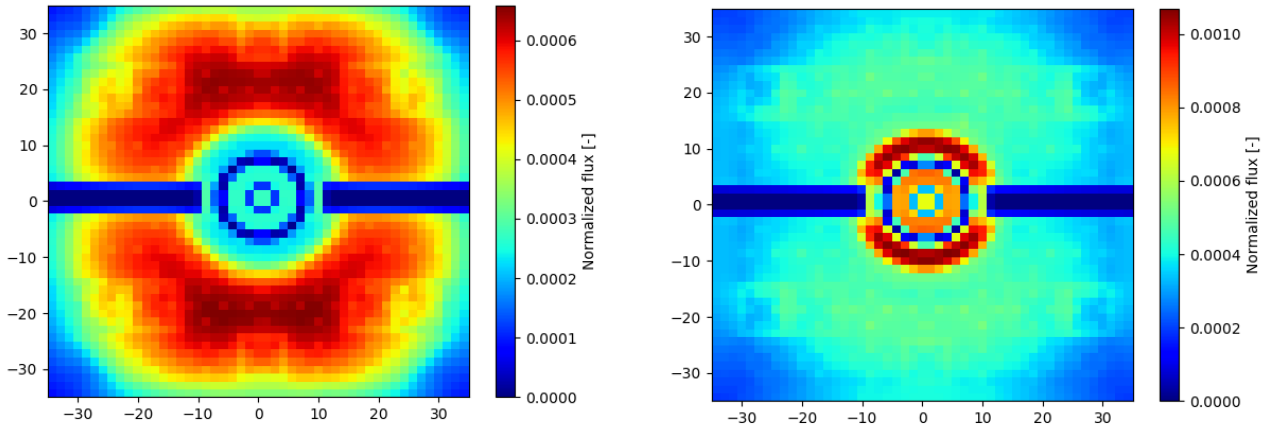


Figure 47. Radial distribution of the fast (left) and thermal (right) flux in the critical core configuration. Results obtained with the dynamic module

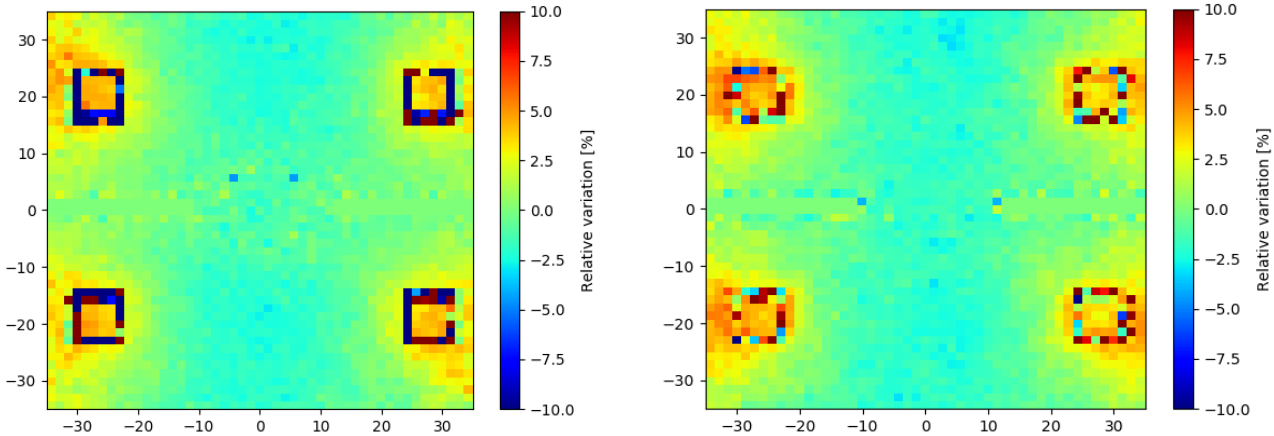


Figure 46. Relative variation in the fast (right) and thermal (left) flux between the initial and final core configuration

Similar to the total flux variation, there is a good agreement in the fast and thermal flux distribution between the static and dynamic modules, as presented in Figure 48 for the critical core configuration and in Figure 49 for the final core configuration. The maximum relative difference is on average 2% for both the critical and final core configuration, which is within the statistical uncertainty of the scores. These results also indicate that the systematic flux overestimation in the pressurized water loop is due to the overestimation of the fast flux (the fast flux for the critical configuration is 2 to 4% lower with the dynamic calculation than with the static one).

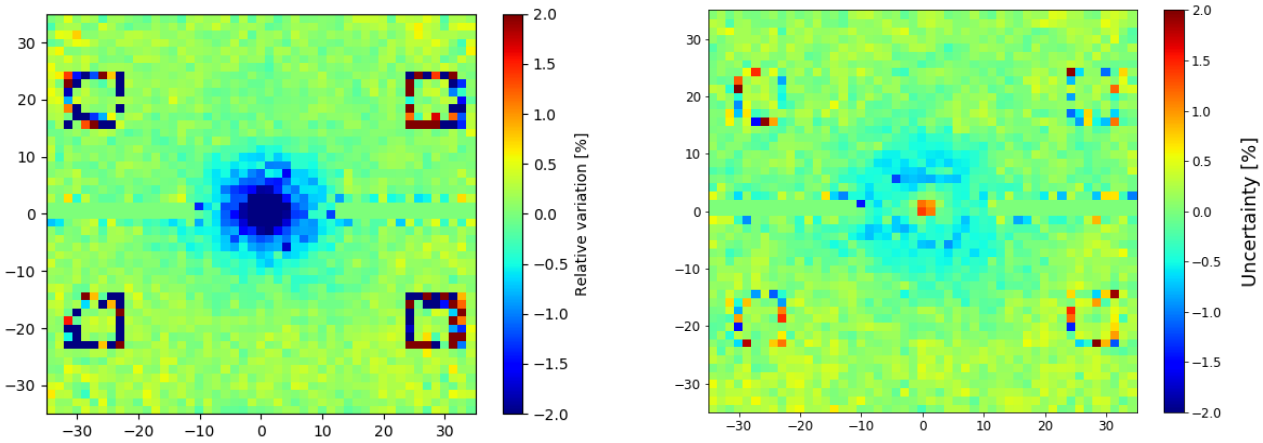


Figure 48. Relative difference between the static and dynamic flux distribution for the critical core configuration for the fast (right) and thermal (left) flux

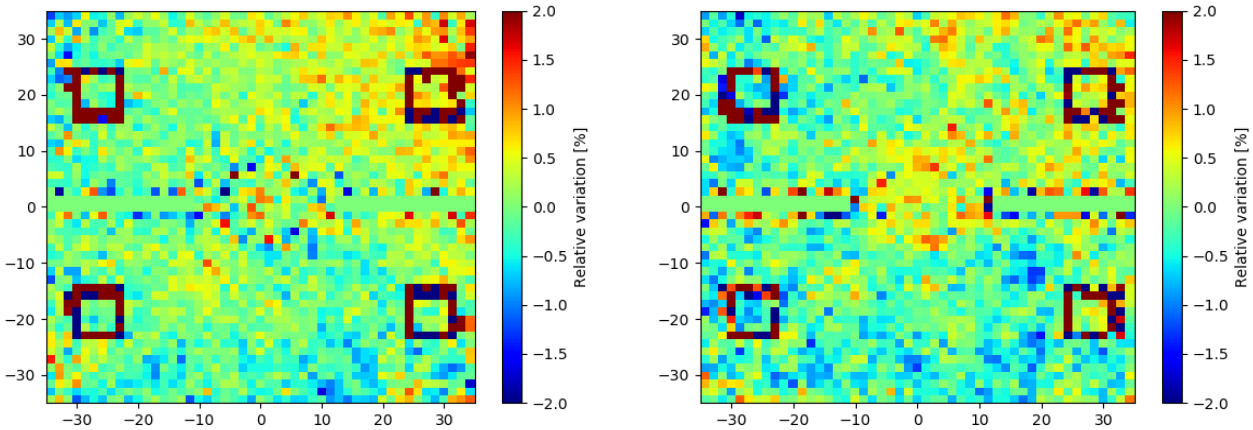


Figure 49. Relative difference between the static and dynamic flux distribution for the final core configuration for the fast (right) and thermal (left) flux

4.1.2. Axial flux distribution

Given the characteristics of this transient, namely the axially homogeneous helium depressurization and the fact that the control rod position is fixed during the transient, the axial flux distribution does not meaningfully change during the transient. Nevertheless, it is more interesting to verify whether there is a difference in the axial distribution between the test pin and different types of assemblies.

Figure 50 presents the axial distribution of the flux, obtained with the dynamic module, in the test pin and in different types of adjacent fuel assemblies: a transient assembly, a control rod assembly and a 7x7 assembly. The flux is scored on 4-cm segments along the test pin, and over each chosen assembly. As expected, the axial flux has a cosine distribution with a lower flux in the top of the core, due to the control rods being inserted 39 cm, the bottom of which corresponds to a height of 1 cm height on the z-axis in Figure 50. The erratic behavior of the uncertainties in the case of the transient assembly is due to the presence helium in the transient rods, which result in a lower flux and significantly higher uncertainties than the average uncertainty in nominal fuel rods (see Figure 45).

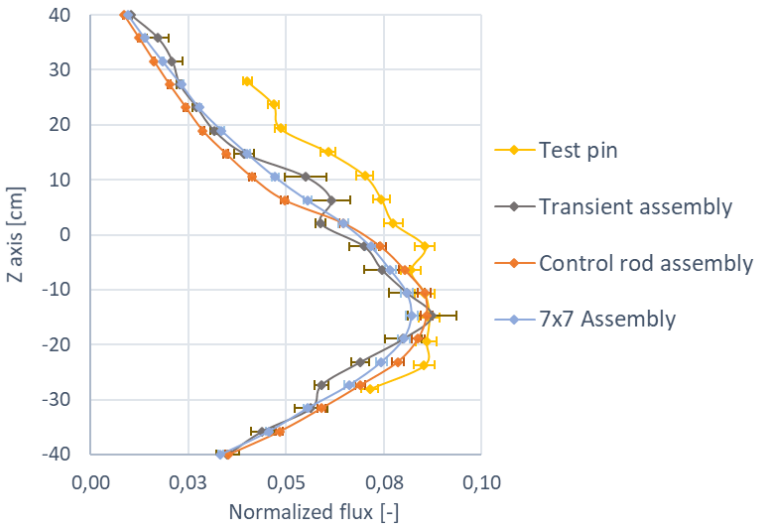


Figure 50. Axial flux distribution in the test pin and in chosen assemblies in the critical core configuration. Computed with the dynamic module and normalized to 1

As presented in Figure 51, there is good agreement between the axial flux distribution calculated by the static and dynamic modules. The small differences in the case of the test pin and transient assembly can be attributed to the statistical uncertainty of the dynamic scores (3 to 5%).

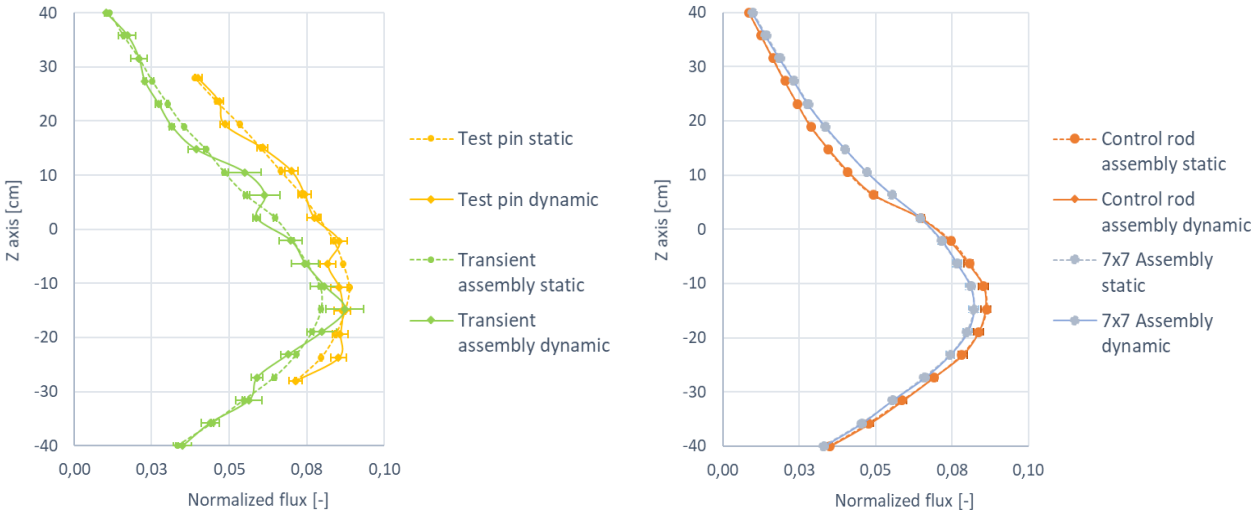


Figure 51. Axial flux distribution computed with the static and dynamic module in the critical core configuration

4.1.3. Spectrum variation

The flux spectrum is another significant parameter. More specifically the difference in the spectrum in the test pin and in the core as well any variation in the spectrum resulting from the depressurization of the transient rods. A difference in the spectrum is important because the probability of fission, i.e. macroscopic fission rate, is energy dependent and it differs for the different fissile isotopes. Thus, a difference in the flux spectrum could ultimately result in a different energy deposition rate.

Figure 52 presents the flux spectrum, discretized into 99 energy groups, in the test pin and the core for the critical core configuration, as obtained with the dynamic module. The flux is computed for the critical core configurations and are normalized to unity. These results emphasize that the spectrum in the driver core is harder than in both the central water loop and in the test pin. The flux spectrum computed with the static and dynamic module is in good agreement, the relative difference being in the order of the statistical uncertainty.

Discretizing the neutron spectrum into three groups (thermal: <0.4 eV, intermediate: 0.4 eV to 1 MeV, and fast flux: 1 to 20 MeV) the thermal flux represents 22%, the intermediate flux 46% and the fast flux 32% of the total flux in the pin. In the core on the other hand, the thermal flux represents 22%, the intermediate flux 63% and the fast flux only 15% of the total flux. This distribution does not change with the depressurization, the relative difference between the final and critical distribution is under 0.5% for both the core and the test pin.

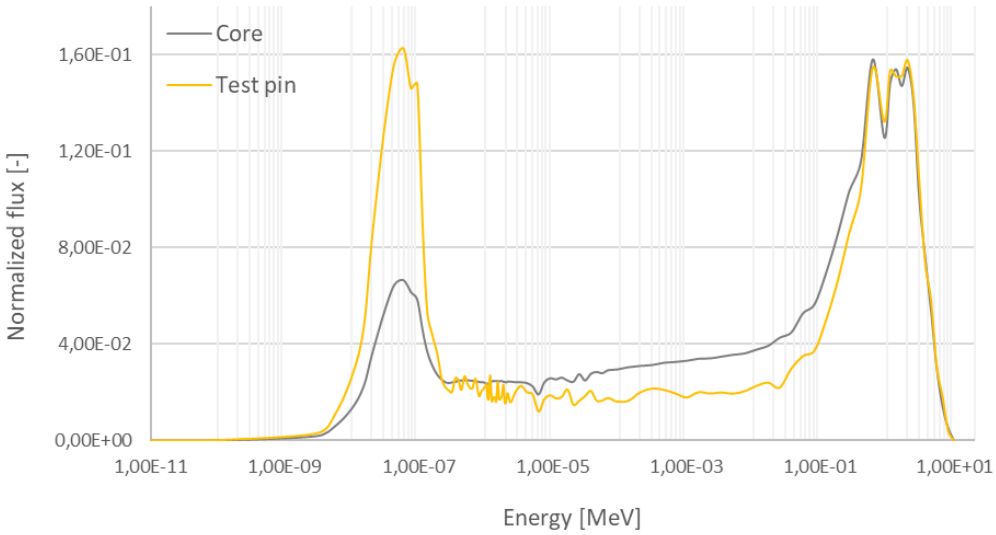


Figure 52. Neutron flux spectrum per lethargy unit in the core and test pin in the critical core configuration, obtained with the dynamic module

4.2. Evolution of the flux during a prompt supercritical transient

The dynamic module of the TRIPOLI-4® code is not yet capable of correctly simulating the power increase in the case of a prompt supercritical transient. Accordingly, the simulation of a prompt supercritical transient is limited to static calculations.

In order to be able to capture stronger feedbacks than the 1.4 bar depressurization provides, a new transient was chosen as a prompt-supercritical test case: a simple depressurization from 11.5 with a fresh UO_2 test pin. The transient is represented by 7 consecutive geometries, defined similarly to the previous cases. The maximum power is 21 GW and the power surge is terminated by the Doppler feedback and control rod drop (not modelled in these calculations). The evolution of the main parameters and the chosen geometries are depicted in Figure 53.

The radial distribution will be presented first, followed by the axial distribution and the flux spectrum variation. In each case, the flux evolution is considered at both the core and test pin levels, focusing on possible differences between the flux behavior in the core and pressurized water loop.

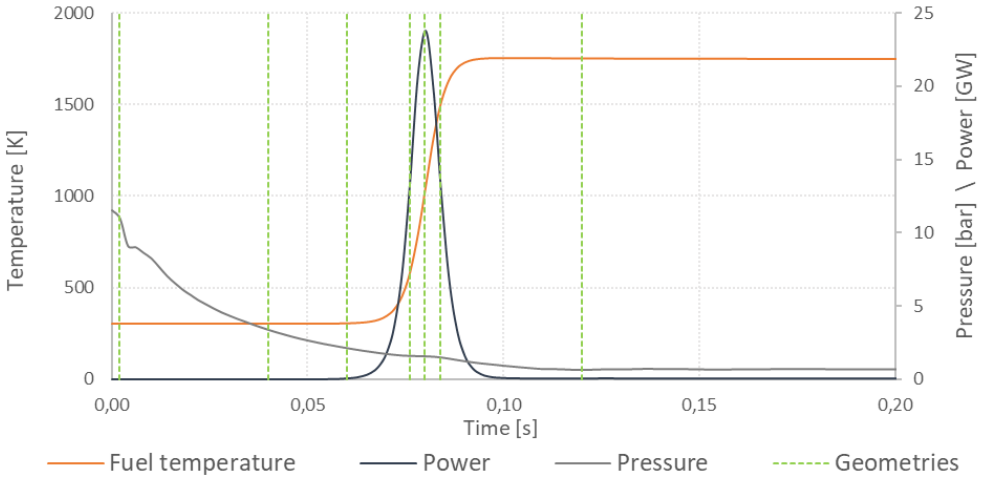


Figure 53. Evolution of the main parameters of the prompt-supercritical transient. Results obtained with PALANTIR

4.2.1. Radial flux distribution

Figure 54 presents the radial distribution of the flux in the critical core configuration and the relative variation in the flux following the depressurization. The results are obtained with the static module and the flux is normalized to unity.

With a high initial helium pressure, the flux is significantly lower around the transient rods, as it can be observed in the periphery of the core. Consequently, the control rod insertion depth is limited to 26 cm, thus having less impact on the radial flux shape. Following the helium depressurization there is a significant flux increase around the transient assemblies as shown on the right in Figure 54.

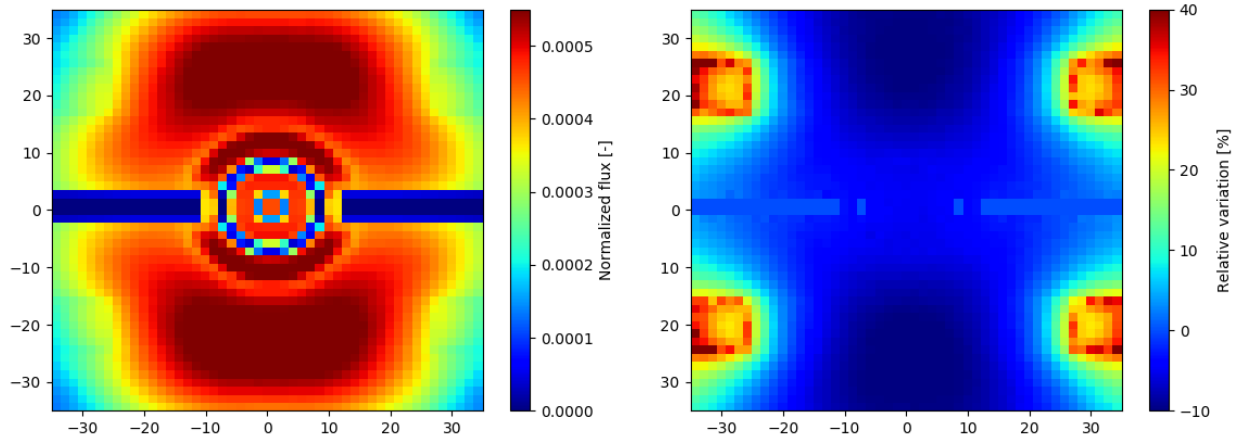


Figure 54. Radial flux distribution for the critical core configuration (left) and the relative variation in the flux following the depressurization (right). The neutron flux is normalized to 1

Due to core symmetry and the position of the transient assemblies, this also means that the original peaked flux is flatter at the end of the transient. With the relative flux distribution variation being normalized to unity, this translates to an apparent flux decrease in the center, which actually indicates that the flux in the center is increasing at a lower rate than around the periphery of the core. The relative distributions of the thermal and fast fluxes are presented in Figure 55 and in Figure 56, respectively. The thermal flux peaks in the water loop surrounding the pressurized water loop structure, as a result of the thermalization of the fast neutrons in the moderator. Meanwhile, the fast flux is peaks in the center of the driver core, proportional to the amount of fissile material.

The variation induced in the thermal and fast flux distribution due to the depressurization is the same in both cases: the flux significantly increases around the transient assemblies. This increase is somewhat more important in the case of the thermal flux (40%, as opposed to 25% for the fast flux), since the helium-3 is a thermal neutron absorber.

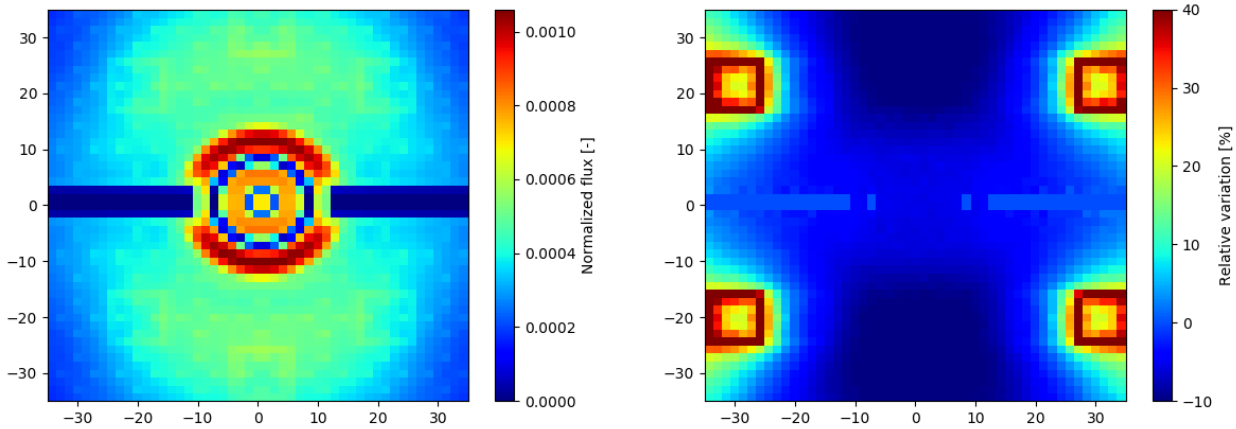


Figure 55. Relative distribution of the thermal flux for the critical core and the relative variation of the thermal flux following the depressurization. The neutron flux is normalized to 1

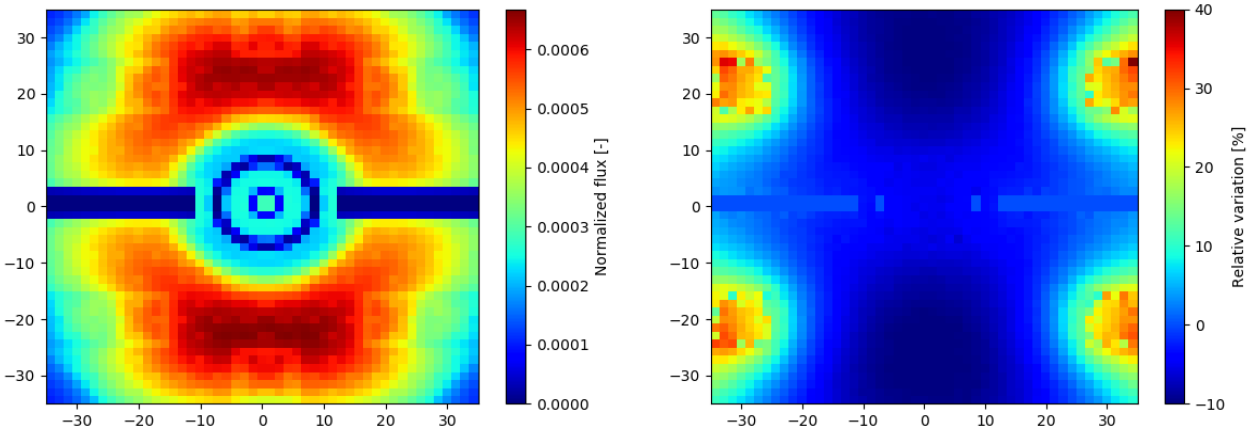


Figure 56. Relative distribution of the fast flux for the critical core and the relative variation of the fast flux following the depressurization. The neutron flux is normalized to 1

Figure 57 presents the individual impact of both the Doppler feedback and helium depressurization on the radial flux distribution. The helium impact can be captured by computing the flux variation between the first and fourth geometry. Between these states the helium pressure decreases from 11.5 bar to 3.71 bar, without any fuel temperature variation. Similarly, the impact of the Doppler feedback can be presented by comparing the flux distribution between the core configurations referred to as fifth and sixth geometry, where the temperature increases by 700°C while the helium pressure decreases by 0.2 bar. The overall impact of the latter can be considered negligible.

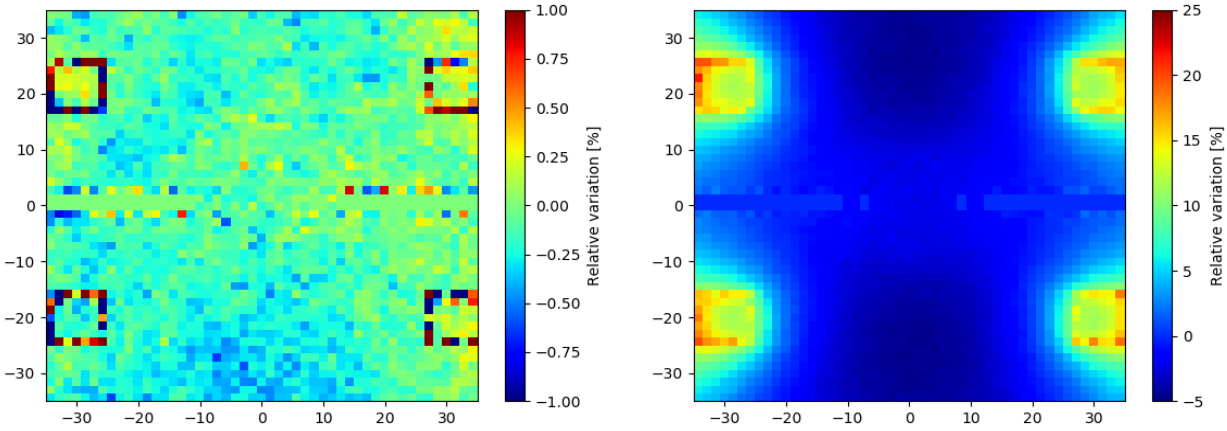


Figure 57. Relative variation in the flux due to the Doppler feedback (left) and the helium depressurization (right)

The helium depressurization results in a significant flux increase (in the order of 10%) in the periphery. On the other hand, given that in the current modelling all of the fuel pins in the core have the same temperature and temperature evolution, the Doppler feedback does not induce any variations in the flux distribution.

The impact of this modelling choice on the flux distribution is assessed by comparing the radial flux distribution between the final core configuration with a discretized and a non-discretized assembly-wise temperature. Due to the symmetrical aspect of the core, a quarter-core representation is adapted in PALANTIR. The assembly-wise temperatures corresponding to the 11 assemblies are shown in Figure 58. The non-discretized core temperature is defined as the average of the assembly-wise temperatures calculated with PALANTIR, and is 1840 K in this case.

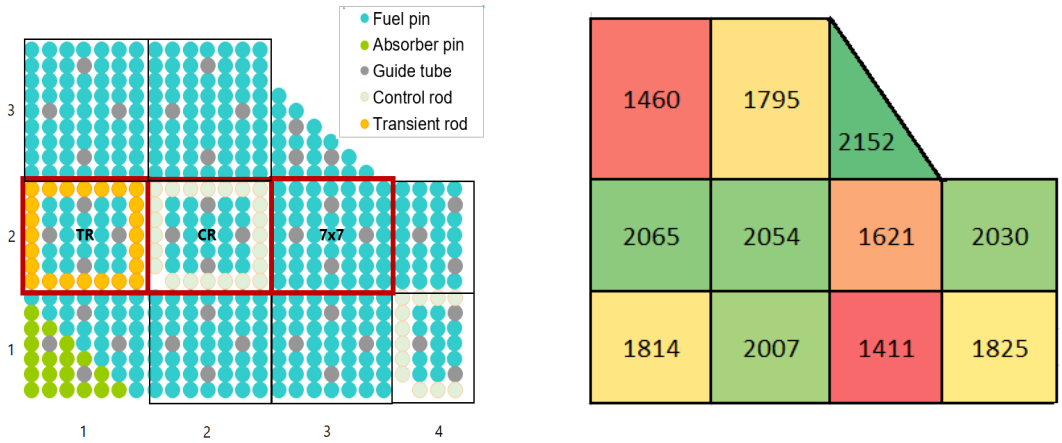


Figure 58. Schematic view of the quarter of the core (left), and corresponding assembly-wise temperatures in K (right)

As illustrated in Figure 59, the relative difference between the flux distribution between the discretized and non-discretized case is lower than 1%, meaning that the modelling approximation does not significantly affect the flux distribution. The impact of the relatively high statistical uncertainty on the flux in the transient rods can also be observed here. Consequently, the previously observed variations in the radial flux distribution (Figure 54) can be almost entirely attributed to the helium depressurization.

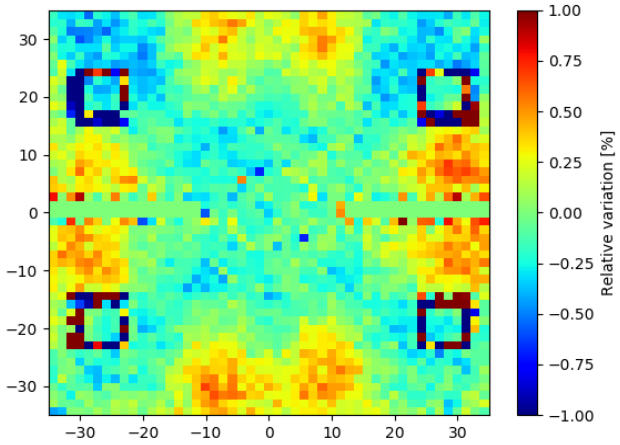


Figure 59. Relative variation in the flux between the discretized and non-discretized core temperatures

4.2.2. Axial flux distribution

Contrary to the radial flux distribution, the axial flux distribution does not vary during this transient. The parameters that could induce variation in the initial axial flux distribution are the control rod position, the helium depressurization and the Doppler feedback. The control rod positions are not changed during the transient, the Doppler feedback is homogeneous over the core (fuel temperature is not discretized) and the helium depressurization, although radially localized, is axially homogeneous. As such, the axial flux distribution does not change during a transient, and the relative variation is under 1%.

Figure 60 presents the axial distribution of the flux in the test pin and in different types of adjacent fuel assemblies: a transient assembly, a control rod assembly and a nominal 7x7 assembly. The axial flux has a cosine distribution, with a lower flux in the top of the core because of the control rod presence (the control rods are inserted 26 cm from the top in this core configuration).

It is interesting to note that the impact of the control rod is less important on the transient assembly than on the nominal assembly, even though both of the assemblies are located right next to control rod assembly. In fact, the helium-3, being thermal neutron absorber, has a shadowing effect on the control rods, which becomes considerable in this case due to the increased helium amount present in the initial core configuration. Following the helium depressurization, the flux distribution in the transient assembly approaches the flux distribution in the nominal assembly, as shown on the right figure.

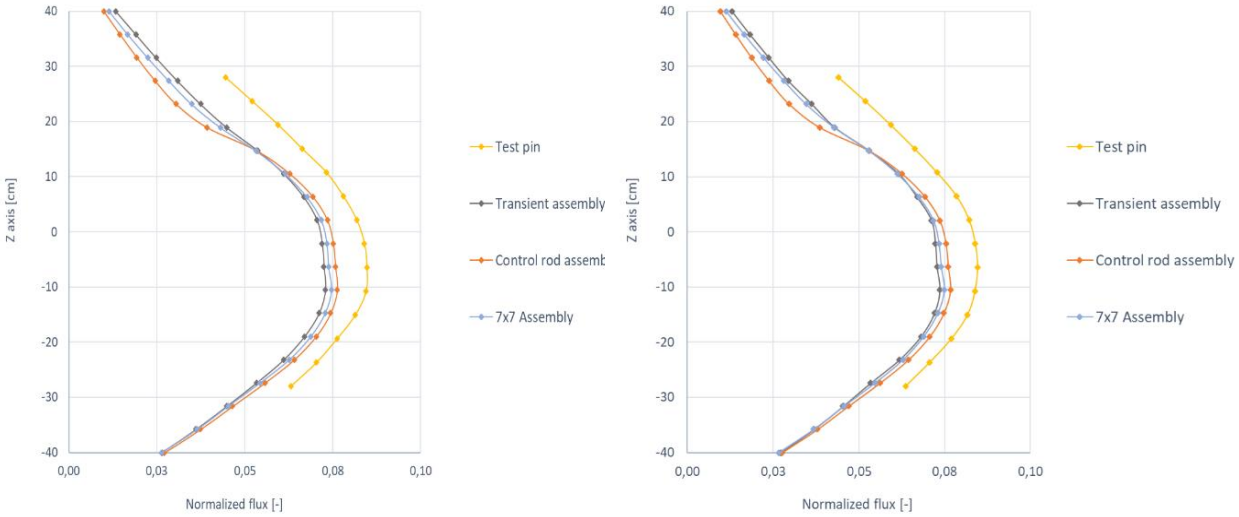


Figure 60. Axial flux distribution in the test pin and several fuel assemblies for the critical core configuration (left) and for the final core configuration (right). Flux normalized to 1

4.2.3. Spectrum variation

The difference in the spectrum between the core and the test pin can be observed in Figure 61, which presents the flux per lethargy unit discretized into 99 energy groups and normalized to 1 in the test pin and the core for the critical configuration. As the test pin is located in the center of the core and surrounded by the water loop, the relative fraction of thermal flux is significantly higher than in the core. The thermal flux (<0.4 eV) represents 23%, the intermediate flux (0.4 eV to 1 MeV) 46% and the fast flux (1 to 20 MeV) 31% of the total flux in the test pin. Concerning the neutron flux spectrum in the driver core, the thermal flux represents 22%, the intermediate flux 63% and finally the fast flux 15% of the total flux. The relative difference between the final and initial flux distribution is under 0.5%.

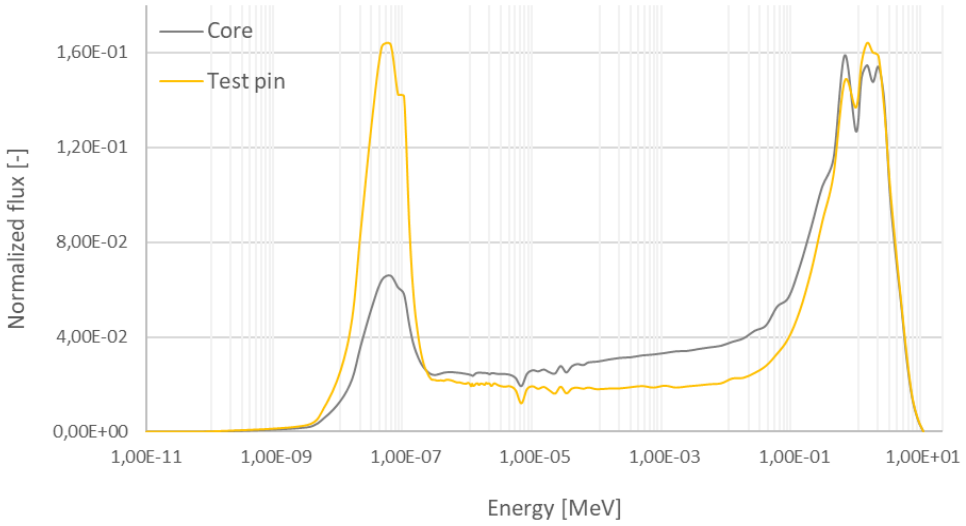


Figure 61. Neutron flux spectrum per lethargy unit in the test pin and the core in the critical core configuration. Results obtained with the static module and normalized to 1

4.3. Summary

Both the dynamic and the static methodologies are able to correctly reproduce the flux shape at different stages of the transient. However, the dynamic module seems to underestimate the absolute flux by 3%. The helium depressurization is the most impactful factor on the flux distribution: radially the flux increases significantly around the transient rods while the axial flux in the transient rods approaches the axial distribution of the nominal fuel assemblies as the depressurization progresses. Finally, it can be observed that the spectrum of the core is harder than the spectrum of water loop and also that the flux distribution does not change during the depressurization.

The impact of the flux shape and spectrum on the integral parameters and their variation is the subject of the following chapter.

5. ENERGY DEPOSITION INTO THE TEST PIN DURING THE TRANSIENT

The main objective of the thesis is to define a calculation methodology to estimate the energy deposition into the test pin during a transient in the CABRI reactor. However, it is not only the absolute value of the energy deposition that it is of interest, but also its evolution throughout the transient. The latter holds information regarding the different parameters that influence this process and also provides information regarding another important aspect, specific to this reactor: the coupling between the driver core and the test pin. The coupling factor is an important operational parameter. Defined as the ratio between the core and test pin power (equivalent to the ratio of the energy deposited in the core and in the test pin, it is measured in steady-state operation and assumed to be constant. Ultimately, it is used to determine the energy deposition into the test pin during the transient.

The first part of this chapter deals with the energy deposition calculation in the case of supercritical and prompt-supercritical transients. This section includes the comparison of the results obtained with static and dynamic calculations, a discussion about the different parameters influencing the energy deposition and an analysis of the impact of the calculation scheme used for the energy calculation. The second part is dedicated to the analysis of the coupling between the driver core and test pin. The aim of this part is to propose a new calculation methodology for the coupling factor that takes into consideration the nuclear heating and the variations between the energy deposition rate in the core and test pin during the transient.

5.1. Energy deposition into the test pin

5.1.1. Energy deposition estimated from fission energies

As presented in Chapter 2, the energy deposited in the test pin can be estimated from the fission reaction rates and the corresponding energy release. The two test cases considered are the depressurization from 0.72 bar, resulting in a supercritical transient, and the depressurization from 11.5 bar, leading to a prompt-supercritical transient. The next two sections deal with the results concerning the energy deposition into the test pin in the case of the two transients. The parameters of interest are the final energy deposition into the test pin and the evolution of the energy deposition rate, which refers to the energy deposition

normalized to the energy deposited in the first step. A comparison of the deposition rate in the core and test pin can be used to emphasize the differences between the energy deposition mechanism in the core and test pin.

5.1.1.1. Supercritical transient

Figure 62 recalls the main characteristics of the supercritical transient, such as the pressure and power evolution, the fuel temperature and the chosen geometries (i.e. pressure and temperature). A fresh UO_2 pin is considered as the test pin, identical in composition to the fuel pins in the core.

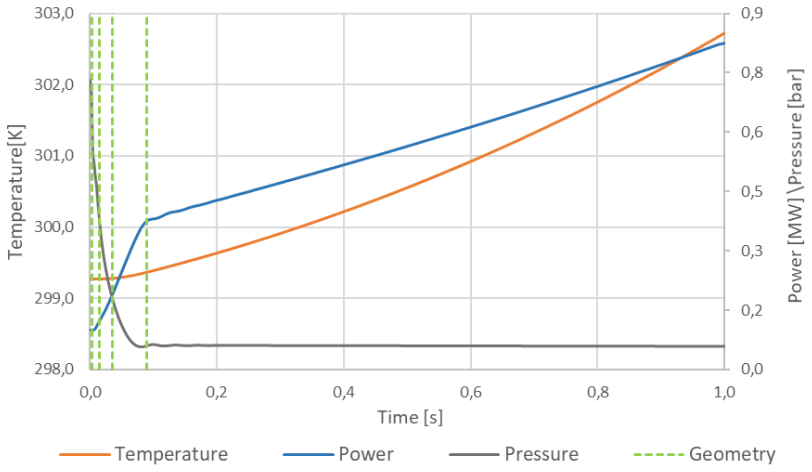


Figure 62. Main parameters of the supercritical transient. Results obtained with the PALANTIR code. Vertical green lines represent the chosen geometries

The energy deposition is calculated from fission rates and fission energies, as described in Chapter 2, and the results concerning the energy deposition into the test pin are presented in Figure 63. It includes the stepwise energy deposition, which refers to the time-dependent energy deposition obtained by linear interpolation between the instantaneous values, and the dynamic energy deposition, obtained with the dynamic module.

The main observation is that the dynamic calculation slightly underestimates the results of the stepwise calculation: averaged over the transient, the energy deposition into the test pin is 4% lower when calculated with the dynamic code. The statistical uncertainty on the power calculation is 2% in the case of the dynamic and 0.4% in the case of the static calculation at 1σ. This was also observed in the case of the flux analysis. This discrepancy is consistent with the 3% discrepancy observed between the static and dynamic flux. The latter can be found in the reaction rates of each isotope as well, suggesting a systematic error that should be accounted for.

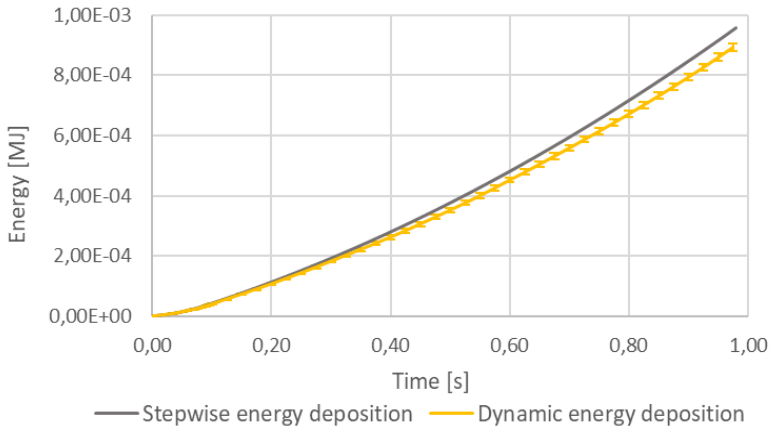


Figure 63. Energy deposition into the test pin, calculated with the static and dynamic module

Another important piece of information that can be obtained from the energy calculation is the energy deposition rate throughout the transient. More specifically, the differences between the energy deposition rate in the core and the test pin. With E_n being the energy deposited in the n-th time step (dt_n) and E_0 the energy deposited in the first time step (dt_0), the energy deposition rate in the n-th time step is calculated as follows:

$$E_{rate,n} = \frac{E_n/dt_n}{E_0/dt_0} \tag{5.1}$$

Figure 64 depicts the energy deposition rate in the core and in the test pin, computed using the results of the static calculations and the ratio of the two deposition rates. It can be observed, that as the transient progresses the energy deposition in the core is more important than the energy deposition into the test pin. By the end of the transient, the energy deposition rate is close to 2% higher in the core than in the test pin.

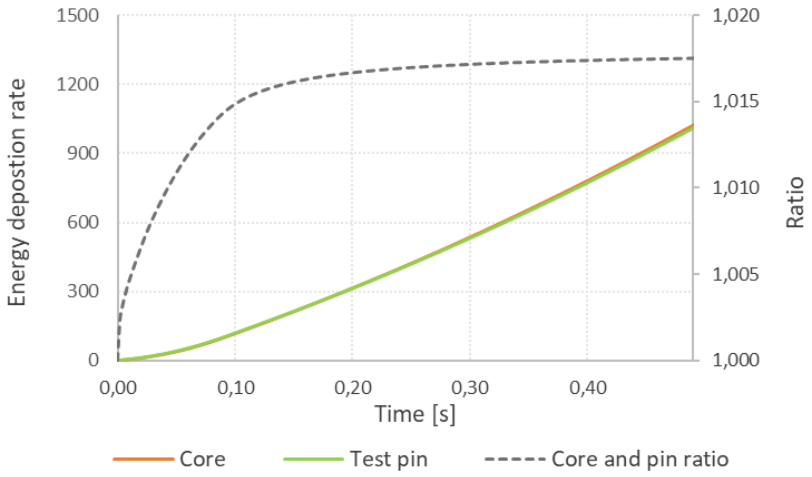


Figure 64. Energy deposition rate in the core and in the test pin during the transient. Results obtained with the static module

The same parameters are plotted in Figure 65 for the dynamic calculation. The results suggest a constant energy deposition rate between the core and the test pin. This is not surprising since the statistical error on the energy deposition and deposition rate calculation is on the same order of magnitude as the relative difference suggested by the stepwise results. Thus, no conclusive observations can be drawn from the dynamic results concerning the energy deposition rate in this low-energy transient. Instead, an in-depth analysis of the energy deposition and deposition rate, including a sensitivity studies concerning the modelling choices, is provided through the example of the prompt supercritical transient.

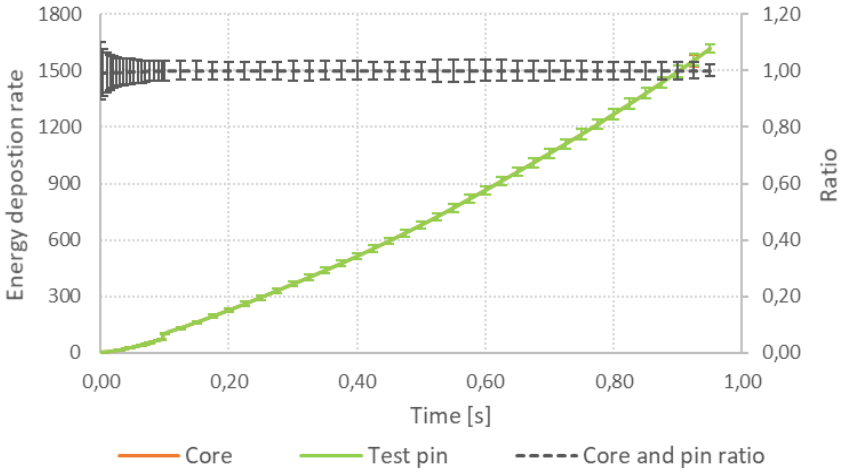


Figure 65. Energy deposition rate in the core and in the test pin during the transient. Results obtained with the dynamic module

5.1.1.2. Prompt supercritical transient

The energy deposited during the prompt supercritical transient is calculated similarly to the supercritical case. The evolution of the main parameters of the prompt-supercritical test case is presented in Figure 66, alongside of the chosen core configurations. For each of these configurations an instantaneous power is calculated for the driver core and for the test pin respectively. Once the instantaneous power is normalized to the corresponding core power, (computed with PALANTIR), the time-dependent power is obtained by linear interpolation between two consecutives values.

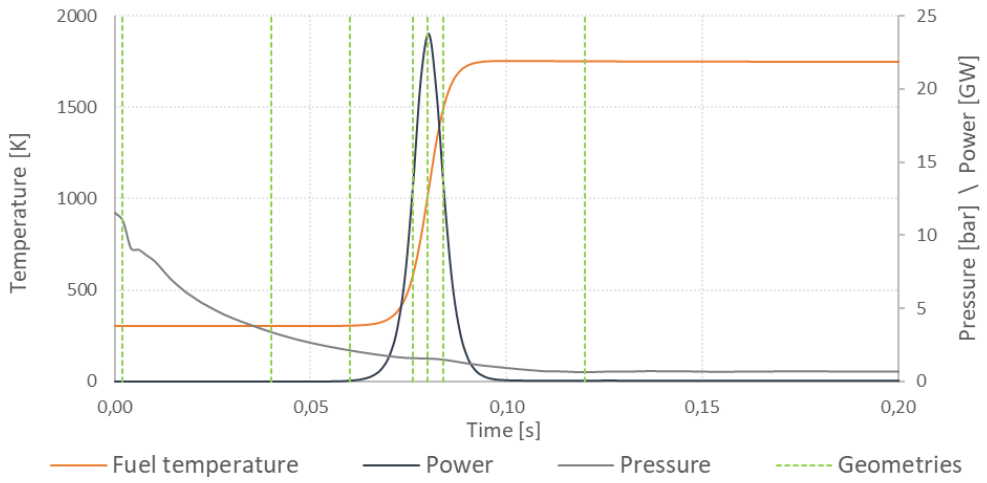


Figure 66. Evolution of the main parameters of the prompt-supercritical transient. Results obtained with PALANTIR

Integrating the core power along the transient gives the energy deposition, summarized in Figure 67. For 345 MJ deposited in the core, 0.62 MJ is deposited in the test pin and the most significant energy deposition happens during the power pulse.

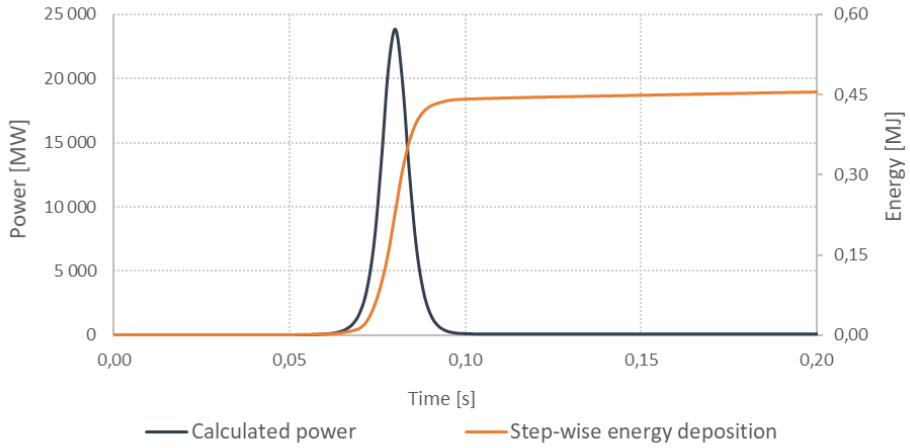


Figure 67. Test pin power and energy deposition during the prompt-supercritical transient

When looking at the energy deposition rate in the core and in the test pin, shown in Figure 68, two points can be made: the energy deposition rate in the core is higher than in the test pin and this difference is evolving during the transient. The relative difference between the energy deposition rate in the core and in the test pin increases to 4% during the transient, implying that as the transient progresses, there is relatively more energy deposited in the core than in the test pin.

Furthermore, it can also be noticed that changes in the relative difference correspond to the changes in the geometry, and the increase is not linear. This suggests that the energy deposition rate is influenced by the core parameters. The next section is dedicated to an in-depth analysis on the possible factors that influence the energy deposition and the deposition rate during the transient.

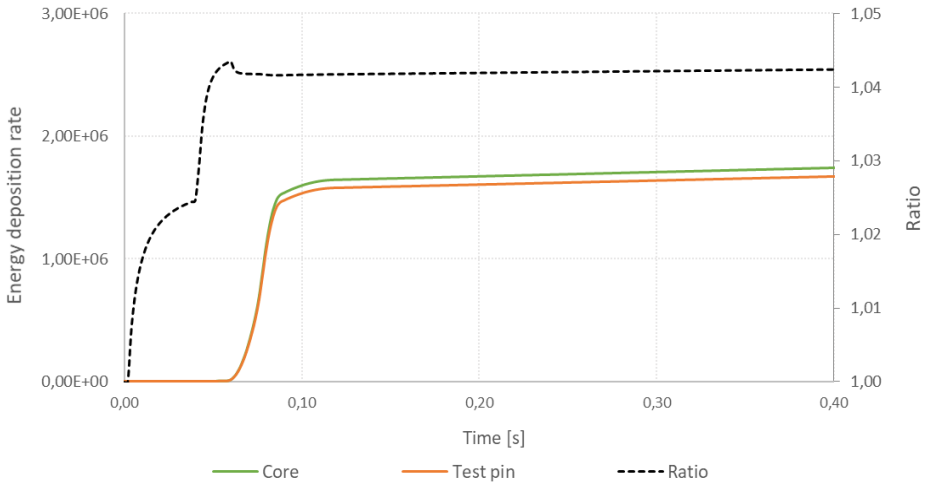


Figure 68. Energy deposition rate in the core and in the test pin during the transient. Results obtained with the static module

5.1.2. Impactful parameters on the energy deposition

The main parameters characterizing the power pulse, such as the peak power, the pulse length and the total energy deposition, depend on the operational characteristics of the reactor and are adjustable by experiment design in the case of the CABRI reactor. The initial pressure of the helium gas and the kinetics of the depressurization determine the maximum core power attained and the duration of the transient, while the total energy deposition can be finely tuned by the timing of the control rod drop.

The reactor core, including the pressurized water loop, is accurately modelled however, as explained in Chapter 3, the fuel temperature in the core is not discretized either radially or axially in the current test cases. Each fuel pin, including the test pin, has the same temperature and temperature evolution. Furthermore, the pressurized water loop is modelled as a water loop at ambient pressure and the moderator at 20°C, similar to the core conditions. In addition, the choice in the test pin and its burnup can also influence the energy deposition during a transient. Lastly, the calculation scheme itself can entail biases and approximations.

The impactful parameters on the transient energy deposition can be classified as experimental, physical, or calculation parameters. The experimental parameters entail the helium pressure,

depressurization kinetics (simple or double depressurization, opening time of the valves etc..) and the test pin characteristics (fuel type and burnup). The physical parameters include the different feedbacks, such as the temperature and the thermomechanical feedback. As for the simulation parameters, these include the fuel pin discretization (isotopic composition and temperature), the calculation methodology (energy deposition estimated from fission energies or based on nuclear heating) and the choice in nuclear data library.

The following sections will focus on the impact of the experimental and physical parameters, through the results of the prompt-supercritical test case. The bias introduced by the calculation methodology is also discussed in detail in Chapter 5.1.3. Concerning the simulation parameters, the impact of the modelling assumptions in the case the test pin including the thermo-mechanical feedbacks, are not addressed at the current stage of the calculation scheme development. The accurate isotopic representation of the fuel pin is part of the future work.

5.1.2.1. Impact of the helium pressure on the energy deposition

The initial helium pressure is one of the defining parameters of the final energy deposition. The goal of this study is to analyze how the helium depressurization influences the energy deposition rate, or, more precisely, to estimate whether the depressurization has the same impact on the energy deposition into the test pin and into the core.

The impact of the helium depressurization is studied using the case of the 11.5 bar depressurization. As can be observed in Figure 66, the transient can be divided into three main stages. First, there is the rapid depressurization phase, where the helium pressure changes significantly. This is followed by the prompt power and core temperature increase, which is terminated by the Doppler feedback, and the final state (minimum pressure, maximum fuel temperature).

The energy deposition rate is compared between the initial core configuration, with the helium at 11.5 bar, and the third geometry, where the helium is at 3.71 bar, while the other parameters of the core remain unchanged. The results are illustrated in Figure 69. This ratio describes the rate of energy increase in the core and test pin. A ratio higher than one means that there is higher relative energy deposition in the core than the test pin.

The main conclusion is that the helium depressurization leads to an increase in the relative difference in the energy deposition rate between the core and the test pin. In other words, the power increase resulting from the helium depressurization is more important in the driver core than in the central test pin. Conversely, as the depressurization progresses, for the same amount of energy deposited in the core, there is relatively less energy deposited in the test pin.

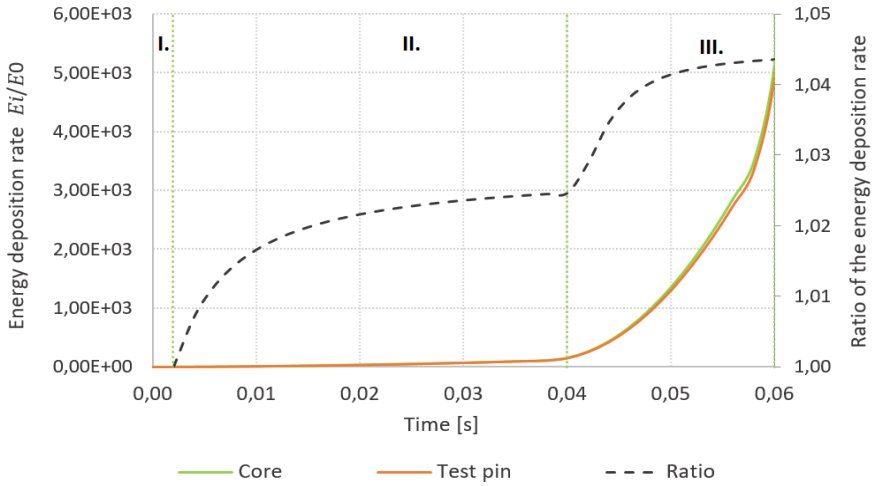


Figure 69. Energy deposition rate in the core and test pin and the relative difference in the energy deposition rate between the core and the test pin

This was observed already when looking at the flux distribution in the core during the transient. Overall, the flux increase in the driver core was more important than the flux increase in the test pin. This translates to a relatively higher increase in the fission reaction rates of the core assemblies than in the fission reaction rates of the test pin. Figure 70 presents a schematic view of a quarter of the core and the relative variations in the fission reaction rates per assembly between the first and third core configurations. The reaction rate increase in the transient assembly and its surroundings (28% in the case of the transient assembly) is more important than the increase towards the center of the core, including the test pin.

These results emphasize once again that the increase in the periphery of the core is significantly higher than in the center of the core, and it is this difference in the power distribution that leads to different energy deposition rates in the core and test pin as the depressurization progresses.

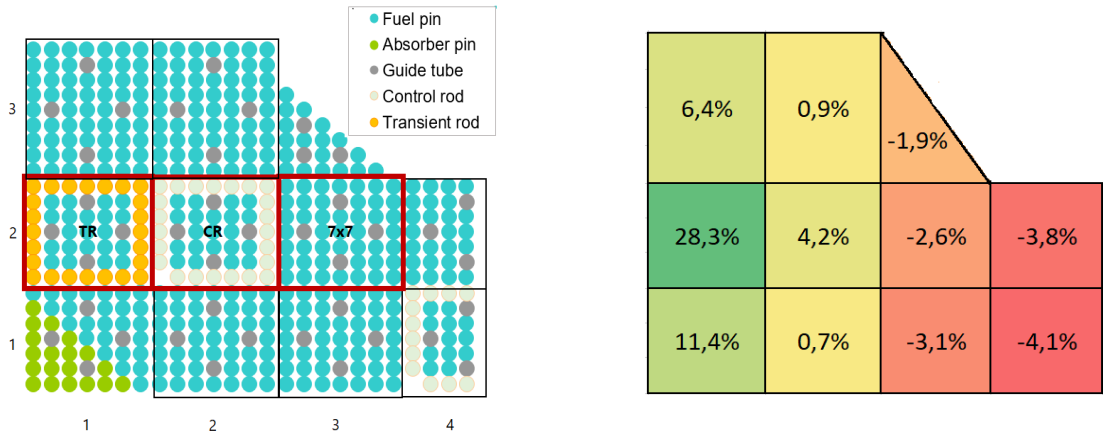


Figure 70. Schematic view of the quarter core and the variation in the fission reaction rates between the two core configurations

5.1.2.2. Impact of the fuel pin type on the energy deposition

Another parameter that might have a significant impact on the energy deposition between the core and the test pin is the test pin type (i.e. its isotopic composition). The isotopic composition is defined by both the fuel type (UO_2 or MOX) and the burnup of the pin. Accordingly, four different fuel pins were chosen for this study: UO_2 and MOX in both fresh and irradiated state. A simple depressurization form 11.5 bar was simulated for the different fuel pins. The final energy deposition into the different fuel pins, as well as the main parameters of the fuel pins, is summarized in Table 5.

FUEL TYPE	ENRICHMENT	BURNUP	ENERGY DEPOSITION
Fresh UO_2	6%	-	0.722 MJ
Irradiated UO_2	3.7%	50 GWd/t	0.340 MJ
Fresh MOX	7%	-	0.696 MJ
Irradiated MOX	7%	50 GWd/t	0.606 MJ

Table 5. Total energy deposition in the case of different test pins

The energy deposition is estimated based on the energy generated during the fission events, and as such, the final energy deposition is proportional to the fissile content of the fuel pin. The highest energy deposition is obtained when using a fresh, 6% enriched UO_2 fuel pin[a], and the lowest with the irradiated UO_2 pin with 3.7% enrichment. The results also illustrate the impact of the burnup on the energy deposition. In the case of the MOX fuel, 50 GWd/t burnup results in 15% lower energy deposition following a similar transient.

Figure 71 presents the evolution of the ratio of the energy deposition rate in the core and in the test pin for the different type of pins. At the early stages of the transient, the energy deposition rate is similar for the different pins. However, the impact of the different isotopic compositions becomes apparent with increasing temperatures. Towards the end of the transient, the energy deposition ratio is smaller for the fuel pins with plutonium content compared to UO_2 fuels, and in irradiated fuels compared to fresh ones. A smaller energy deposition ratio translates to a higher energy deposition rate in irradiated and MOX fuel pins than in the fresh UO_2 pin (the energy deposition rate in the core is the same in all cases).

In chapter 4, it was shown that the neutron spectrum does not change significantly during the transient, and as such, the difference in the energy deposition rate can be attributed to the

[a] The fissile content of a 7% enriched MOX fuel corresponds to approximately to the fissile content of a 4.5% enriched UO_2 pin (World Nuclear Association, 2017).

Doppler feedback being less efficient in the case of the fresh UO_2 pin than the fuel pins containing plutonium isotopes.

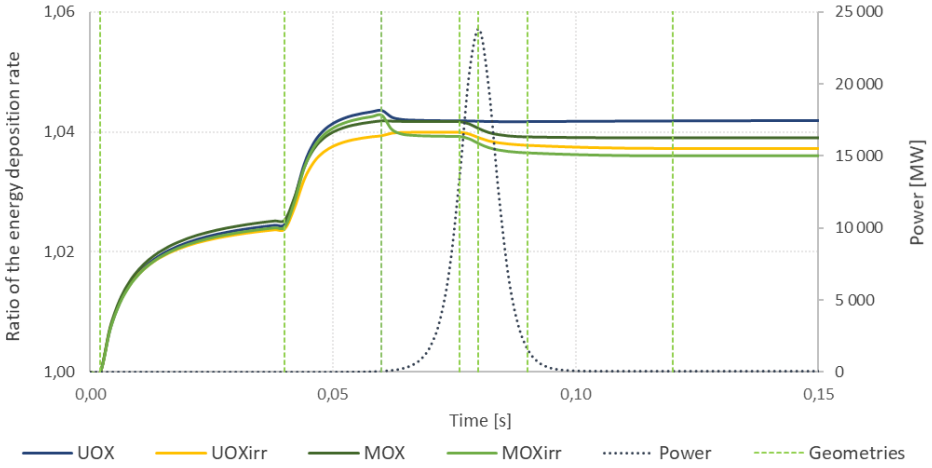


Figure 71. Relative difference in the energy deposition rates between the core and the different test pins

5.1.2.3. Impact of the transient type on the energy deposition

Besides the initial helium pressure, it is the depressurization type that defines the pulse length and the power peak, which ultimately determines the energy deposition. The transient chosen to be compared to the simple depressurization test case is a double depressurization from 11.5 bar. The simple depressurization can be described by short but energetic power pulses, while the double depressurization leads to a longer pulse with a lower power peak. This depressurization leads to a power pulse of 0.2 seconds and a peak power of 3.5 GW, resulting in 252 MJ energy deposition into the core and 0.51 MJ energy deposition into the fresh UO_2 test pin. The main parameters, including the chosen geometries, are displayed in Figure 72.

The difference between the final energy deposition between the simple and double depressurization is summarized in Table 6. Even with the same initial helium amount in the transient rods, the final energy deposition can significantly vary between different depressurization types. Overall, the simple depressurization results in a significantly higher energy deposition.

DEPRESSURIZATION TYPE	POWER PEAK [GW]	FWHM [ms]	ENERGY DEPOSITION IN THE CORE [MJ]	ENERGY DEPOSITION INTO THE TEST PIN [MJ]
Simple depressurization	21	9.5	386	0.70
Double depressurization	3.5	22	282	0.51

Table 6. Energy deposition in the case of the studied depressurizations

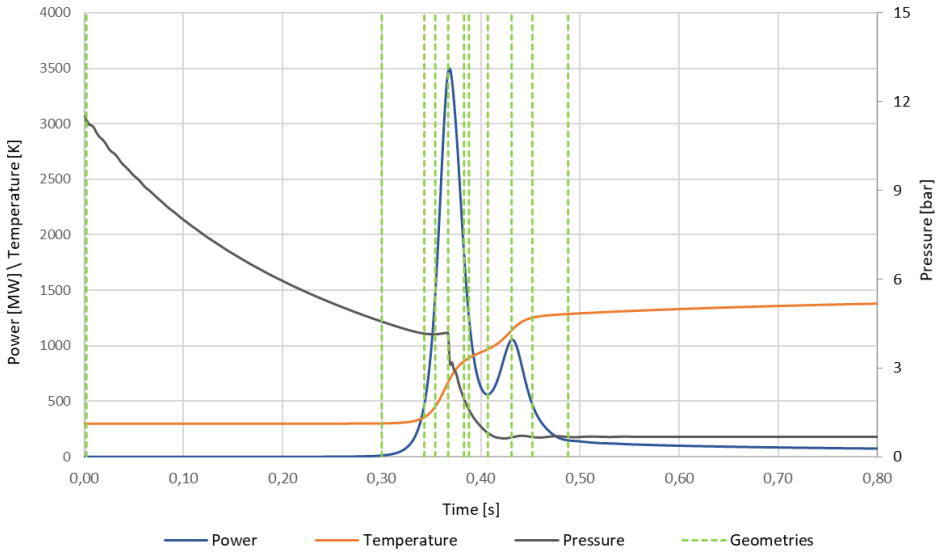


Figure 72. Evolution of the parameters of the double depressurization. The vertical lines represent the geometries chosen to model the transient. Results are obtained with PALANTIR

Figure 73 presents the energy deposition into the test pin during the simple and double depressurizations. In both cases, the most important part of the energy deposition happens during the power pulse. In the case of the double depressurization, the impact of the two power peaks, which in this case represent different helium depressurization speeds, on the energy deposition rate can also be observed.

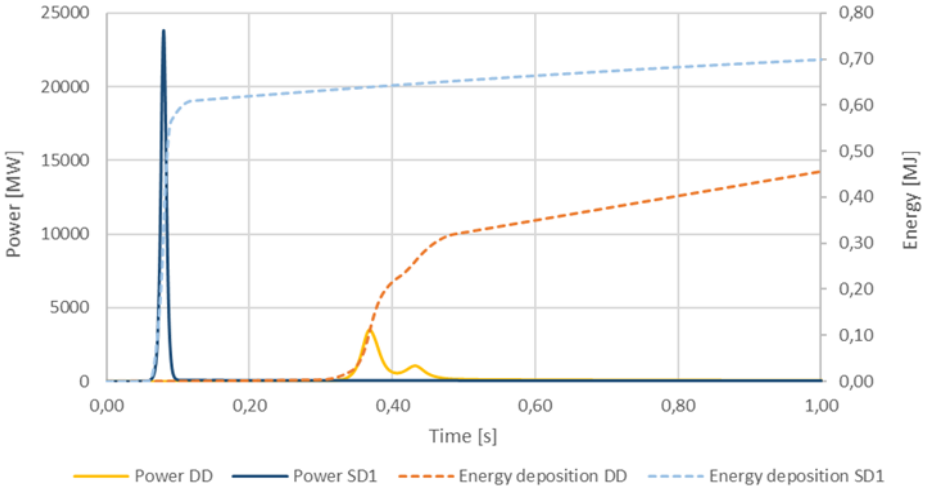


Figure 73. Energy deposition into the test pin during the simple and double depressurization

Finally, the ratio of the energy deposition rate between the core and the test pin is computed for both depressurizations, shown in Figure 74. The jumps that can be observed in the ratio are due to the geometry changes. The ratio and its evolution are similar between the simple and

double depressurization and it reflects that the energy deposition rate in the core is higher than in the test pin. This difference is mainly determined by the helium depressurization in both cases and it increases to ~1.05 by the end of the transient. These results also suggest that the energy deposition variation depends not only on the initial helium pressure but on the depressurization type (i.e. pulse length) as well.

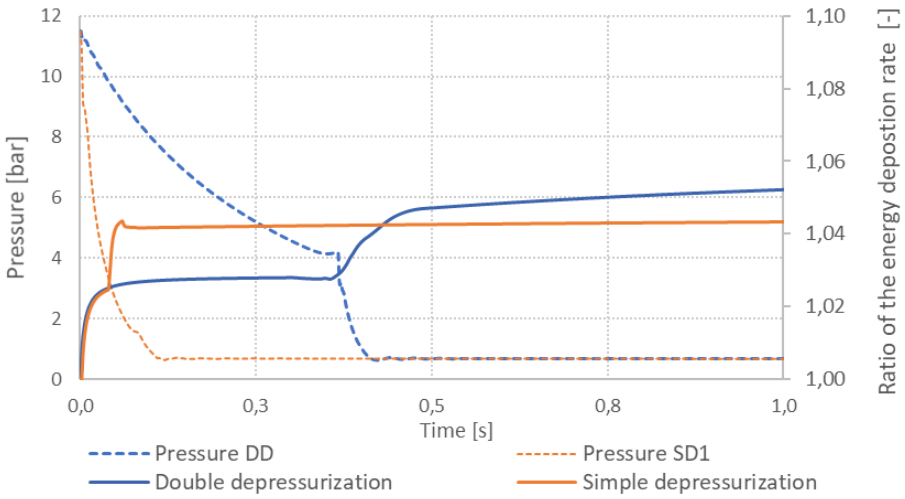


Figure 74. Ratio of the energy deposition rate between the core and test pin for the simple (SD) and double (DD) depressurization

5.1.3. Energy deposition estimated from nuclear heating

The main assumption of the energy deposition calculation based on the fission energies is that all of the energy generated during fission is deposited where the fission takes place. Consequently, the energy deposition due to the long-range particles originating from the driver core is not taken into account, neither is the energy deposited outside of the test pin by the particles created in the test pin. The aim of this study is to compute the nuclear heating in the test pin (fissile volume and cladding) in order to define the proportion of the fission energy that is deposited outside the test pin. This proportion is referred to as the energy distribution factor and. It is also evaluated whether this factor changes during the transient and if it is dependent on the fuel pin type.

The energy generated during fission appears as the kinetic energy of the fission products and the energy of the neutron, gamma and beta particles created during fission and subsequent decay events. These particles convey their energy to the surrounding medium depending on specific interactions, characteristic to each particle type. This determines the spatial repartition of the fission energy.

This calculation scheme, originally developed for steady-state calculations, is adapted for the power pulse as well. The transient is modelled by consecutive core configurations, as in the case of the energy deposition estimation based on fission energies. The nuclear heating is calculated for each of the chosen geometries of the simple depressurization from 11.5 bar and the same four fuel pins from the last section.

The energy distribution factor (F_{out}) is defined as:

$$F_{out} = 1 - \frac{Energy\ deposited\ in\ the\ test\ pin}{Energy\ generated\ in\ the\ test\ pin} = 1 - \frac{E_{pin\rightarrow pin} + E_{core\rightarrow pin}}{E_{pin\rightarrow pin} + E_{pin\rightarrow outside}} \quad (5.2)$$

Where: $E_{pin\rightarrow pin}$ is the part of the fission energy released inside the test pin that is deposited into the test pin

$E_{core\rightarrow pin}$ is the energy deposited into the test pin due to a particle originating from the core

$E_{pin\rightarrow outside}$ is the part of the fission energy released inside the test pin that is deposited outside of the test pin

Before presenting the results of the nuclear heating scheme, the delayed and prompt contribution during the power pulse will be discussed.

5.1.3.1. Delayed nuclear heating contribution during the power pulse

The first step of the delayed heating calculation is the definition of the delayed beta and gamma sources for the different fissile isotopes. More precisely, the delayed spectrum and the multiplicity of the source are defined. The multiplicity is determined by the reaction rates in the fissile volume, meaning that it depends on the power level. Consequently, the irradiation time can be divided into two parts: a steady-state irradiation and the power pulse.

The delayed contribution during the power pulse can be estimated as the sum of the delayed heating determined for each intermediate configuration step. However, due to the high computational need for the delayed heating calculation and the low delayed heating contribution during the pulse, the power pulse is represented instead by considering a steady-state operation at the peak power for a time length of 0.2 seconds. This gives a rough (over)estimation of the delayed heating contribution during the power pulse.

Figure 75 presents the beta spectrum for the three main fissile isotopes after 1 hour of irradiation, representing the steady-state, and 0.2 seconds, representing the spectrum during the pulse. While the spectrum does not differ significantly between the different isotopes, it is significantly harder in the case after 0.2 seconds.

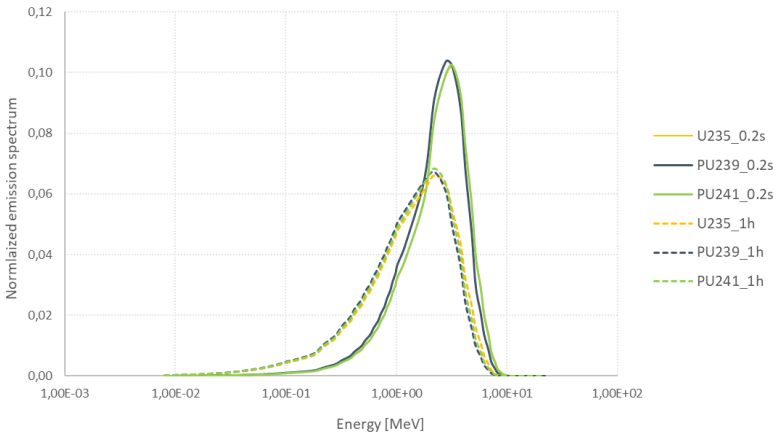


Figure 75. Delayed beta spectrum for the different isotopes and irradiation time.
The spectrum is normalized to 1

The same can be observed for the gamma spectrum, which is presented in Figure 76 for a 0.2 s irradiation time and in Figure 77 for 1 hour of irradiation. However, this difference in the delayed spectrum between steady-state and the transient state has no significant impact on the total energy deposition. The calculations run for a fresh UO_2 test pin show that the contribution of the delayed heating deposited during the power pulse amounts to only 0.04% of the total nuclear heating during the pulse. As such, it will not be considered. The delayed heating presented in the following section refers to the delayed heating deposited during the steady-state irradiation.

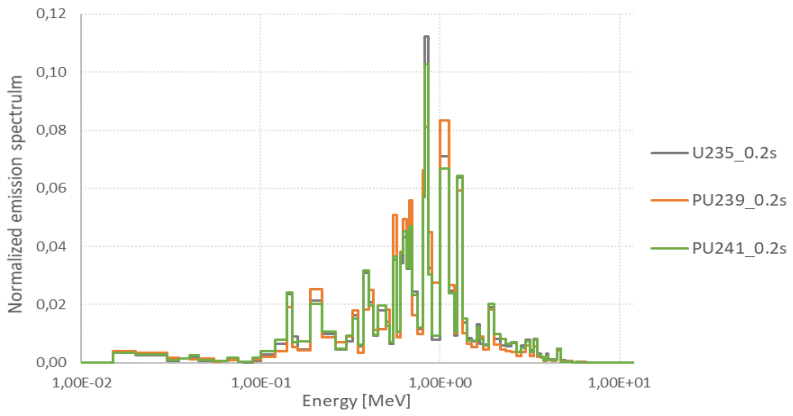


Figure 76. Delayed gamma spectrum after a 0.2 s irradiation for the different fissile isotopes.
The spectrum is normalized to 1

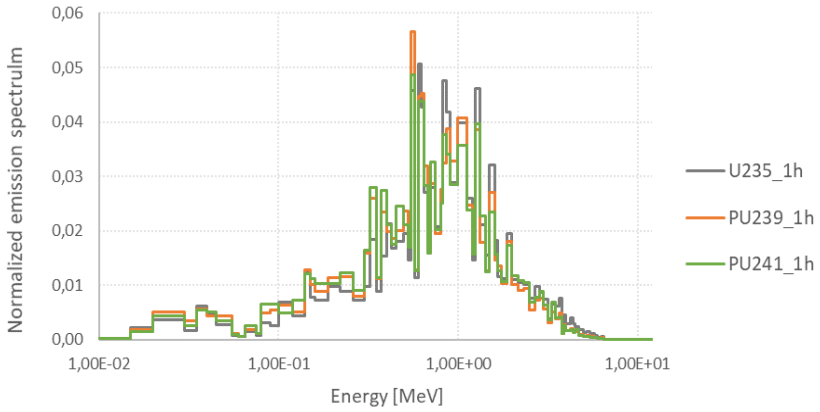


Figure 77. Delayed gamma spectrum after 1 hour of irradiation for the different fissile isotopes. The spectrum is normalized to 1

5.1.3.2. Prompt nuclear heating contribution during the power pulse

The prompt nuclear heating is obtained by running a 4-particle criticality calculation. TRIPOLI-4® calculates the energy deposited by the charged particles as they move through the studied volume in units of MeV/s. Normalizing it to the core power (see Equation (2.27)) gives the power deposition into a given volume, which, if integrated over the irradiation (and eventual cooling) time, gives the total energy deposition. In order to be able to compare the nuclear heating for different core configurations, the following results will be given in power deposition normalized to 1 MW core power, in W/MW.

The particles that deposit their energy into the test pin can originate from either the driver core or the test pin. The distinction in the origin of the particles can be made by running two set of calculations. One where the test pin is replaced by a lead pin and one with the actual test pin. Lead was chosen since it has a density similar of those of the fuel pins. This way, the energy deposited in the test pin in the case of a lead test pin is a result of the particles originating solely from the core. On the other hand, if the test pin contains fissile material, the calculated energy deposition into the water loop includes both the energy deposition due to the particles originating from the test pin and from the core.

Table 7 presents the distribution of the prompt power released in a fresh UO_2 test, the power deposition due to the particles originating from the core and the energy distribution factor for different core configurations. These calculations concluded that the energy distribution factor is constant regardless the core configuration. Taking into consideration that the contribution of the delayed heating during the power pulse is inconsequential and that the ratio of the prompt energy being deposited outside the test pin is constant during the pulse, a conclusion regarding the spatial distribution of the energy can be determined from the steady-state results, presented in the following section.

	$P_{pin \rightarrow pin}$ [W/MW]	$P_{core \rightarrow pin}$ [W/MW]	$P_{pin \rightarrow outside}$ [W/MW]	Energy distribution factor F_{out} [%]
Geometry #1 11.5 bar 300 K	1551 ± 0.13%	14 ± 0.23%	207 ± 1.28%	11.0 ± 0.21%
Geometry #2 3.71 bar 300 K	1592 ± 0.13%	14 ± 0.23%	212 ± 1.28%	10.9 ± 0.27%
Geometry #4 1.57 bar 774 K	1561 ± 0.13%	14 ± 0.23%	208 ± 1.28%	10.9 ± 0.19%
Geometry #5 1.55 bar 1474 K	1564 ± 0.13%	14 ± 0.23%	206 ± 1.28%	10.8 ± 0.20%

Table 7. Prompt power deposition into the test pin for different core configurations

5.1.3.3. Spatial distribution of the nuclear heating

The results concerning the distribution of the fission energy are presented in two steps. Table 8 presents the spatial distribution of the prompt and delayed heating in the case of a fresh UO_2 test pin. The delayed heating contribution represents 3% of the total power deposited in the test pin. The contribution of the particles originating from the core represents 1% of the total energy deposited in the test pin, while 13% of the total fission energy generated in the test pin is deposited outside of the pin.

	Prompt power deposition [W/MW]	Delayed power deposition [W/MW]
$P_{pin \rightarrow pin}$	1551 ± 0.12%	56.23 ± 1.10%
$P_{core \rightarrow pin}$	14 ± 0.28%	2.05 ± 1.47%
$P_{pin \rightarrow outside}$	204 ± 1.28%	35.09 ± 0.90%

Table 8. Decomposition of the power deposition by spatial distribution and by prompt and delayed components for a fresh UO_2 fuel pin. Values normalized to 1 MW core power

In order to evaluate the impact of the test pin type on this distribution factor, the same calculations were carried out for the four different fuel pin types. Table 9 presents the power deposition into each pin, including the energy distribution factor. In this case the power deposition represents the total power: the sum of the prompt and delayed heating.

	$P_{pin \rightarrow pin}$ [W/MW]	$P_{core \rightarrow pin}$ [W/MW]	$P_{pin \rightarrow outside}$ [W/MW]	Energy distribution factor F_{out} [%]
Fresh UO_2	1607 ± 0.12%	16 ± 0.23%	239 ± 1.08%	12.22 ± 0.21%
Irradiated UO_2	854 ± 0.16%	18 ± 0.23%	107 ± 1.45%	9.25 ± 0.27%
Fresh MOX	1731 ± 0.11%	18 ± 0.23%	291 ± 0.87%	13.49 ± 0.19%
Irradiated MOX	1520 ± 0.12%	18 ± 0.23%	179 ± 1.20%	9.50 ± 0.20%

Table 9. Decomposition of the power deposition by spatial distribution for the critical core configuration, normalized to 1 MW core power

The majority of the energy deposited in the test pin (~95%) is the energy deposited by the particles originating from the pin and 11 to 15% of the total fission energy released in the test pin is deposited outside of the test pin. This ratio is the highest for the fresh fuel pins. The heating originating from the core represents, depending on the fuel type, 1 to 2% of the total energy deposition. This contribution was also evaluated for different core configurations and found to be constant. The contribution from the core somewhat compensates the energy loss due to the particles leaving the test pin, as it can be observed in energy distribution factor, which is, depending on the fuel pin type, 9 to 14%.

5.2. Coupling factor evolution during a transient

As described in Chapter 1.3.1, the coupling factor, used to calculate the energy deposition in the test pin, is measured for the critical core configuration. It represents the ratio of the core and test pin power, which are both measure via thermal balances on the driver core and water loop, respectively. This definition entails the same approximations as discussed for the energy deposition calculation: constant coupling factor throughout the transient and not taking into account the spatial distribution of the fission energy generated in the test pin. The thermal balance measurement on the water loop incorporates the part of the fission energy generated in the test pin that is deposited outside of the pin.

In the following sections, the same transients will be presented as for the energy deposition study, but this time the results will be focused on the coupling factor and its evolution during the depressurizations. First, the approximations induced by the hypothesis of the constant coupling factor is evaluated based on the results of the stepwise calculation scheme, then the coupling factor is calculated with the nuclear heating scheme to assess the impact of the fission energy distribution in the water loop.

The following coupling factor definitions are used throughout this section:

- *Steady-state coupling factor* refers to the coupling factor corresponding to the critical core configuration and the initial instantaneous coupling factor
- *Instantaneous coupling factor* is computed for each chosen core configuration
- *Stepwise coupling factor* calculated by interpolating between two instantaneous coupling factors, with the mention that it is considered constant following the final core configuration
- *Dynamic coupling factor* is given by dividing the dynamic core and test pin power
- *Revised coupling factor* is calculated from the stepwise coupling factor and the energy distribution factor

The aim of this analysis is to study the possible variation of the coupling factor during the transient, to determine the parameters that influence its variation and to propose a new calculation method for the coupling factor based on its observed behavior.

5.2.1. Coupling factor evolution during a supercritical transient

Figure 78 summarizes the coupling factor evolution as obtained with the different calculation methodologies. The stepwise coupling factor is in good agreement with the results given by the dynamic scheme, keeping in mind the high statistical error (~5%) on the dynamic scores. The statistical error on the steady-state and interpolated coupling factor is in the order of 0.2%.

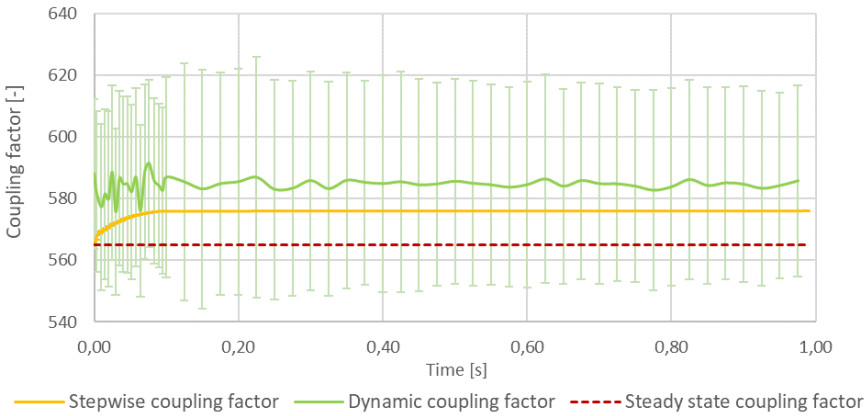


Figure 78. Coupling factor variation during the supercritical transient. Results obtained with the stepwise and dynamic methodology

With the error on the dynamic scores being higher than the coupling factor variation predicted by the stepwise results (2% higher instantaneous coupling factor at the end of the transient as opposed to the steady-state coupling factor), the coupling factor variation cannot be

conclusively defined in this case. These results correspond to the relative difference between the energy deposition rates in the core and in the test pin, as observed in the previous section, since both parameters describe the energy distribution between the core and the test pin.

5.2.2. Coupling factor evolution during a prompt-supercritical transient

The stepwise coupling factor is calculated by linearly interpolating between two instantaneous coupling factor values, with the assumption that the coupling factor is constant between the final core configuration and the end of the transient. The coupling factor evolution is depicted in Figure 79. It increases by 6% during the transient and the impact of the geometry changes is reflected in its variation. It is important to note that the most significant increase in the coupling factor happens before the power peak, meaning that there is a significant difference between the coupling factor describing the critical core and the coupling factor describing the core during the power pulse.

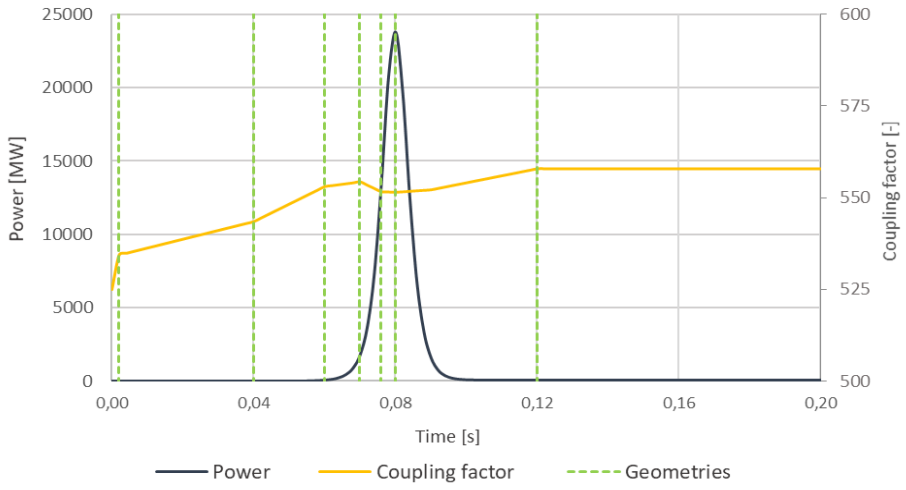


Figure 79. Coupling factor variation during the prompt-supercritical transient. Results obtained with the stepwise calculation scheme

As presented in earlier chapters, the two core parameters that both change during this transient and are included in the modelling are the helium pressure and the fuel temperature. The early stage of the transient is characterized by a rapid depressurization but no temperature increase (~80% of the helium is depressurized before the any significant temperature increases), while the pulse can be described by a significant temperature increase and a less important pressure decrease (~1500 K and 2 bar respectively).

Table 10 contains the pressure and temperature of each geometry and the corresponding coupling factor. By comparing the coupling factor variation between the first and third geometry (significant pressure difference with no temperature variation) and between the geometry #6 and #7 geometry (important temperature variation, insignificant pressure variation) the following conclusion can be drawn. The helium depressurization results in a coupling factor increase, which can be explained by the asymmetry of the energy deposition rates into the core and in the test pin. Since the energy deposition is more important in the core than in the test pin as the depressurization progresses, their ratio, the coupling factor, increases.

GEOMETRY #	HELIUM PRESSURE [BAR]	FUEL TEMPERATURE [K]	COUPLING FACTOR
1	11.5	300	525 ± 0.12%
2	6.54	300	534 ± 0.12%
3	3.71	300	544 ± 0.12%
4	1.94	314	553 ± 0.12%
5	1.72	474	552 ± 0.12%
6	1.57	774	552 ± 0.12%
7	1.55	1474	552 ± 0.12%
8	1.15	1840	552 ± 0.12%
9	0.67	1840	558 ± 0.12%

Table 10. Helium pressure, fuel temperature and instantaneous coupling factor for the different core configuration of the 11.5 bar transient

On the other hand, it can be observed that as the fuel temperature increases and the Doppler feedback becomes more apparent, the increase in the coupling factor due to the helium depressurization is mitigated, indicating that the Doppler feedback tends to decrease the coupling factor (the neutron spectrum is harder in the core). However, the effect of the Doppler feedback is secondary to the helium depressurization.

5.2.3. Impact of the fuel pin type on the coupling factor

The stepwise coupling factor was computed for four different test pins, similar to the case presented in Chapter 5.1.2.2. Since the test pin power is proportional to the fissile content of the pin, the initial values of the coupling factor, corresponding to the critical core configuration, are different. The results are summarized in Table 11 according to the test pin type. It can also be observed that the coupling factor is decreasing with increasing fissile content, i.e. more energy is deposited in test pins with higher fissile content. This is similar to the observation made regarding the energy deposition in the case of different fuel pins (refer to chapter 5.1.2.2).

FUEL TYPE	ENRICHMENT	BURNUP	COUPLING FACTOR
Fresh UO_2	6%	-	525 ± 0.12%
Irradiated UO_2	3.7%	50 GWd/t	1120 ± 0.12%
Fresh MOX	7%	-	546 ± 0.12%
Irradiated MOX	7%	50 GWd/t	630 ± 0.12%

Table 11. Steady-state coupling factor for different test pins

Even though the isotopic composition of the test pin has a significant impact on the coupling factor value, the coupling factor variation itself is similar in the case of the different fuel pins, as shown in Figure 80. In the early stages of the transient, where the helium depressurization is characteristic, the coupling factor variation is the same for the different pins. The difference in the coupling factor variation starts to become visible in the second part of the transient, when the Doppler feedback becomes prominent. This can be attributed to the lower Doppler coefficient of the fuel pins containing plutonium.

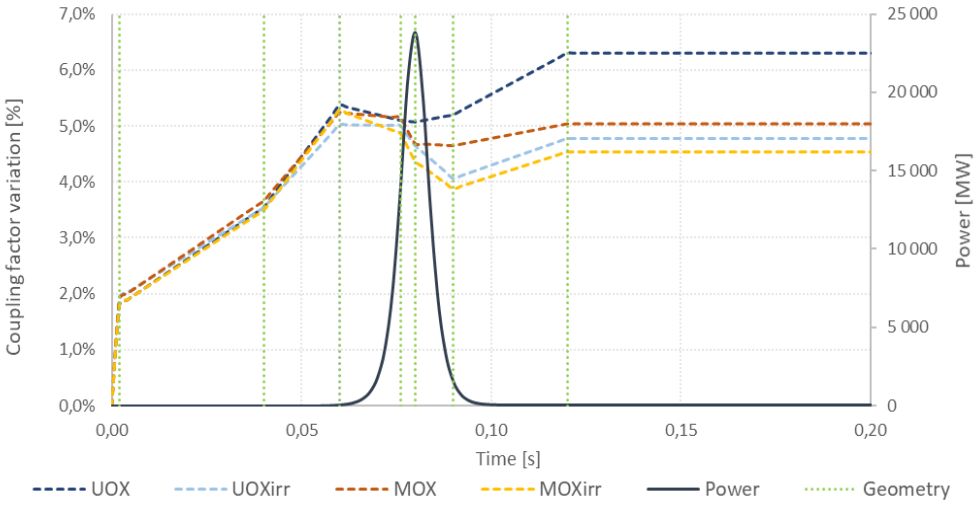


Figure 80. Coupling factor variation for different fuel pin types. The vertical lines represent the different core configurations

However, the trend in the coupling factor variation is similar for all fuel pin types. The coupling factor increases with the decreasing helium pressure (for example before 0.06 s and after 0.1 s), and decreases with the Doppler feedback. Moreover, it can be concluded that the test pin type has only secondary impact on the coupling factor evolution, since the impact of the depressurization is the same for each fuel type and the difference in the coupling factors for the different fuel pins during the power pulse (where the majority of the energy deposition happens) is significantly less important than the effect of the depressurization.

5.2.4. Impact of the depressurization type on the coupling factor

Figure 81 presents a comparison between the coupling factor variation in the case of a simple and a double depressurization. The initial coupling factor is 525, which increases to 558 in the case of the simple depressurization and to 559 in the case of the double depressurization, representing a ~6% increase. The statistical uncertainty on the coupling values is 0.1% and the evolution of the coupling factor is similar in both cases. The coupling factor increases as the helium presence in the transient rods decreases, and it slightly decreases as the Doppler feedback becomes more important (which coincides with the end of the depressurization).

The opening of the second valve during the double depressurization, which leads to a faster pressure loss, can be observed in the coupling factor evolution as well. This underlines again, that the coupling factor variation is strongly dependent on the helium pressure variation.

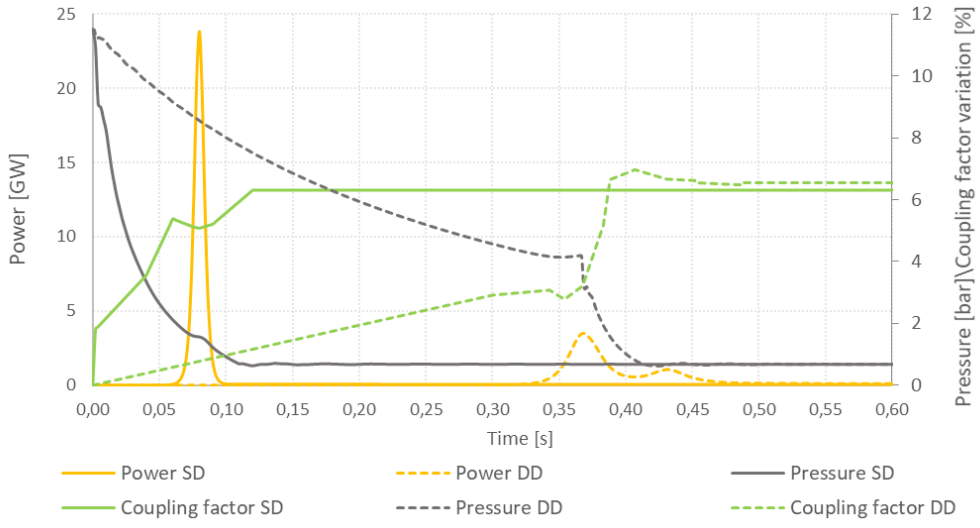


Figure 81. Coupling factor and helium pressure evolution during the simple (SD) and double (DD) depressurization

5.2.5. Coupling factor and energy deposition

As previous results show, the coupling factor changes during the transient and its evolution is primarily determined by the helium pressure variation and secondarily by the fuel temperature increase. In addition, calculating the energy deposition from a coupling factor based on the fission energy calculation scheme gives the value of the energy generated in the test pin and not the energy deposited in the pin, these two values being related through the energy distribution factor.

Thus, the notion of a revised coupling factor can be introduced, which accounts for both the coupling factor variation, through the stepwise coupling factor ($C_{stepwise}(t)$) and the difference between the generated and deposited energy through the correction factor (F_C), defined based on the energy distribution factor. This revised coupling factor can be defined as follows:

$$C_{revised}(t) = C_{stepwise}(t) \cdot F_C \tag{5.3}$$

$$F_C = F_{out} + 1 \tag{5.4}$$

To obtain the revised coupling factor, the energy distribution factor has to be calculated first with the nuclear heating scheme for the critical core configuration. Then, an instantaneous coupling factor should be calculated for the representative core configurations (early phase of depressurization, beginning of the pulse, at the power peak(s), and the end of the power pulse), and then the stepwise coupling factor can be computed from these values.

The impact of the coupling factor variation on the energy deposition calculation for the test pin can be illustrated by comparing the total energy deposition into the test pin obtained with the steady-state coupling factor and the revised coupling factor, as summarized in Table 12 for a simple and a double depressurization from 11.5 bar. This study shows that using the steady-state coupling factor could result in a 20% overestimation of the energy deposition in the test pin.

	SIMPLE DEPRESSURIZATION		**DOUBLE DEPRESSURIZATION**	
	Energy deposition	Relative variation	Energy deposition	Relative variation
Steady-state coupling factor	0.55 MJ ± 0.31%	-	0.54 MJ ± 0.31%	-
Revised coupling factor	0.46 MJ ± 0.31%	-20%	0.45 MJ ± 0.31%	-20%

Table 12. Energy deposition into a fresh UO_2 test pin calculated from the energy deposition in the core and the different coupling factor values

This underlines the observation that the steady-state coupling factor is not representative of the core (more specifically to the energy distribution between the core and test pin), during the power pulse, where ~85% of the energy deposition happens.

5.3. Summary

The objective of this chapter was to evaluate the energy deposition into the test pin during a transient, the energy distribution between the core and the test pin, and to assess the impact of the influencing parameters on the energy deposition. Two transients were considered, a supercritical transient, which enables the comparison of the stepwise and dynamic calculation schemes, and a prompt-supercritical transient that allows the analysis of the energy deposition process.

The studies conducted on the supercritical transient concluded that the energy deposition trend is in good agreement between the static and dynamic results, however, the systematic error observed the dynamic flux calculation appears in the energy calculation as well. The stepwise results also predict a difference in the energy deposition rate in the core and test pin. Given that this difference is in the same order of magnitude as the statistical uncertainty, it could not be definitively determined in the case of the dynamic calculation. This difference in the energy deposition rate between the core and the test pin is found in the case of the prompt-supercritical transient as well. The calculations show that there is relatively more energy deposited into the core than the test pin during the depressurization and it this difference reaches 5% in the case of a simple depressurization form 11.5 bar.

Both the depressurization type and the fuel type define the final energy deposited into the test pin. For the same initial helium pressure, there is ~40% more energy deposited into the same test pin in the case of a simple depressurization, while the final energy deposited into a test pin is proportional to the fissile content of the pin. But it was found that neither the test pin type nor its burnup has any significant impact on the energy deposition rate evolution.

In the case of the prompt supercritical transient, the energy deposition was also estimated from the nuclear heating. This methodology takes into account the spatial distribution of the fission energy. The results showed that around a significant amount of the fission energy generated in the test pin is actually deposited outside the test pin. This is described by the energy distribution ratio, which also takes into account the energy deposition from the particles originating in the test core. This ratio does not change during the depressurization, but it does change depending on the test pin type: the calculations suggest that this ratio increases with increasing fissile content. For the test pins considered in this study (fresh and irradiated UO_2 and MOX with 6 and 7% enrichment, respectively) it varied between 9 and 14%. In other words, estimating the energy deposition from the reaction rates and fission energies overestimates

the total energy deposition into the test pin, and a suitable correction factor, corresponding to the energy distribution factor, should be applied to it.

The energy deposited into the test pin can also be calculated using the coupling factor, which describes the energy distribution between the core and the test pin. The coupling factor was calculated for each transient and fuel type mentioned before. The results showed that it increases during the transient and its evolution is primarily affected by the helium depressurization. This also means that calculating the energy deposition based on the coupling factor determined for the critical core configuration, as is the current practice, overestimates the energy deposited in the test pin. For example, in the case of the simple and double depressurizations from 11.5 bar, the energy deposition overestimation reaches 6%.

In order to take into account the variation of the coupling factor and the spatial distribution of the energy when calculating the energy deposition (especially in the case of the CABRI experiments), the steady-state coupling factor should be replaced by the revised coupling factor. The latter corresponds to the stepwise coupling factor weighted by the energy distribution factor. The results showed, that using the steady-state coupling factor entails a 20% overestimation of the energy deposited in the test pin.

6. CONCLUSIONS AND PERSPECTIVES

One of the main areas of interest of nuclear safety analysis is the behavior of nuclear fuel during operational and accidental situations. In the CABRI reactor the fuel pin to be examined (test pin) is placed in the center of the core in a dedicated test loop. It is then subjected to a power transient, obtained by the fast depressurization of the neutron absorber gas (helium-3) from transient rods located in the core. One of the central parameters of the experiment is the energy deposition into the test pin, which is currently not measured during the transient. Instead, it is calculated from the energy deposition in the driver core and the coupling factor. The coupling factor refers to the ratio of the core and test pin power and consequently the ratio of the deposited energy. It is measured in steady-state operation and applied to the transient state with the assumption that the relative energy distribution between the core and the test pin is constant regardless the operational state of the reactor.

There has been a significant development in recent years concerning the simulation and prediction of the CABRI power pulses. These calculation tools aimed at creating a more accurate power pulse calculation and on implementing a multiphysics approach. As a complementary approach, this current work aimed at the improvement of the neutron calculation scheme for the parameters of interest of the CABRI transients, by taking into account at the same time the time-dependency and spatial flux variation during a CABRI power pulse.

A transition between static and kinetic Monte Carlo simulations is achieved progressively, by implementing two methodologies. The first methodology is based on steady-state stochastic calculations, where a criticality calculation is run for consecutive core configurations, representative of different stages of the transient. This allows for the observation of the variations in the parameters of interest during the transient with the codes already in use, and sheds a light on the most impactful parameters on the energy deposition rate. In the second methodology the fully dynamic simulation of the transient is obtained by implementing the newly developed dynamic module of the TRIPOLI-4® code, which allows the simulation of non-stationary conditions and can handle geometry changes within the simulation. The transient is modelled with the same core configurations as in the stepwise case. The first part of the work is centered on the implementation of the two aforementioned calculation schemes and the validation of the modelling choices.

Two transients were considered: a supercritical transient, which enables the comparison of the results of the stepwise and dynamic calculation schemes, and a prompt-supercritical transient that allows for an in-depth analysis of the energy deposition process. The supercritical test case is a simple depressurization from 0.72 bar, leading to a ~580 pcm reactivity insertion, while the prompt-supercritical test case is a simple depressurization from 1.4 bar, resulting in a 780 pcm reactivity insertion. The representative geometries are chosen based on the evolution of the

physical parameters (pressure and temperature) and the characteristics of the power pulse, in a way to be representative of the different stages of the transient. Such as the early phase, characterized by the decreasing helium pressure without temperature variation, the power pulse, described by decreasing pressure and increasing temperatures, and the final phase of stabilized pressure and fuel temperature. It was found that ~10 geometries are enough to cover a transient, and more than 15 geometries should be avoided due to memory and running time limitations. Regarding the time steps, in the fast kinetics phase the time steps should be in the order of the prompt neutron lifetime, while in the slow kinetics phase a 0.1 s time steps suffice.

The analysis showed that the modelling with the TRIPOLI-4® kinetic module is able to correctly reproduce the power pulse in comparison with a point kinetics model, the stepwise methodology and the experimental power curve. However, the results also revealed that the kinetic module is only able to calculate the power evolution in the case of the supercritical transient, but not yet for prompt supercritical transients. The analysis of the transient modelling was supplemented with a sensitivity study on the dynamic power calculation for the supercritical transient, focused on the impact of the uncertainties of some experimental and modelling input parameters on the core power calculation. The analysis showed that amongst the parameters considered, the power calculation is the most sensitive to the uncertainty on the pressure measurement, the latter leading to 14% of uncertainty on the final power.

The second part of the work was dedicated to the dynamic energy deposition. Even though there are different approaches for estimating the energy deposition, it was derived in each case from the same physical quantity: the neutron flux. The neutron flux distribution and evolution was analyzed for the stepwise and dynamic simulation for the supercritical case and for the stepwise results in the case of the prompt-supercritical transients. In order to be able to capture stronger feedbacks, a new transient, a simple depressurization from 11.5 bar was considered. The total flux increase in the periphery (where the transient rods are situated) was more important than the flux increase in the center of the core (where the test pin is situated). In the considered case, the flux increased around the transient rods by up to 40% following the depressurization. It was also observed that, while the flux spectrum is harder in the driver core than in the pressurized water loop, it does not change during the depressurization. Concerning the calculation scheme comparison, both the dynamic and the static calculation were able to reproduce the flux shape at different stages of the transient with a good agreement, the discrepancies being in the order of magnitude of the statistical errors. However, the kinetic module seems to underestimate the absolute flux by 3% for the critical state.

As suggested by the flux variations, the energy distribution between the core and the test pin is not constant during a transient and the variations are mainly driven by the helium depressurization. This observation was confirmed in the case of the 11.5 bar prompt-supercritical transient. The calculations showed that there is relatively more energy deposited into the core than in the test pin during the depressurization, this difference reaching 5%. For the same initial helium pressure, there is ~40% more energy deposited into the same test pin

in the case of a simple depressurization compared to a double depressurization (longer power pulse but with lower power peak), while the final energy deposited into a test pin depends on the fissile content of the test pin.

Two limitations of the current energy deposition calculation were identified and quantified: the impact of the energy deposition calculation scheme and the assumption of a constant coupling factor. In the current calculation scheme, all of the generated fission energy is considered to be deposited inside the test pin. The actual spatial distribution of the fission energy is accounted for with the nuclear heating scheme, and is represented by the energy distribution factor. For the test pins considered in this study (fresh and irradiated UO_2 and MOX) this factor ranges from 9 to 14% and it includes the portion of the energy generated in the test pin that is deposited outside the test pin and the energy compensation due to the particles arriving from the core. This factor does not change during the depressurization, and the calculations suggest that this ratio increases with increasing fissile content.

The energy deposited into the test pin can also be calculated using the coupling factor, which describes the energy distribution between the core and the test pin, and in current methodology is defined for the critical core configuration and considered constant. The impact of the latter assumption could be observed using the stepwise calculation scheme, with the energy deposition being calculated from fission energies. The calculations revealed that the coupling factor increases during the transient (by 6% for the 11.5 bar depressurization) and that its variation is impacted by the helium pressure variation, the Doppler feedback resulting, as a homogeneous effect in the core, resulting only in a secondary effect. This also means that the most significant change in the coupling factor happens before the power peak, i.e. the coupling factor corresponding to the critical state is actually not representative of the power pulse. This is especially important since the majority of the energy deposition happens during the pulse.

In other words, estimating the energy deposition from the reaction rates and fission energies and assuming a constant coupling factor both overestimate the total energy deposition in the test pin. In order to take into account the variation of the coupling factor and the correction coming from the spatial distribution of the energy deposition, the revised coupling factor was defined, which corresponds to the stepwise coupling factor weighted by the energy distribution factor. The results showed, that using the steady-state coupling factor could result in an almost 20% overestimation (depending on the transient and test pin type) of the energy deposited in the test pin. Thus, the work presented in this thesis allows to make recommendations on the coupling factor calculation methodology, which can ultimately lead to the improvement of the energy deposition calculation during an experiment in the CABRI reactor.

PERSPECTIVES

In the following, some directions will be given for the possible future developments covering the following areas: modelling of the test pin, kinetic Monte Carlo simulation, multiphysics modelling, coupling factor calculation and the validation of this calculation methodology.

Modelling of the test pin

There are several areas of improvement concerning the test pin and pressurized water loop modelling. Taking into account the temperature evolution of test pin more accurately could influence the coupling factor and thus the energy deposition.

Currently the test pins are modelled with a homogeneous isotopic composition and with the same temperature evolution (axial and radial) as the pins in the driver core. However, for instance in the case of a test fuel with a high burnup, the initial uniform fissile material distribution is changed due to the enhanced neutron resonance capture on the pellet periphery, leading to a local buildup of transuranium isotopes at the pellet outer ring, called the rim region. Accordingly, the radial temperature profile also varies during a transient. The fuel behavior, including the axially and radially discretized temperature variations, could be obtained through an iterative process with the ALCYONE code, which is capable of the simulating the fuel behavior following an energy deposition (Guénot-Delahaie, et al., 2018)

In addition, the water loop is modelled in this work as having the same conditions (moderator pressure and temperature) as the driver core. In order to have a more realistic Doppler and moderator feedback for the test pin and test the water loop should be modelled at its nominal, pressurized conditions. This includes the moderator and test pin temperatures as well. The implementation of the pressurized water loop in PALANTIR, which would give the evolution of the physical parameters in the water loop, is underway.

Kinetic Monte Carlo simulation

Concerning the prospective for the kinetic Monte Carlo simulation of the CABRI reactor, two approaches can be distinguished, depending on the choice of the Monte Carlo code. In the case of transient simulations with TRIPOLI-4® additional developments are needed to be able to simulate prompt-supercritical transient, to solve the discrepancy observed in the absolute flux values between a criticality and a kinetic calculation, to implement of the track estimator for the neutron flux. Furthermore, the treatment of the Doppler feedback has to be improved as well, for example by implementing the on-the-fly Doppler broadening or allowing temperature interpolation with probability tables.

As an alternative, it could be feasible to use other stochastic codes to model the CABRI transients, such as the Serpent 2 code, which also shows potential in the transient simulation and in multiphysics coupling (Syrjälahti, et al., 2015) (Leppanen, 2013) (Aures, et al., 2021).

Multiphysics coupling

The coupling of a Monte Carlo code with a thermal-hydraulics code does not appear to be the most suitable simulation tool for the moment, given the significant computational cost and the difficulties observed in the prompt-supercritical transient simulations, such as for the CABRI transients. As such, at CEA current research is directed towards a coupling between a deterministic neutron transport code (APOLLO3® in this case) and a core and system thermal-hydraulics code. A new thesis, with the objective of developing such a coupling is currently underway (Coissieux, et al., 2022).

Dynamic coupling factor

The study of the variation of the coupling factor should be extended to other transient types. Additionally, studies should be continued to find an optimized number of geometries to model any type of transient and to map all of the impactful parameters on the energy deposition and coupling factor, as well as to quantify their importance (such as the moderator and expansion feedback).

Ultimately, a metamodel could be built to define a coupling factor based on the core parameters (pressurized water-loop conditions, fuel and moderator temperature, control rod position). Similarly, once the power underestimation problem is solved, the analysis should be extended to the dynamic simulations of prompt-supercritical transients

Validation of the calculation methodologies

Evidently, it is necessary to carry out energy deposition measurements during the transient in the core and in the test pin to validate experimentally the calculation scheme presented in this thesis. The CABRI core is not yet equipped with instrumentation that would allow measuring neither the dynamic energy deposition in the test pin, nor the variations in the coupling factor. With this in mind, a thesis was started recently with the aim to develop measurement techniques and ad-hoc instrumentation to map the flux distribution during the transient, ultimately paving the way to dynamic energy deposition measurements.

BIBLIOGRAPHY

Aures, A., Pautz, A. & Zwermann, W., 2021. Transient Calculations of Spert III Experiments. *EPJ Web of Conferences,* 247(EDP Sciences), pp. 07-017.

Brown, D. et al., 2018. *ENDF/B-VIII. 0: the 8th major release of the nuclear reaction data library with CIELO-project cross sections, new standards and thermal scattering data,* Nuclear Data Sheets: 148, pp. 1-142.

Brun, E. et al., 2015. TRIPOLI-4, CEA, EDF and AREVA reference Monte Carlo code. *Annals of Nuclear Energy,* Volume 82, pp. 151-160.

Brun, R., Gheata, A. & Gheata, M., 2003. The ROOT geometry package. *Nuclear Instruments and Methods in Physics Research Section A: Accelerators, Spectrometers, Detectors and Associated Equipment,* 502(2-3), pp. 676-680.

CEA, 2009. *Nuclear fuels; A Nuclear Energy Division Monograph.* Cadarache: ISBN 987-8-281-11345-7.

CEA, 2015. *Neutronics, A Nuclear Energy Division Monograph.* Paris: Editions du Moniteur CEA Saclay and Group Monitoring .

Chevalier, V., Mirotta, S., Guillot, J. & Biard, B., 2018. The CABRI fast neutron Hodoscope: Renovation, qualification program and the first results following the experimental reactor restart. *EPJ Web of Conferences, ANIMMA 2017,* 170(04003), p. 7.

Clamens, O., 2018. *Analyse et propagation des incertitudes associees a la depressurization de l'Helium-3 sur les transitoires de puissance du reacteur CABRI.* Doctoral dissertation: Université Grenoble-Alpes.

Coissieux, T. et al., 2022. Development of a 3D APOLLO3 neutron deterministic calculation scheme for the CABRI experimental reactor. *Submitted to PHYSOR 2022.*

Demaziere, C., Sanchez-Espinoza, V. & Chanaron, B., 2020. Advanced numerical simulation and modelling for reactor safety– contributions from the CORTEX, HPMC, McSAFE and NURESAFE projects. *EPJ Nuclear Sciences & Technologies,* Issue 6, p. 42.

Dulla, S., Mund, E. H. & Ravetto, P., 2008. The quasi-static method revisited. *Progress in Nuclear Energy,* Volume 50(8), pp. 908-920.

Faucher, M., 2019. *Coupling between Monte Carlo neutron transport and thermal-hydraulics for the simulation of transients due to reactivity insertions,* Doctoral dissertation: Université Paris Saclay (COmUE)).

Faucher, M., Mancusi, D. & Zoia, A., 2018. New kinetic simulation capabilities for Tripoli-4: Methods and applications. *Annals of Nuclear Energy,* Volume 120, pp. 74-88.

Faucher, M., Mancusi, D. & Zoia, A., 2021. Multi-physics transient simulations with TRIPOLI-4. *EPJ Web of Conferences* , Volume 247, p. 07019.

Ferraro, D. et al., 2020. Ferraro, D., García, M., Valtavirta, V., Imke, U., Tuominen, R., Leppänen, J. and Sanchez-Espinoza, V., 2020. Serpent/SUBCHANFLOW pin-by-pin coupled transient calculations for a PWR minicore. *Annals of Nuclear Energy,* Issue 137, p. 107090.

Fuketa, T. et al., 1996. *NSRR experiment with 50 MWd/kgU PWR fuel under RIA conditions.* s.l.:s.n.

Geffraye, G. et al., 2011. CATHARE 2 V2. 5_2: A single version for various applications. *Nuclear Engineering and Design,* 241(11), pp. 4456-4463.

Goorley, T., 2014. *MCNP6. 1.1-beta release notes,* LA-UR-14-24680: Los Alamos, USA.

Guénot-Delahaie, I. et al., 2018. Simulation of reactivity-initiated accident transients on UO2-M5® fuel rods with ALCYONE V1. 4 fuel performance code. *Nuclear Engineering and Technology,* 50(2), pp. 268-279.

Imholte, D. & Aydogan, F., 2016. Comparison of nuclear pulse reactor facilities with reactivity-initiated-accident testing capability. *Progress in Nuclear Energy,* Volume 91, pp. 310-324.

Imke, U. & Sanchez, V., 2012. Validation of the subchannel code SUBCHANFLOW using the NUPEC PWR tests (PSBT). *Science and Technology of Nuclear Installations.*

IRSN, 2021. [En ligne]
Available at: https://www.irsn.fr/EN/Research/Research-organisation/Research-programmes/CABRI-International-program/Pages/CABRI-Facility.aspx
[Accès le 2019].

Jeury, F., Pantera, L. & Garnier, Y., 2013. CABRI experimental reactor: experimental reassessment of CABRI core power and measurement uncertainties. *IGORR2013,* pp. 13-18.

Labit, J.-M., 2020. *Modélisation multiphysique des transitoires d'insertion de réactivité et méthodologie de validation appliquée au réacteur CABRI,* Doctoral dissertation: Université Grenoble Alpes.

Lemaire, M., 2015. *Validation des calculs d'échauffements photoniques en réacteur d'irradiation au moyen du programme expérimental AMMON et du dispositif CARMEN,* Aix-Marseille: Doctoral dissertation.

Leppanen, J., 2013. Development of a dynamic simulation mode in Serpent 2 Monte Carlo code. *Proceedings of M&C,* pp. 5-9.

Leppanen, J. et al., 2015. The Serpent Monte Carlo code: Status, development and applications in 2013. *Annals of Nuclear Energy,* Volume 82, pp. 142-150.

Moal, A., Georgenthum, V., Bernaudat, C. & Parrot, A., 2018. *L'accident d'ejection de grappe.* Paris

Mylonakis, A., Varvayanni, M., Grigoriadis, D. G. E. & Catsaros, N., 2017. Developing and investigating a pure Monte-Carlo module for transient neutron transport analysis. *Annals of Nuclear Energy,* Issue 104, pp. 103-112.

Nuclear Energy Agency, 2010. *Nuclear Fuel Behaviour during Reactivity Initiated Accidents, Workshop Proceedings.* (No. NEA-CSNI-R--2010-7)

Nuclear Energy Agency, 2010. *Nuclear fuel behaviour under reactivity initiated accident (RIA) conditions: state-of-the-art report,* (No. NEA-CSNI-R--2010-1)

OECD, 1995. *Transient behaviour of high burnup fuel.* (NEA-CSNI-R--95-22)

OECD, 2012. *Nuclear fuel safety criteria Technical Review Second Edition,* (No.7072), ISBN 978-92-64-99178-1

OECD, 2013. *Fuel safety criteria in NEA member countries,* (No. NEA-CSNI-R--2003-10) Organisation for Economic Co-Operation and Development

Ott, K. & Neuhold, R. J., 1985. *Introductory nuclear reactor dynamics.* American Nuclear Society.

Papin, J. et al., 1996. French studies on high-burnup fuel transieny behavior under RIA conditions. *Technical progress journal,* 37(4), pp. 289-327.

Peron, A., 2014. *Contribution à l'amélioration des méthodes d'évaluation de l'échauffement nucléaire dans les réacteurs nucléaires à l'aide du code Monte-Carlo TRIPOLI-4®*. Université Paris Sud: Doctoral dissertation.

Ravaux, S., 2013. *Qualification du calcul de l'échauffement photonique dans les réacteurs nucléaires.* Université Grenoble: Doctoral dissertation.

Reuss, P., 2008. *Neutron physics.* EDP sciences

Richards, S. et al., 2019. MONK11A: status and plans for the MONK Monte Carlo code for criticality safety and reactor physics analyses. *Proceedings of International Conference on Mathematics and Computational Methods Applied to Nuclear Science and Engineering, Portland, Oregon,* pp. 495-506.

Ritter, G., Berre, R. & Pantera, L., 2012. DULCINEE. Beyond neutron kinetics, a powerful analysis software. *In Proc. RRFM IGORR,* p. 5.

Roque, B. et al., 2002. Experimental validation of the code system DARWIN for spent fuel isotopic predictions in fuel cycle applications. *Int. Conf. on Reactor Physics Safety and High-Performance Computing (PHYSOR).*

Rudling, P. et al., 2016. *Nuclear fuel behaviour under RIA conditions,* Advanced Nuclear Technology International Europe AB: Tollered Sweden

Sanchez-Espinoza, V. et al., 2021. The McSAFE project-high-performance Monte Carlo based methods for safety demonstration: from proof of concept to industry applications. *EPJ Web of Conferences,* 247(EDP Sciences), p. 06004.

Santamarina, A. et al., 2009. *The JEFF-3.1. 1 nuclear data library,* 22 (10.2), p.2: JEFF report.

Sartoris, C. et al., 2010. A consistent approach to assess safety criteria for reactivity initiated accidents. *Nuclear Engineering and Design,* 240(1), pp. 57-70.

Schneider, D. et al., 2016. APOLLO3®: CEA/DEN deterministic multi-purpose code for reactor physics analysis. *Proc. Int. Conf. PHYSOR,* p. 2274.

Schubert, A. et al., 2011. Application of the extended TRANSURANUS code in the FUMEX-III project. *9th International Conference on WWER Fuel Performance, Modelling and Experimental Support.*

Sjenitzer, B., 2013. *The dynamic Monte Carlo method for transient analysis of nuclear reactors.* Delft University of Technology: Doctoral dissertation.

Sjenitzer, B. & Hogenboom, J., 2013. Dynamic Monte Carlo method for nuclear reactor kinetics calculations. *Nuclear Science and Engineering,* Issue 1, pp. 97-107.

Sjenitzer, B., Hoogenboom, J., Escalante, J. & Espinoza, V., 2015. Coupling of dynamic Monte Carlo with thermal-hydraulic feedback. *Annals of Nuclear Energy,* Issue 76, pp. 27-39.

Syrjälahti, E. et al., 2015. Multiphysics simulations of fast transients in VVER-1000 and VVER-440 reactors.

Westinghouse, 2021. *Optimized ZIRLO High-performence Fuel Cladding Material.* [En ligne]
Available at:
https://www.westinghousenuclear.com/Portals/0/operating%20plant%20services/fuel/fuel%20products/NF-FE-0046%20Optimized%20ZIRLO%20HP%20Fuel%20Clad%20Mtl.pdf

World Nuclear Association, 2017. *Mixed Oxide (MOX) Fuel.* [En ligne]
Available at: https://www.world-nuclear.org/information-library/nuclear-fuel-cycle/fuel-recycling/mixed-oxide-fuel-mox.aspx
[Accès le 2021].

Yamauchi, A., 2018. *Criteres et etudes de surete en ejection de grappe.* Paris

ANNEXES

ANNEX A. Power interpolation in the stepwise methodology

The power interpolation steps are presented for the prompt supercritical test case. Figure 82 shows the stepwise power evolution calculated by linearly interpolation between the instantaneous power values defined by the geometry choices. While the chosen geometries are adequate in being representative of the different core configurations, it can be observed that this discretization is not fine enough to reproduce an accurate power evolution. An accurate power evolution is not needed for the driver core itself, since the core power evolution can be calculated with PALANTIR if there is no experimental data. Instead, it is needed to calculate the test pin power evolution and, consequently, the energy deposition into the test pin, which can be neither calculated with PALANTIR, nor measured during the experiment.

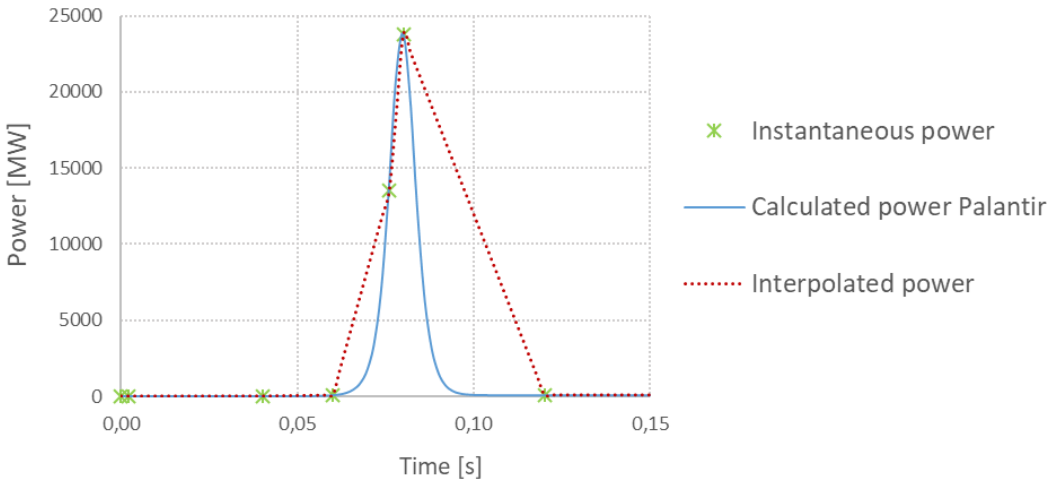


Figure 82. Stepwise power evolution obtained by linear interpolation between the instantaneous values

As, in this case, the interpolation between the instantaneous values leads to an overestimation in the core power, it would lead to an overestimation of the pin power as well. The accuracy of the power evolution calculation can be increased by implementing more normalization steps. The dynamic power would be normalized to the calculated power corresponding to the chosen instant without changing the core configuration. For example, based in Figure 82, two extra normalization steps need to be included between the 3rd and 4th geometry to capture the power increase and two more during the power decrease phase. Similarly, in the case of the last geometry change, the power is not considered constant anymore, instead it is linearly decreasing to the final power calculated with PALANTIR. The final stepwise power core power

evolution (interpolated power) is shown in Figure 83, including the power evolution calculated with PALANTIR and the instantaneous and extra normalization steps.

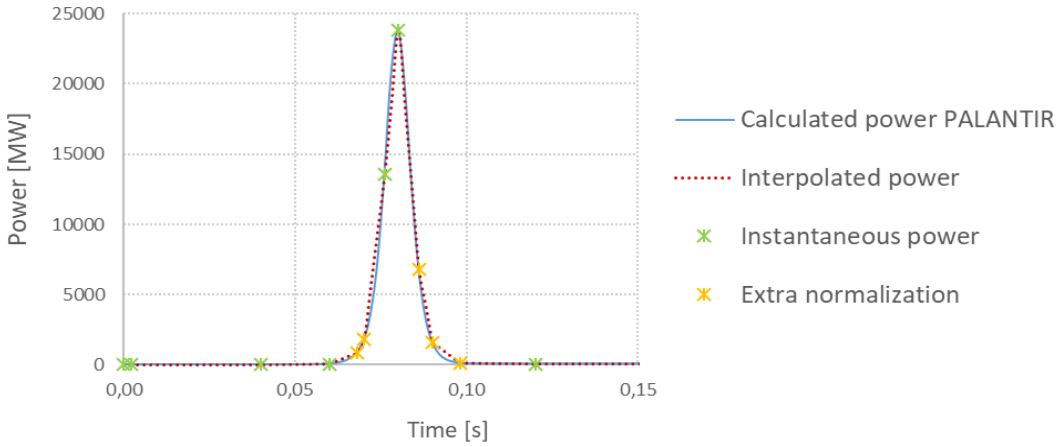


Figure 83. Updated stepwise core power evolution

The goal is to have e relative difference between the energy deposition in the core calculated from the power evolution given by PALANTIR and by the power interpolation on the same order of magnitude, or lower, as the error on the experimental power measurement (<3%).

At each normalization step, a normalization factor is also calculated, which is then used to determine the test pin power (using Eq. 2-2), and, just as in the case of the core power, the pin power evolution is obtained by interpolating between the instantaneous and normalized values.

ANNEX B. Multiplicity and spectra calculation with DARWIN/PEPIN2

In order to simplify the explanation, the calculation methodology will be presented for only one source calculation: the definition of the delayed gamma source following the fission of a ^{235}U particle. The calculation scheme is similar for all delayed sources; the only differences are in the fissile isotope that is defined in the DARWIN/PEPIN2 input file and the energy discretization (93 groups for gamma and 61 groups for beta sources). The beta and gamma emissions are computed for 60 minutes after the fission, with a time step of 0.01 seconds.

The calculation scheme presented below is the calculation scheme defined in (Lemaire, 2015). The multiplicity and spectra are calculated with the PEPIN2 module of the DARWIN code, developed at CEA. The nuclear data used in PEPIN2 is coming from the JEFF 3.1.1. evaluations (CEA, 2015).

The calculation steps are the following:

- PEPIN2 calculates the concentrations of the fission products $N_i(t)$ over the defined time scale
- From the concentration of the fission products and the decay constants λ_i, DARWIN computes the activity $A_i(t)$, i.e. the number of disintegrations per second for each fission product

$$A_i(t) = \lambda_i \times N_i(t)$$

- The average number of gamma rays emitted per disintegration for each fission product and energy group $S_i(E_\gamma)$, is also available in code. Then the total emitted gamma rays over a time step, $S_{U5}(t, E_\gamma)$, is calculated as:

$$S_{U5}(t, E_\gamma) = \sum A_i(t) \times S_i(E_\gamma)$$

- The total number of gamma rays, $N(T, E_\gamma)$, for a given energy emitted over all time steps after a fission at time T is given by:

$$N(T, E_\gamma) = \int_{t=0}^{T_{tot}-T} S_{U5}(t, E_\gamma)\, dt$$

- T_{tot} refers to the entirety of the studied time scale, which is generally made up of an irradiation time, T_i, and a cooling time, T_{cool}. For these calculations, the cooling time was not considered. Then, in order to take into account all the fissions taking place during the irradiation, total number of gamma rays needs to be integrated the

irradiation time T_i. Dividing this with the irradiation time results in the average delayed gamma spectrum,$\overline{S_\gamma}$, as shown below:

$$\overline{S_\gamma} = \frac{1}{T_i}\int_{T=T_{cool}}^{T=T_i}\int_{t=0}^{T} N(t, E_\gamma)\, dt\, dT$$

- This integration is solved via a python script by discretizing it, as follows:

$$\overline{S_{\gamma,discr}} = \frac{\Delta t^2}{T_i}\left[\sum_{i=k}^{n-1}\sum_{j=0}^{i-1} S_{U5}(j\Delta t) + \left(\frac{S_{U5}(n\Delta t)}{4} - \frac{S_{U5}(k\Delta t)}{4} - \frac{mS_{U5}(0)}{4}\right) + \sum_{i=k}^{n-1} S_{U5}(i\Delta t)\right]$$

Where:

$$k = T_{tot}/dt$$
$$m = T_i/dt$$
$$n = k + m$$

- Finally summing this spectrum over all energy groups gives the multiplicity M of the source.

$$M = \sum \overline{S_\gamma}$$

- However, in (Lemaire, 2015) it was observed, that the residual energy computed directly by the code, E_{res}, and the residual energy calculated by integrating the computed spectrum, $E_{spectrum}$, over all energy groups is not the same, suggesting a possible bias in the nuclear data. To account for this bias, a correction factor needs to be applied on the multiplicity, which is given by the ratio of the residual energy computed by the code and the residual energy calculated by integrating the spectrum, as shown below. This corrected multiplicity, M_{corr}, is used to define the intensity of the delayed source.

$$M_{corr} = M \times \frac{E_{res}}{E_{spectrum}}$$